POLITECNICO DI TORINO

Master of Science
in Biomedical Engineering, Bionanotechnology

Master Thesis

Design and development of novel core-shell nanoparticles for antitumor therapy

Supervisor:
Prof. Valentina Cauda

Candidate:
Claudia Amato

Academic Year 2025/2026
April 2026

This page left intentionally blank

Abstract

Nanomedicine currently stands at the forefront of modern medicine, offering innovative strategies to address the limitations of conventional antitumoral therapies. In this context, Zinc Oxide (ZnO) has garnered significant attention due to its semiconductor properties and its potential for cancer cell selective cytotoxicity. However, the clinical translation of ZnO is still limited due to its inherent instability in biological fluids. This leads to the unregulated leakage of zinc ions and premature ROS production, which pose a significant risk of off-target toxicity to healthy tissues.

The primary objective of this thesis is to mitigate this off-target toxicity and overcome the limitations of the system in biological environments. This is achieved through the design of specific shells tailored to incorporate Iron-doped Zinc Oxide (Fe-ZnO) nanoparticles (NPs) and quantum dots (QDs). Iron-doping confers unique piezoelectric, sono- and photo-catalytic properties upon ZnO, enabling controlled, stimuli-driven activation of the nanosystem and enhancing its diagnostic and therapeutic potential. The experimental strategy to engineer the surface relied on two distinct coating approaches: an inorganic strategy based on silica shells and a self-assembly strategy based on lipid coating via microfluidic technology.

Physicochemical characterization confirmed the successful synthesis of the nanometric cores, yielding high-purity, crystalline Fe-ZnO NPs and ultrasmall quantum dots. Results regarding the silica coating on Fe-ZnO NPs were encouraging, colloidal stability was preserved in aqueous media and the Z-potential shifted from the intrinsic positive value of ZnO to the negative potential typical of silica NPs. This makes these NPs primary candidates for subsequent stability and biological interaction studies. In contrast, QDs proved difficult to stabilize even with silica coating, possibly due to their high tendency to aggregate in basic environments. Similarly, preliminary data showed improved stability for lipid-coated Fe-ZnO NPs, while lipid-coated QDs revealed lack of colloidal stability precluding their use in biological studies.

Biological validation of the optimized silica-coated system was conducted via in vitro cytotoxicity assays on human lung adenocarcinoma cells (A549). The results demonstrated a sharp contrast: uncoated Fe-ZnO nanoparticles induced severe, dose-dependent cytotoxicity leading to a near-total loss of cell viability even at low concentrations, while the silica-coated counterparts attenuated this effect, increasing the biocompatibility of the nanoconstruct and allowing for higher doses to be safely administered. This outcome suggests that the dense silica shell acts as a protective barrier, mitigating the inherent toxicity of the core by likely regulating its dissolution and limiting direct interaction with cells.

In conclusion, this study shows an example of the potential of surface engineering, specifically through inorganic and organic core-shell architectures, in tuning the biological impact of Fe-ZnO. These findings identify silica-coated Fe-ZnO NPs as promising candidates for next-generation biocompatible nanoconstructs, providing a viable strategy to reduce off-target toxicity and paving the way for future advancements in the antitumoral field.

Table of contents

List of figures

List of tables

1 Introduction

1.1 Overview on nanomedicine and clinical needs

Over the past three decades, the interdisciplinary field of nanomedicine has undergone a period of intensive research and exponential growth. Building upon continuous advancements in nanotechnology, this sector has facilitated the transition of numerous medical products from the bench to the global market, while a significant number of novel formulations are currently navigating the complex pipelines of clinical translation [1–3]. This technological evolution has driven significant progress leading to the development of innovative nanotherapeutics, which include both engineered nanoparticles and sophisticated nanostructured medical devices, such as scaffolds for tissue engineering or diagnostic biosensors. These systems represent a promising evolution compared to traditional pharmaceutical approaches, offering the potential for more precise disease management [4]. With a view toward future clinical transition, nanomedicine has the potential to revolutionize oncology, offering advanced diagnostic and therapeutic capabilities that improve early detection and pave the way for efficient, personalized therapies [2].

Despite these advances, the global burden of severe pathologies such as cancer [5] and conditions related to chronic oxidative stress, including neurodegenerative and cardiovascular diseases [6], continues to rise. This escalating oncological trend highlights the critical limitations of conventional treatment methods, such as chemotherapy, radiation therapy, and immunotherapy, which are often hampered by a lack of specificity, significant systemic toxicity, and the onset of multidrug resistance [2,7,8]. Traditional chemotherapeutic agents frequently suffer from poor water solubility, nonspecific biodistribution, and a low therapeutic index [7,9]. Consequently, there is an urgent need for targeted strategies capable of confining therapeutic action to the tumor site, thereby minimizing side effects on healthy tissues [8].

In this context, nanoparticles represent a promising alternative to conventional chemotherapy. Their unique physicochemical properties, like high drug-loading capacity and responsiveness to external stimuli, allow for site-specific activation, enabling a potential targeted therapy [10].

1.2 Nanoparticles (NPs): definition and biological interaction

According to the International Union of Pure and Applied Chemistry (IUPAC), a nanoparticle is defined as a particle with dimensions ranging from 1 to 100 nanometers. This specific dimensional limit is critical because, at this scale, materials begin to exhibit novel physicochemical properties, such as quantum effects, transparency, and enhanced reactivity, that distinguish them significantly from their bulk counterparts [11,12]. However, this definition acts as a general guideline, as in practice, for nanomedicine applications, the prefix is frequently applied to structures up to 500 nm. This extension of the dimensional range is justified by the fact that larger particles or aggregates may retain characteristic nanoscale behaviors, such as high surface-area-to-volume ratio and quantum confinement effects, which are relevant for biomedical applications like drug delivery and imaging regardless of the formal 100 nm threshold. [11].

The therapeutic potential of NPs is fundamentally dictated by their physicochemical features. First, their size is comparable to that of biological macromolecules, such as proteins and DNA, which play key roles in regulating cellular cycles and maintaining homeostasis [13]. This size similarity allows NPs to mimic biomolecular activity, navigate biological barriers, and interact with biological systems for therapeutic purposes [14]. Second, the extremely large surface-area-to-volume ratio of NPs enables them to encapsulate or adsorb high amounts of therapeutic agents, facilitating a greater therapeutic payload compared to conventional drugs. As well, the intrinsic therapeutic potential of some types of inorganic NPs, such as metallic and metal oxides NPs, based on their optical, magnetic and catalytic properties, has been widely investigated, particularly in the field of cancer therapy [15]. Furthermore, NPs vast surface area and high reactivity enable easy functionalization, which is an effective method to impart new properties such as enhanced colloidal stability or specific targeting capabilities using peptides or antibodies [14]. These factors contribute collectively to the improvement of both the safety and efficacy of treatments, positioning nanomedicine as a pivotal tool in the era of personalized medicine [14,15].

1.2.1 Classification of nanoparticles

A wide variety of NPs have been investigated in nanotherapeutics research, resulting in the definition of distinct classes as shown in Figure 1. Each presents unique advantages and disadvantages concerning safety, efficacy, and manufacturing.

Polymeric nanoparticles are solid structures made of synthetic or natural polymers which are advantageous due to their biodegradability and biocompatibility, offering a versatile platform where the surface can be easily modified to control circulation times and drug release profiles [3]. However, despite their versatility, challenges such as potential aggregation and complex toxicity profiles remain hurdles for widespread clinical approval [3,15].

Lipid-based nanoparticles are structures that rely on the self-assembly of phospholipids to produce highly biomimetic systems. They currently represent the gold standard for the delivery of nucleic acids and lipophilic drugs. [16] . They are the most widely studied and common class of FDA-approved nanomedicines due to their formulation simplicity and great pharmacokinetic properties [15,16]. Their amphiphilic nature allows them to encapsulate both hydrophilic and hydrophobic drugs effectively, although they can face challenges related to stability and poor biodistribution, with preferential uptake by the liver and spleen [4,15].

Finally, inorganic nanoparticles are structures composed of inorganic elements such as gold, iron, and silica. Due to their unique electronic and physical properties given by the nanoscale, including optical, magnetic or semiconductive behaviors, these inorganic systems can be engineered into theranostics devices that function not only as drug carriers but also as active agents in both imaging and stimuli-responsive therapies.[15,17]. Despite their promise, particularly in photothermal therapy and imaging, inorganic NPs often face challenges related to low colloidal stability and toxicity concerns, necessitating careful surface engineering [4,15].

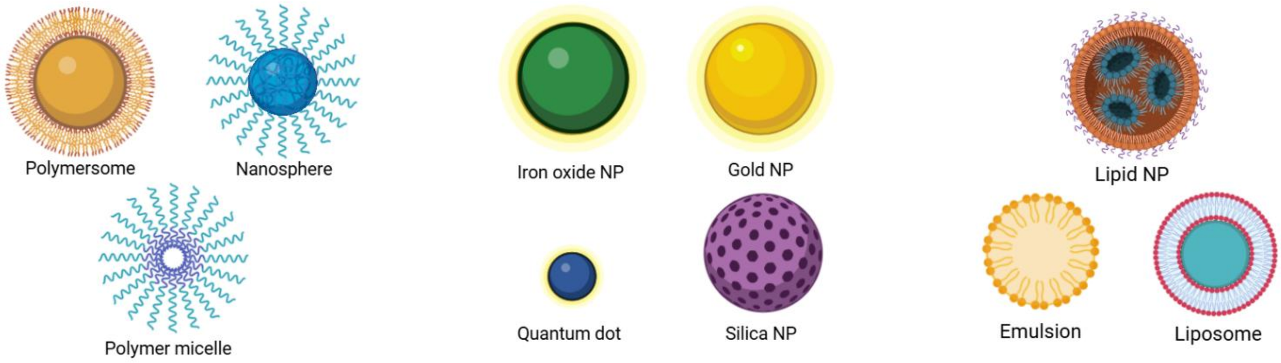

Figure 1 *Schematic representation of the primary nanoparticle categories: polymeric, inorganic, and lipid based. (Image created in BioRender.com)*

1.3 Zinc oxide nanoparticles and quantum dots

Among the inorganic materials explored for biomedical applications, nanostructured Zinc Oxide (ZnO) has captured considerable attention [18,19]. ZnO is an abundant, cost-effective wide band-gap semiconductor (3.37 eV) classified as a “Generally Recognized As Safe” (GRAS) substance by the Food and Drug Administration (FDA) [14,18,20]. This safety classification, combined with its unique physical and chemical properties, such as photo- and sono-catalytic activity, piezoelectricity, and pyroelectricity, makes it a highly suitable candidate for a plethora of biomedical applications. [21–26].

The inherent potential of ZnO NPs in exhibiting anticancer activity has been acknowledged, with recent studies emphasizing the possibility of further enhancing their performance by tailoring their physicochemical properties [7,27].

These properties can be optimized and even strengthened by selecting the most appropriate morphology, as ZnO can be synthesized through wet and dry synthetic approaches in various forms, including thin films, nanowires, nanorods, nanobelts, nanoparticles, and flower-like structures [28–35].

A particularly interesting phenomenon occurs when the particle size of ZnO is reduced to the nanometer scale, typically 2–10 nm, as this reduction results in quantum confinement effects that transform the particles into Quantum Dots (QDs) with size-tunable optical properties. In this sense, ZnO nanoparticles serve a dual purpose, as they can be used as imaging agents without the need of standard fluorophores while simultaneously acting as therapeutic agents [36,37].

Furthermore, due to their reduced size, ZnO NPs can be effectively internalized and localized in the human body, facilitating accumulation and interaction with target tissues [38].

1.4 Surface chemistry, physiological stability, and toxicity mechanisms

The interaction of ZnO NPs with the biological environment is heavily dependent on their surface chemistry. The surface of pristine ZnO NPs is largely determined by hydroxyl groups that play a key role in controlling the surface charge. Since ZnO NPs typically have an isoelectric point between pH 9 and 10, they exhibit a predominantly positive surface charge under physiological conditions [38]. While this positive charge leads to the interaction with negatively charged cell membranes, facilitating initial adhesion and uptake, it can also provoke instability phenomena and unspecific protein adsorption, i.e. protein corona, when the particles enter the bloodstream [39].

The primary application of ZnO NPs in oncology is based on the possibility of rendering the particles toxic under specific conditions to selectively kill tumor cells. This therapeutic effect is primarily achieved through the release of zinc ions Zn^{2+} and the generation of Reactive Oxygen Species (ROS). Specifically, ROS production is associated with the semiconductor and catalytic properties of ZnO, which can be enhanced by specific physical or chemical external stimuli. The release of Zn^{2+} cations is triggered by the instability of the particles in acidic conditions, such as those typically found within the tumor microenvironment or in the cellular sub-compartments late endosomes and lysosomes. Once the zinc ions are present inside the cell, the cytotoxic response is predominantly driven by the activation of interconnected signaling pathways [40–43]. This internal overload of zinc ions leads directly to mitochondrial dysfunction, protein activity disequilibrium and disruption of cellular signaling pathways, which ultimately results in cell death through apoptosis involving both intrinsic and extrinsic pathways and the activation of caspase enzymes. [43–45].

However, because the dissolution of ZnO and the subsequent release of Zn^{2+} ions are not inherently specific to malignant cells, achieving clinical precision remains a challenge. Between the two cytotoxic mechanisms, ROS generation could be more easily controlled: upon activation by physical stimuli, ZnO nanoparticles generate ROS, pushing oxidative stress beyond a cytotoxic threshold, whereas in normal tissues they may instead contribute to restoring redox balance [46]. The challenge, therefore, lies in modulating the dissolution rate through surface engineering, thereby minimizing off-target toxicity while maintaining the ROS-mediated therapeutic efficacy against cancer cells.

1.5 Iron doping: enhancing the stability of ZnO NPs

While Zinc Oxide (ZnO) has been successfully applied in diverse sectors ranging from gas sensing to biomedicine [47], expanding its potential requires strategies that go beyond the simple optimization of its own features [48,49]. To create a truly multifunctional system, doping represents a valuable approach, as the embedding of specific guest atoms into the crystal lattice of the host material allows for the fine-tuning of its electronic, optical, or chemical characteristics [50].

Among transition metals, iron is of particular interest due to its ability to exist in dual oxidation states, Fe^{2+} and Fe^{3+}, a property that significantly increases the functional range of the nanoparticle. From a therapeutic perspective, iron-doped ZnO NPs (FeZnO) represent a sophisticated theranostic system, as the inclusion of these metal atoms within the lattice broadens the light absorption spectrum and enables the generation of additional reactive species. This enhancement is primarily driven by Fenton-like reactions, where iron ions catalyze the conversion of hydrogen peroxide into highly reactive hydroxyl radicals, thereby amplifying the overall oxidative stress within the tumor environment [18].

Moreover, iron doping addresses one of the main limitations of pure ZnO, namely its poor stability. It has been demonstrated that Fe doping improves chemical stability in aqueous media and reduces the dissolution rate of the NPs. This reduction in solubility is a pivotal factor for mitigating the rapid and uncontrolled release of cytotoxic ions, which helps in preventing undesirable damage to healthy cells while maintaining high therapeutic efficacy against tumor tissues [51].

1.6 The role of protective shells: Silica and Lipid coating

The clinical translation of ZnO NPs is significantly hindered by their instability in biological fluids, as the rapid dissolution of the particles leads to a massive and uncontrolled release of zinc ions Zn^{2+} into the surrounding medium [52]. To overcome these limitations, several strategies have been investigated in the literature, ranging from the modification of the internal crystal structure, like the doping just mentioned, to surface engineering via encapsulation. To achieve a truly robust system, the encapsulation of the ZnO core within a silica (SiO_2) shell has emerged as a potent solution to enhance biocompatibility [52].

The silica coating acts as a physical barrier that stabilizes the nanoparticles and drastically reduces the dissolution rate, and was proven to mitigate the release of cytotoxic ions even in acidic conditions [52,53]. Consequently, silica-coated NPs show a significantly improved safety profile when compared to naked ZnO NPs. Moreover, this surface modification preserves the functional properties of the core, and may even enhance specific attributes, such as antimicrobial activity [52,53]. Beyond dense coatings, silica offers the versatility to be engineered into mesoporous structures, providing additional advantages including a high specific surface area and tunable pore volume. These features maintain the protective function against premature degradation and create a platform for high-capacity drug loading, enhancing the overall therapeutic potential [54].

In addition to silica, encapsulation in lipid shell represents a highly effective strategy for the stabilization of NPs. Driven by thermodynamic interactions, phospholipids and cholesterol can self-assemble around the ZnO core, forming a supported lipid bilayer. This biomimetic coating acts as a physical barrier between the reactive nanocrystal surface and the aqueous physiological environment, slowing down the particles dissolution [39]. Furthermore, these shells are structurally similar to biological membranes, providing a biomimetic shield that improves in vivo biocompatibility and extends systemic circulation times [39].

1.7 Thesis objective

One of the primary challenge in the application of ZnO NPs in biomedical fields remain the low stability in biological fluids and the non-controllable, rapid release of Zn^{2+} cytotoxic species [55,56]. Literature studies indicate doping and inorganic and organic coating (such as silica and lipids) as promising strategies to enhance their chemical and colloidal stability in biological environment. However, these strategies could benefit from further optimization and synthetic routes, specifically tailored to the type of ZnO NPs.

In this context, this thesis focuses on the synthesis of two ZnO-based nanomaterials, ZnO NPs and QDs, and on specific strategies to mitigate their toxicity and enhance stability in biologically-relevant media. This is achieved through the development of protective shells, specifically silica coatings (dense and/or mesoporous) or lipid shells, designed to stabilize ZnO in biological environment.

This thesis is composed of three main sections. The first one is dedicated to the synthesis of ZnO NPs. Specifically, ZnO nanoparticles (NPs) and ZnO quantum dots (QDs), which differ primarily in their dimensions, will be synthesized, also evaluating the incorporation of doping ions into the crystalline structure. Additionally, an amino-propyl surface functionalization will be performed on the ZnO NPs, either in situ during synthesis or as a post-synthesis treatment. This functionalization improves the colloidal stability of the NPs themselves and serve as anchoring groups for eventual functional molecules, such as fluorescent dyes for biomedical imaging.

The second section focuses on encapsulating these NPs within a silica coating. Given the dimensional differences of the synthesized NPs, this section evaluates how the nature of the particles could affect the silica coating process. Also, the inherent instability of ZnO at the typical pH conditions for silica formation presented an opportunity to determine the most effective approach for keeping the nanoparticles well-dispersed, leading to a comparative evaluation of simple mechanical agitation and ultrasound-assisted dispersion.

Finally, the third section explores the use of a lipidic shell as a coating strategy for the QDs. For this purpose, a novel microfluidic approach will be investigated to perform the coating in a continuous flow, thereby ensuring a highly throughput process. All the engineered nanoconstructs were characterized via X-ray diffraction (XRD), Field Emission Scanning Electron Microscopy (FESEM), and Dynamic Light Scattering (DLS) to assess their crystal structure, morphology, and colloidal stability, respectively. Finally, their biological performance and safety profile were evaluated through toxicity assays on A549 human lung adenocarcinoma cells, selected as a representative in vitro model to confirm the reduction of the intrinsic ZnO NPs toxicity.

2 Materials and Methods

2.1 Materials

Zinc Acetate dihydrate ($Zn(CH_3COO)_2{\cdot}2H_2O$), potassium hydroxide (KOH), ethanol (EtOH), methanol (MeOH), ferric nitrate nonahydrate ($Fe(NO_3)_3{\cdot}9H_2O$), gadolinium nitrate hexahydrate ($Gd(NO_3)_3{\cdot}6H_2O$), 3-aminopropyltrimethoxysilane (APTMS), methanol (MeOH), sodium hydroxide (NaOH), tetramethylammonium hydroxide (TMAH), tetraethyl orthosilicate (TEOS), ammonium hydroxide (NH4OH) were purchased by Sigma-Aldrich. Oleic acid was purchased by VWR International and cetyltrimethylammonium Bromide (CTAB) was purchased by AnalytiChem Belgium NV.

1,2-dioleoyl-sn-glycero-3-phosphate, sodium salt (18:1 PA; DOPA); 1,2-dioleoyl-sn-glycero-3-phosphocholine (18:1 (Δ9-Cis) PC; DOPC); 1,2-Dioleoyl-3-trimethylammonium propane (DOTAP); 1,2-distearoyl-sn-glycero-3-phosphoethanolamine-N-[amino(polyethyleneglycol)-2000], ammonium salt (DSPE-PEG(2000) Amine); and cholesterol (ovine derived) were purchased from Avanti Polar (Avanti Research™ - USA) either dissolved in chloroform solution or lyophilized in powder from.

Reagents for in vitro assays, including Dulbecco's Modified Eagle Medium (DMEM), L-glutamine, penicillin-streptomycin, Fetal Bovine Serum (FBS), trypsin, Phosphate-Buffered Saline (PBS), and Trypan Blue were purchased from Sigma-Aldrich. The WST-1 cell proliferation reagent was acquired from Roche.

2.2 Synthesis and functionalization of zinc oxide nanoparticles

2.2.1 Synthesis of Iron-doped zinc oxide nanoparticles with Oleic acid

Iron-doped zinc oxide nanoparticles (FeZnO NPs) were synthesized by a wet chemical hydrolysis method following a previously established protocol [50] that uses oleic acid as stabilizing agent. Specifically, 526 mg of $Zn(CH_3COO)_2{\cdot}2H_2O$ and 58 mg of $Fe(NO_3)_3{\cdot}9H_2O$ were dissolved in a mixture of 40 mL of absolute ethanol and 1 mL of MilliQ water in a 100 mL three-neck round-bottom flask. This ratio was selected to achieve a nominal iron doping concentration of 6 atomic percent (6 at. %) with respect to Zn ions. Afterwards 140 µL of oleic acid were added to the solution. The reaction mixture was heated to 70 °C under reflux conditions and continuous magnetic stirring (300 rpm).

In parallel, an alkaline solution was prepared by dissolving 1.044 g of TMAH in 1.052 mL of MilliQ water, followed by the addition of 10 mL of absolute ethanol. Once the precursor solution reached the target temperature, the TMAH solution was rapidly poured into the flask to trigger nucleation. The reaction proceeded for 10 minutes, after which it was quenched by adding 40 mL of cold ethanol (4°C).

The resulting nanoparticles were collected by centrifugation at 8000 × g for 10 minutes and washed two times with ethanol. Finally, the synthesis yield was determined by drying 0.5 mL of the final suspension in a pre-weighed Eppendorf tube; the mass difference after solvent evaporation allowed for the calculation of the particle concentration.

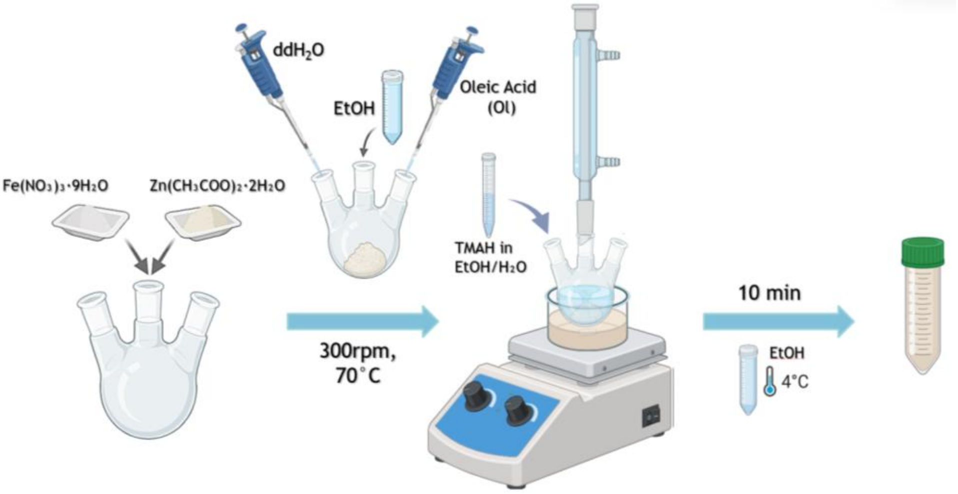

Figure 2 *Schematic overview of the experimental setup used for the preparation of Fe-doped ZnO nanoparticles (FeZnO NPs) with oleic acid. (Image created in BioRender.com)*

2.2.2 Synthesis of Iron-doped zinc oxide nanoparticles without Oleic acid

The formation of the silica coating can be hindered by chemical species on the ZnO surface that obstruct the covalent bonding of the silica precursor. Consequently, the effect of removing the oleic acid capping was investigated. A second batch of nanoparticles (OlFeZnO NPs) was synthesized without oleic acid. The procedure followed the same protocol described in section 2.2.1 without the oleic acid addition to verify that morphology and DLS dimensions remained consistent even in the absence of the capping agent. All the reaction steps, including nucleation time, quenching, and washing, remained unchanged.

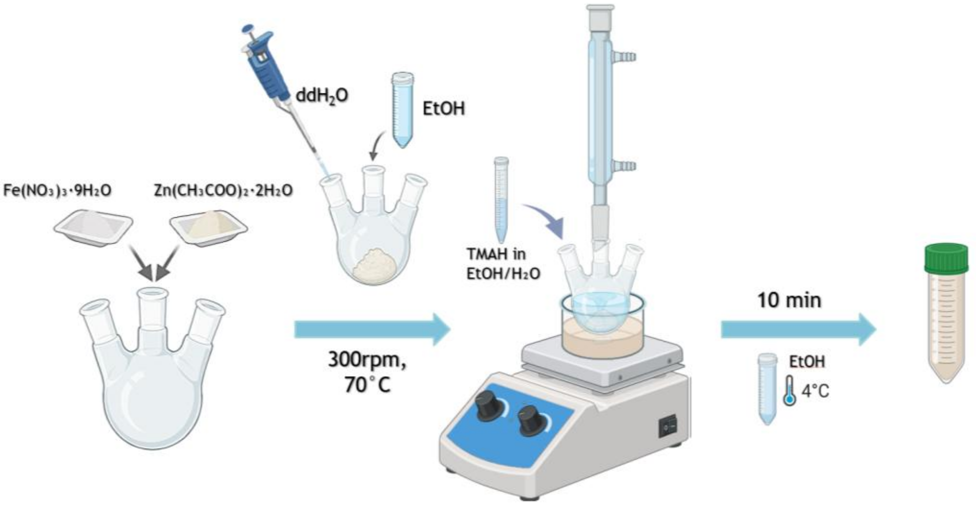

Figure 3 *Schematic overview of the experimental setup used for the preparation of FeZnO NPs without Oleic acid (OlFeZnO NPs). (Image created in BioRender.com)*

2.2.3 Functionalization with amino groups

The surface functionalization of iron-doped ZnO nanoparticles with amino groups was performed following a previously established procedure [50]. In detail, 40 mg of pristine nanoparticles were dispersed in ethanol to achieve a final concentration of 2.5 mg/mL. The dispersion was transferred into a 25 mL round-bottom flask and heated to 70 °C under reflux conditions, with moderate stirring and a continuous flow of nitrogen gas.

After allowing the system to equilibrate for 10 minutes, a specific amount of (3-Aminopropyl)trimethoxysilane (APTMS) was added to the dispersion to obtain two different batches. In the first case, 8.6 µL of APTMS were added, corresponding to 10 mol% relative to the total molar amount of ZnO, while a second batch was prepared using 86 µL of the precursor to achieve a 100 mol% functionalization. We investigated these two quantities to assess whether increasing the APTMS concentration yields a marked improvement in surface functionalization. The reaction was maintained under a nitrogen atmosphere with continuous stirring for 6 hours and in refluxing conditions to prevent solvent evaporation.

Finally, the functionalized nanoparticles were collected by centrifugation at 12,000 × g for 20 minutes. To ensure the complete removal of unbound APTMS molecules, the precipitate was washed two times with ethanol through successive centrifugation and redispersion cycles.

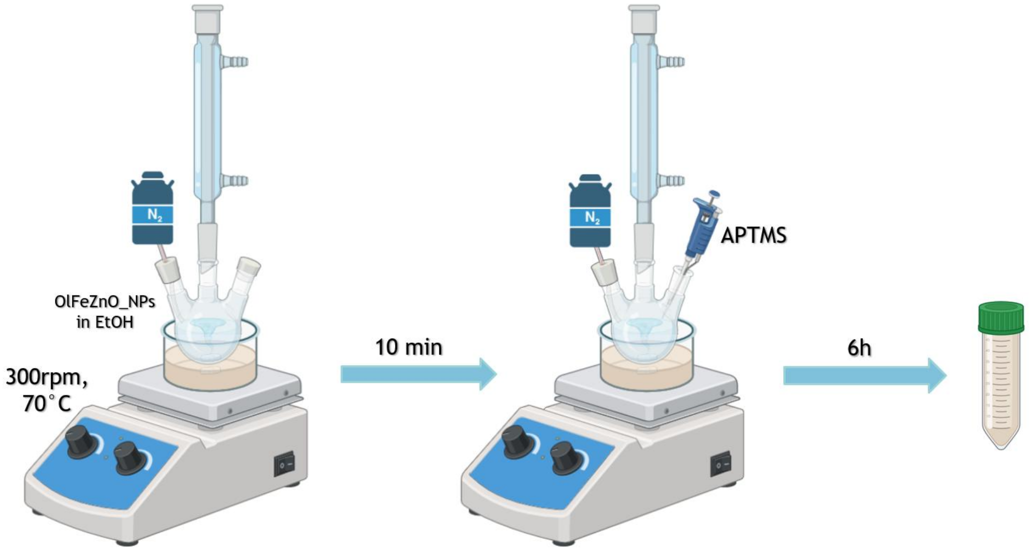

***Figure 4** Schematic overview of the experimental setup used for the amino-functionalization of Fe-doped ZnO nanoparticles (FeZnONH2 NPs). (Image created in BioRender.com)*

2.2.3.1 Evaluation of surface reactivity and amino group loading through fluorescent labeling with ATTO 550

To evaluate the chemical reactivity and the relative density of the amino groups on the nanoparticle surface, a conjugation assay with a fluorescent dye was performed. This experiment aimed to determine whether an increase in the number of surface amino groups correlates with a higher amount of fluorophore successfully coupled to the particles, using

ATTO 550 NHS-ester, which is specifically reactive towards primary amines, as the selected fluorophore.

For the labeling procedure, 400 µg of amino-functionalized nanoparticles, derived from both 1x and 10x batches, were dispersed in 400 µL of pure ethanol to reach final particle concentration of 1mg/mL. Subsequently, 0.8 µL of ATTO 550 stock solution (2 mg/mL) was added to the suspension, maintaining a dye-to-particle ratio of 2 µL/mg. The mixture was incubated overnight under continuous stirring and protected from light to allow the coupling reaction to proceed. Following incubation, the samples were centrifuged three times at 14,000 × g for 10 minutes to ensure the removal of any unbound dye molecules. At each washing step, the supernatant containing the free fluorophore was collected for analysis, and the pellet was redispersed in fresh ethanol.

Both the collected supernatants and the resuspended nanoparticles were analyzed via UV-Vis spectroscopy and Fluorescence Microscopy (using a spinning disk fluorescence-inverted microscope Ti2 Nikon equipped with a crest large FOV laser and a 60×PlanAPO objective, NA = 1.40). The UV-vis absorbance analysis was conducted using a multi-well plate, where three replicates for each sample were measured and subsequently averaged. To ensure accuracy, the background signal was subtracted using pure ethanol as a blank, which corresponds to the medium employed for the sample dispersion. Measurements were performed across the wavelength range from 200 to 800 nm using a Multiskan GO microplate spectrophotometer (Thermo Fisher Scientific).

2.3 Synthesis of zinc oxide quantum dots

Zinc oxide quantum dots (ZnO QDs) were synthesized using two different methods:

1. Method 1

Undoped (ZnO QDs1), iron-doped and amino-functionalized (FeZnONH2 QDs1), and gadolinium-doped (GdZnO QDs1) quantum dots were synthesized following a modified wet chemical method [57].

In detail, a basic solution was prepared by dissolving 14 mmol of potassium hydroxide (KOH) in 8 mL of absolute ethanol (final concentration 1.75 M) and kept at 4 °C until use.

In parallel, 2.195 g of $Zn(CH_3COO)_2 \cdot 2H_2O$, (10 mmol) were dissolved in 60 mL of absolute ethanol. For the synthesis of doped QDs, the specific precursor was added to this solution: 242.4 mg of $Fe(NO_3)_3 \cdot 9H_2O$ (0.6 mmol) for Fe-doping, or 271 mg of $Gd(NO_3)_3 \cdot 6H_2O$ (0.6 mmol) for Gd-doping. These amounts correspond to a nominal dopant/Zn molar ratio of 6 at.%.

To promote hydrolysis, 952 µL of MilliQ water was added to the precursors solution. The mixture was then heated to 78 °C under magnetic stirring and reflux conditions. Once the temperature stabilized, the cold KOH solution was added dropwise to the mixture.

For undoped and Gd-doped QDs, the reaction was allowed to proceed for 1 hour at 78 °C. The final product was then collected and purified through three consecutive cycles of centrifugation (10,000 × g for 5 minutes) and redispersion in ethanol.

For the amino-functionalized iron-doped QDs, a one-pot functionalization step was performed during the synthesis. The reaction was initiated as described above, and 30 minutes after the KOH addition, a solution containing 160 µL of APTMS (approx. 0.9 mmol) dissolved in 600 µL of MilliQ water was injected into the reaction flask. This amount corresponds to approximately 9 mol% with respect to the zinc precursor. The reaction continued for an additional 30 minutes (total reaction time: 1 hour).

Finally, the functionalized QDs were purified following the same washing protocol described for the non-functionalized counterparts.

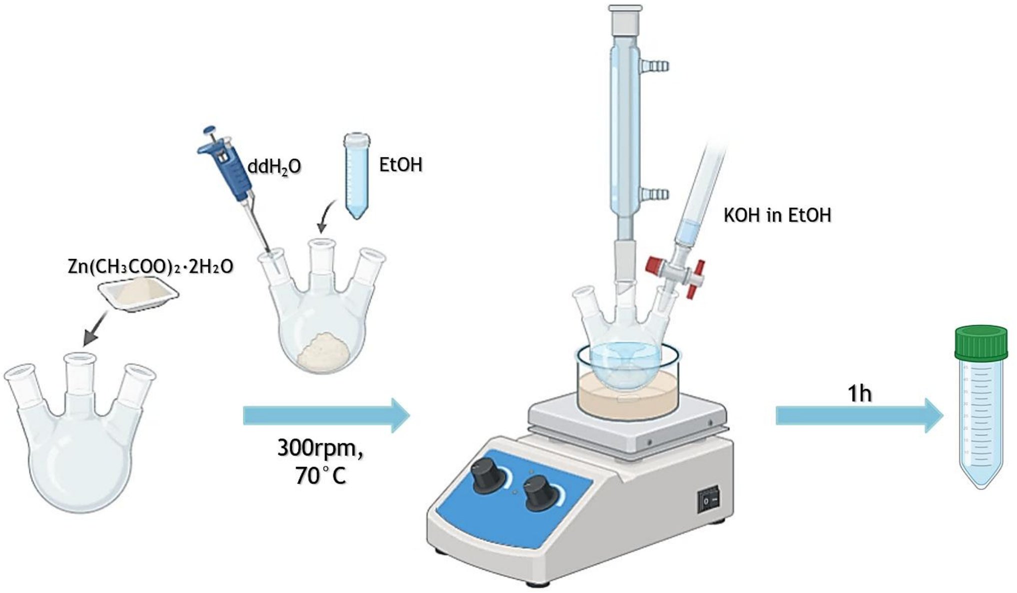

Figure 5 *Schematic overview of the experimental setup used for the preparation of ZnO quantum dots (ZnO QDs1) using method 1. (Image created in BioRender.com)*

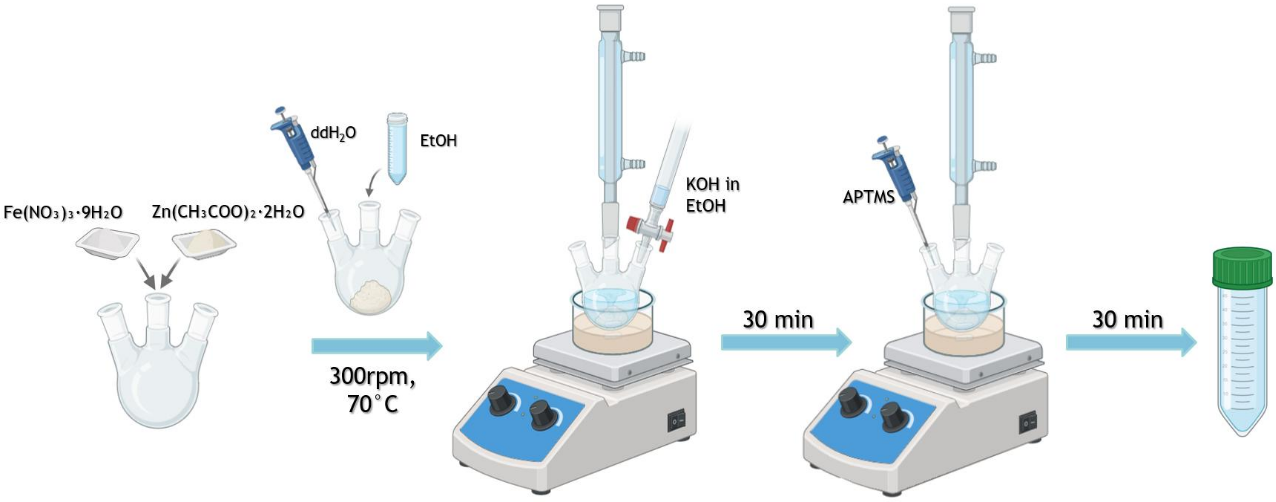

Figure 6 *Schematic overview of the experimental setup used for the preparation of Fe-doped and amino-functionalized ZnO quantum dots (FeZnONH2 QDs1) using method 1. (Image created in BioRender.com)*

2. Method 2

A second typology of zinc oxide quantum dots was synthesized through a wet chemical method adapted from previously reported protocols [23], using methanol as the solvent.

In details, 818.2 mg of $Zn(CH_3COO)_2 \cdot 2H_2O$, corresponding to 3.73 mmol, were dissolved in 42 mL of MeOH in a 100 mL round-bottom flask. The solution was heated to 60 °C under continuous magnetic stirring (350 rpm). To promote precursor dissolution and facilitate hydrolysis, 318 µL of MilliQ water was added to the mixture.
In parallel, a basic solution was prepared by dissolving 288.8 mg of NaOH (7.22 mmol) in 23 mL of methanol. Once the zinc solution reached thermal equilibrium, the NaOH solution was added dropwise into the flask. The reaction was maintained at 60 °C under stirring and allowed to proceed for 2 h ì.

At the end of the reaction, the nanoparticles were purified through three sequential centrifugation cycles. The first washing step was performed in methanol (7000 × g for 5 minutes) to remove reaction byproducts, followed by two subsequent washing and redispersion cycles in ethanol (7000 × g for 5 minutes) to exchange the solvent for the final storage.

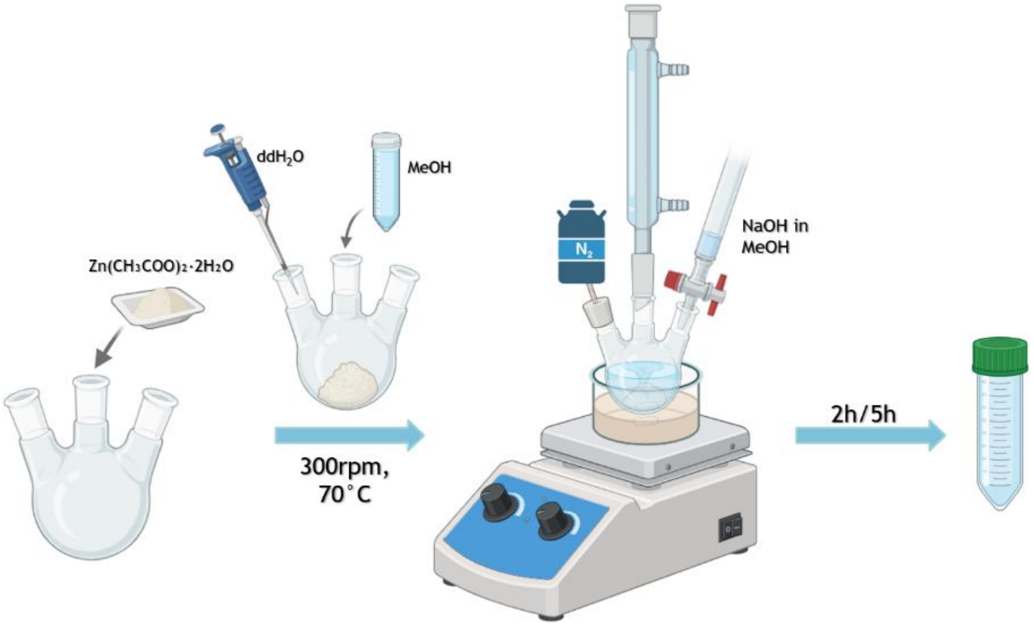

Figure 7 *Schematic overview of the experimental setup used for the preparation of undoped and unfunctionalized ZnO quantum dots (ZnO QDs2) using method 2. (Image created in BioRender.com)*

2.4 Synthesis of mesoporous silica nanoparticles

2.4.1 Synthesis

Mesoporous silica nanoparticles (MSNPs) were synthesized in aqueous conditions using CTAB as the structure-directing agent and TEOS as the silica precursor. The protocol was adapted from a previously reported method [58].

A 0.32 M NH_4OH solution was prepared by diluting 3.84 mL of concentrated ammonia (30-33%) in 200 mL of MilliQ water. Subsequently, 290 mg of CTAB were dissolved in 150 mL of this basic solution within a 200 mL beaker. The mixture was stirred at 50 °C for 1 hour under magnetic

agitation; the formation of a stable vortex was ensured and the beaker was sealed with Parafilm to prevent solvent evaporation.
Then, 3 mL of a TEOS solution (20% v/v in absolute ethanol) was slowly added to the mixture. The beaker was uncovered, and the reaction was maintained under stirring at 50 °C for 1 hour. Stirring was then stopped, and the reaction was allowed to proceed under static conditions at 50 °C overnight. The following day, the colloidal suspension was carefully transferred into a glass bottle, without collecting the last few mL at the bottom to discard any deposited aggregates. The bottle was sealed and subjected to thermal aging in an oven at 70 °C for 24 hours to consolidate the silica network.

Finally, the as-synthesized nanoparticles were collected by centrifugation (12,000 × g, 45 min) and washed with absolute ethanol and MilliQ water to remove unreacted reagents.

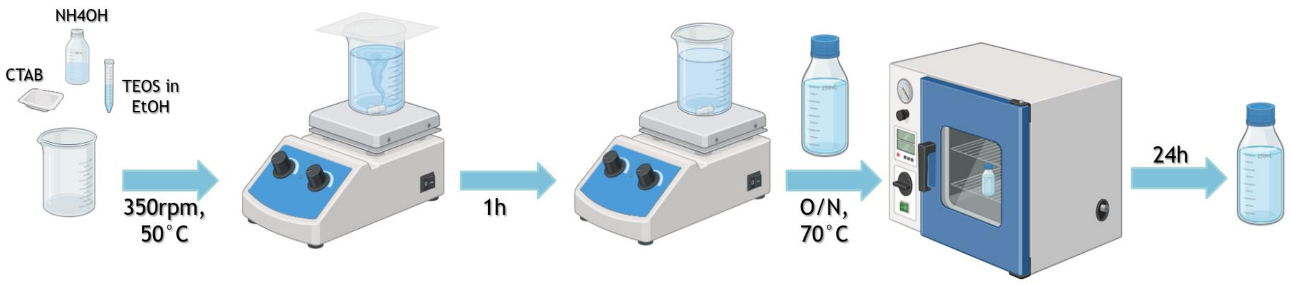

***Figure 8** Schematic overview of the experimental setup used for the preparation of mesoporous silica nanoparticles (MSNPs). (Image created in BioRender.com)*

2.4.2 Template Removal (CTAB Extraction)

The CTAB template was removed from the as-synthesized MSNPs via an ion-exchange extraction process using ammonium nitrate (NH_4NO_3). The extraction solution (10 g/L) was prepared by dissolving 2.5 g of NH_4NO_3 in 250 mL of 95% (v/v) ethanol (composed of 237 mL of absolute ethanol and 13 mL of MilliQ water). To ensure sufficient ionic strength and efficient removal, a ratio of 350 mL of extraction solution per gram of CTAB used in the synthesis was employed.

The ensure complete surfactant removal, two consecutive steps of extraction were performed. First, the nanoparticle pellet was resuspended in the ethanolic NH_4NO_3 solution and kept under magnetic stirring (300 rpm) at 80°C for 2 hours. The nanoparticles were then recovered by centrifugation (12,000 x g, 30 min), washed (one cycle with MilliQ water followed by two cycles with ethanol) and redispersed in fresh extraction solution for a second cycle, which was carried out at 80°C overnight. Finally, the extracted MSNPs were collected by centrifugation (12,000 x g, 45 min) washed and resuspended in ethanol for storage.

2.5 Silica coating

2.5.1 Silica coating after synthesis via ultrasounds (US)

Two distinct sonochemical strategies were employed to coat the FeZnO nanoparticles and the ZnO quantum dots with a dense silica shell. The decision to utilize ultrasonication was driven by the need to effectively overcome particle aggregation during the coating process, while simultaneously providing the additional energy required to promote hydrolysis and condensation reactions. The two experimental protocols differed primarily in the solvent composition, the reaction time, and the specific reagents stoichiometry. To identify the optimal coating conditions, different molar ratios of zinc precursor to catalyst (NH_4OH) and silica source (TEOS) were screened, as summarized in Table 1.

Table 1 *Summary of the experimental conditions for silica coating via ultrasonication. Molar ratio A, B and C were used with Method US1 while D, E, F and G with Method US2 for FeZnO NPs and H and I with Method US2 for FeZnO QDs.*

Sample name	Molar ratios ($ZnO:NH_4OH:TEOS$)
A	1:0.026:0.008
B	1:0.052:0.0016
C	1:2.58:0.3
D	1:0.64:0.06
E	1:0.64:0.04
F	1:0.64:0.03
G	1:0.64:0.01
H	1:0.64:0.04
I	1:0.64:0.01

1. Method US 1

This approach involved a hydrolysis reaction in a water-ethanol mixture.

Fe-doped ZnO nanoparticles were dispersed at a concentration of 1 mg/mL in a solvent mixture consisting of absolute ethanol and deionized water (3:1 v/v ratio). The suspension was sonicated for 3 minutes to ensure homogeneous dispersion.

Subsequently, TEOS was added to the mixture, followed by a second sonication step of 10 minutes. To catalyze the reaction, NH_4OH was introduced, and the process was continued under ultrasonication for an additional 20 minutes.

Three different formulations (Batches A, B, and C) were tested by varying the $ZnO:NH_4OH:TEOS$ molar ratios (see Table 1). The resulting silica-coated nanoparticles were purified through three successive centrifugation and redispersion cycles in ethanol at 12,000 × g for 10 minutes each, to remove unreacted precursors.

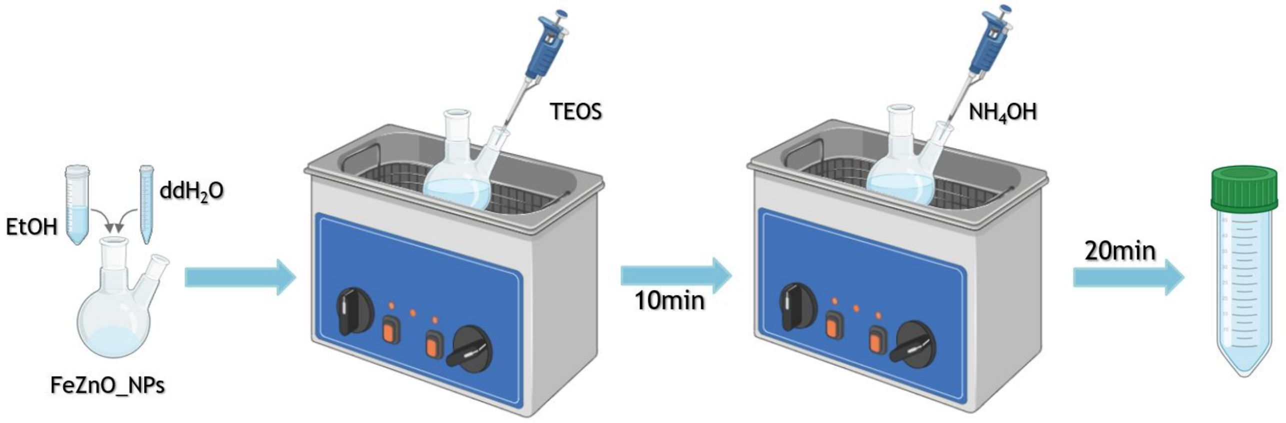

Figure 9 *Schematic overview of the experimental setup used for the silica coating of nanoparticles via ultrasound using Method US 1. (Image created in BioRender.com)*

2. Method US 2

This procedure was performed in a predominantly ethanolic environment to modulate the hydrolysis rate to coat both Fe-doped ZnO nanoparticles (FeZnO NPs) and ZnO quantum dots. The particles were dispersed in 5 mL of absolute ethanol at a concentration of 1 mg/mL and TEOS was added to the mixture. Immediately after TEOS, ammonium hydroxide previously dissolved in ethanol was added to the flask to trigger the reaction, and the mixture was maintained under continuous sonication for 30 minutes. In this set of experiments, the ZnO:NH_4OH ratio was kept constant while the amount of TEOS was varied across four different batches, labeled as D, E, F, and G for the nanoparticles and as H and I for quantum dots, to tune the shell thickness. The washing steps were performed as described above.

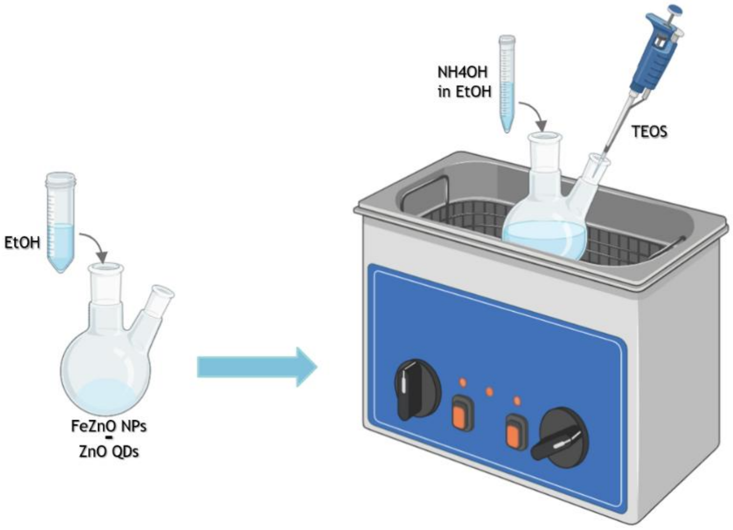

Figure 10 *Schematic overview of the experimental setup used for the silica coating of nanoparticles via ultrasound using Method US 2. (Image created in BioRender.com)*

2.5.2 Silica coating after synthesis via wet-chemical method

An alternative attempt to grow a silica shell on the surface of the quantum dots was performed through wet chemical process in water at high temperature.

In detail, 100 mg of uncoated quantum dots (ZnO QDs1) were dispersed in 25 mL of MilliQ water, resulting in a final concentration of 4 mg/mL. The suspension was transferred to a round-bottom flask and heated to 100 °C under continuous magnetic stirring and reflux conditions. To prevent potential oxidation and ensure a controlled reaction environment, the system was kept under a nitrogen atmosphere (N_2 flow).
Once the suspension reached thermal equilibrium at 100 °C, the silica precursor was introduced. Specifically, TEOS, previously diluted in 600 µL of absolute ethanol, was injected into the mixture.
To optimize the shell thickness, two different TEOS concentrations were tested, corresponding to a molar ratio of 5% and 20% relative to the total molar amount of zinc oxide (ZnO).

The reaction was allowed to proceed for 3 hours. Finally, the resulting silica-coated QDs were collected and purified through three consecutive washing cycles with ethanol, using centrifugation at 12,000 × g for 10 minutes to remove unreacted precursors.

2.5.3 Silica coating during synthesis via wet-chemical method

To try to achieve a silica coating directly during the nucleation and growth phase, a modification was applied to the QDs2 synthesis protocol described in Section 2.3.2.

Specifically, following the addition of NaOH, TEOS was added dropwise to the reaction mixture at a molar ratio of 30% relative to the zinc acetate dihydrate precursor. The reaction was then carried out maintaining the same temperature and stirring conditions reported for the uncoated counterparts. The final product was purified through three consecutive washing cycles in absolute ethanol, collecting the particles by centrifugation at 12,000 × g for 10 minutes to ensure the complete removal of unreacted silanes and byproducts.

2.6 Lipid coating of quantum dots via microfluidic mixing system

To improve the biostability of the QDs, a novel lipidic coating method was investigated utilizing a microfluidic approach. To evaluate the effectiveness of this coating process on inorganic nanoparticles, three distinct lipid formulations were employed, with the specific objective of investigating how surface charge influences the formation and stability of the lipid shell: cationic (denoted as 3C+), anionic (3C-), and zwitterionic (2CN).
The coating process was performed using a Staggered Herringbone Micromixer (SHM) chip (Fluidic 1460 Structure A, microfluidic ChipShop, Jena, Germany).
The flow rates were strictly controlled using a microfluidic pressure controller (OB1 MK4, Elveflow, Paris, France), a system previously validated to produce liposomes and lipid nanoparticles [59].
The lipid organic phase was prepared by dissolving the specific lipid formulations (composition, molecular weights, and molar ratios detailed in Tables 2 and 3) in absolute ethanol to a final concentration of 2 mg/mL. Lipid mixtures were obtained by withdrawing

specific aliquots from chloroform or dichloromethane stock solutions (total weight 0.8 mg) that were died together under vacuum in clean glass vials. The aqueous phase consisted of the QD suspension. Specifically, 1.6 mg of QDs were collected by centrifugation at 14,000 × g for 10 min and resuspended in 1.2 mL of Milli-Q water to achieve an initial particle concentration of 1.33 mg/mL.

The lipid-coated particles were fabricated by injecting the two phases into the micromixer with a Flow Rate Ratio (FRR) of 3:1 (aqueous phase/organic phase) and a Total Flow Rate (TFR) of 1 mL/min. These process parameters ensured a final lipid-to-nanoparticle weight ratio of 1:2, resulting in final concentrations of 1 mg/mL for the QDs and 500 µg/mL for the lipids in the collected output.

Table 2 *List of lipid species used in the coating formulations, reported with their respective molecular weights and abbreviations.*

Lipid Type	Lipids	Molecular Weight (g/mol)
Charged	18:1 PA or DOTAP	722.948 or 698.54
Structural	DOPC	786.113
Sterol	Cholesterol	386.654
PEGylated	DSPE-PEG-amine	2790.486

Table 3 *List of the lipid formulations used, reporting the specific lipid components and their relative molar ratios (%).*

Lipidic Formulation			
	3C-	*2CN*	*3C+*
Lipids	***Molar Ratio***		
18:1 PA	*50%*	*-*	*-*
DOTAP	*-*		*50%*
DOPC	*10%*	*60%*	*10%*
Cholesterol	*38.5%*	*38.5%*	*38.5%*
DSPE-PEG-amine	*1.5%*	*1.5%*	*1.5%*

2.7 Nanoparticles characterization

2.7.1 Dynamic Light Scattering (DLS) and Z-Potential

The characterization of the synthesized nanoparticles involved measuring their hydrodynamic size distribution, and surface charge using Dynamic Light Scattering (DLS) and Zeta potential analysis.

DLS is a non-invasive technique that determines the size of particles in suspension by analyzing the intensity fluctuations of scattered light. When a laser beam passes through a colloidal solution, particles smaller than the wavelength of the incident light scatter it in all directions (Rayleigh scattering). Due to the Brownian motion of the particles, the distance between scatterers changes continuously, causing constructive or destructive interference that results in intensity fluctuations over time. These variations contain information about the time scale of movement, which depends on the particle size: smaller particles move more rapidly, while larger ones move more slowly. [60]

Mathematically, the dynamics of the particles are obtained through an intensity auto-correlation function, which is commonly referred to as ACF. In the presence of monodisperse systems, this function follows a model based on a single exponential decay, where the calculated decay rate is intrinsically linked to the translational diffusion coefficient. Consequently, the Stokes-Einstein equation, reported below, allows for the determination of the hydrodynamic diameter starting from the diffusion value.

$$d_H = \frac{K_B T}{3\pi\eta D}$$

Where:

- K_B is the Boltzmann constant
- T is the absolute temperature
- η is the viscosity of the dispersant
- D is the translational diffusion coefficient

To evaluate the colloidal stability and surface charge of the nanoparticles, Zeta potential (ζ) measurements were performed. Charged nanoparticles in suspension form an Electrical Double Layer (EDL) consisting of an inner "Stern layer" of firmly bound ions and an outer "Diffuse layer," where interactions are weaker. When an electric field is applied, the electrophoretic effect causes charged particles to move toward the opposite electrode. The potential measured at the slipping plane - the interface within the diffuse layer separating the moving particle from the bulk dispersant - is defined as the Zeta potential. This value is calculated from the measured electrophoretic mobility (μ_E) using Henry's equation:

$$\mu_E = \frac{2\varepsilon\zeta f(ka)}{3\eta}$$

Where:

- μ_E the electrophoretic mobility,
- ε is the dielectric constant of the medium,
- ζ is the Zeta potential,
- $f(ka)$ is Henry's function (typically approximate to 1.5 using the Smoluchowski approximation for aqueous media),
- η is the viscosity of the medium.

All measurements were performed using a Zetasizer Nano ZS90 (Malvern Instruments, Worcestershire, UK) equipped with a 4-mW He-Ne laser (633nm).

Prior to analysis, nanoparticle suspensions were prepared to achieve a final concentration of 100 μg/mL.

The preparation protocol differed based on the dispersant:

- for analysis in ethanol, an aliquot of the stock suspension containing 100 μg of particles was sonicated for 10 minutes, and the volume was adjusted to 1 mL with absolute ethanol;

- for analysis in water, to ensure proper change of solvent, the sample was first centrifuged at 14,000 × g for 10 minutes. The supernatant was discarded, and the pellet was redispersed in 1 mL of MilliQ water; before each measurement, samples were sonicated and vortexed to ensure homogeneity.

For size determination, 50 µL of the suspension was loaded into a disposable micro-cuvette. Measurements were performed in triplicate.

Following DLS analysis, 850 µL of the aqueous suspension was transferred into a folded capillary cell (DTS1070) for Zeta potential analysis, taking care to avoid bubble formation. Measurements were conducted at 25 °C in water; the protocol included an equilibration time of 10 seconds, with an automatic attenuator adjusting the laser power. Zeta potential data were collected in triplicate.

2.7.1.1 Field Emission Scanning Electron Microscopy (FESEM)

Field Emission Scanning Electron Microscopy (FESEM) is a high-resolution imaging technique employed to analyze the morphology, size, and topography of nanostructures.

Unlike conventional SEM, FESEM utilizes a field emission cathode, typically consisting of a sharp monocrystalline tungsten tip. When a high electrical field gradient is applied, this tip generates a narrow, coherent beam of electrons with high current density. This configuration significantly enhances spatial resolution and minimizes sample charging and thermal damage, making it ideal for characterizing sensitive nanomaterials.

As the focused electron beam scans the specimen surface, it interacts with the atoms of the material, generating various signals. The most relevant for morphological analysis are secondary electrons (SE), which originate from the near-surface regions of the sample. These electrons are collected by a detector and converted into an electronic signal to produce highly detailed images with a large depth of field, allowing for the visualization of the three-dimensional structure of the nanoparticles.

The morphological investigation of the synthesized nanoparticles was performed using a SUPRA 40 (Zeiss) field emission scanning electron microscope.

To prepare the samples for analysis, nanoparticles were dispersed in either absolute ethanol or MilliQ water, depending on the optimal dispersant for each specific formulation, at a concentration of 50 µg/mL. An aliquot of the dilute suspension was deposited dropwise onto a flat silicon wafer substrate.

Once dried, the silicon substrate was mounted onto an aluminum sample holder using conductive carbon adhesive tape to ensure proper grounding. The images were acquired via an accelerating voltage (EHT) of 5.00 kV and an aperture size of 30.00 µm, at a working distance of approximately 3-4 mm.

The FESEM micrographs were subsequently analyzed using the open-source software ImageJ (National Institutes of Health, USA). The average particle size and size distribution were determined by manually measuring the diameter of at least 60 particles selected from different acquisition areas to ensure statistical significance.

2.7.2 X-Ray Diffraction (XRD)

X-Ray Diffraction (XRD) is a non-destructive analytical technique used to determine the crystallinity, identify polymorphic forms, and analyze the crystal structure and orientation of nanomaterials. The fundamental principle relies on the interaction between a monochromatic X-ray beam and the atoms within a crystal lattice. Since X-rays possess a wavelength (λ) comparable to the interatomic spacing, their collision with the sample induces elastic scattering: the energy is absorbed by the electrons and re-emitted as new X-rays with the same energy.

The interference between these scattered rays can be constructive or destructive. Constructive interference - defined as diffraction - occurs only when the specific conditions of Bragg's Law are met:

$$n\lambda = 2d \sin\theta$$

Where:

- n is an integer number (order of reflection);
- λ is the wavelength of the incident X-ray beam;
- d is the interplanar spacing (distance between adjacent atomic planes);
- θ is the angle of diffraction.

The resulting diffractogram plots the intensity of the diffracted beam as a function of the diffraction angles θ. Since every crystalline structure produces a unique diffraction pattern, this output acts as a specific "fingerprint," allowing for the identification of the synthesized phases by comparing the measured peaks against standard reference patterns.

Sample preparation was critical to ensure a homogeneous and sufficiently thick layer for analysis. An amount corresponding to 1 mg of nanoparticles was collected by centrifugation at 14,000 × g for 10 minutes. After discarding the supernatant, the pellet was resuspended in 50 µL of fresh solvent (absolute ethanol or MilliQ water, depending on the optimal dispersion medium). The concentrated suspension was then deposited onto a silicon wafer substrate applying 10 µL at a time and allowing each layer to dry completely before adding the next. A bare silicon substrate was analyzed as a control background.

Measurements were performed using a Panalytical X'Pert PRO diffractometer in the Bragg-Brentano geometry with a Cu-Kα radiation source operating at 40 kV and 30 mA. The diffraction patterns were collected in the 2θ angular range of 10°–60°, with a step size of 0.026° and a total acquisition time of 10 minutes.

Post-acquisition, the diffraction patterns were analyzed to estimate the average crystallite size (grain dimension) of the nanoparticles. The calculation relies on the observation that the width of the diffraction peaks is inversely proportional to the size of the crystalline domains. This relationship is described by the Debye-Scherrer equation:

$$D = \frac{K\lambda}{\beta \cos \theta}$$

Where:

- D is the average crystallite size;
- K is the shape factor (dimensionless constant), approximated to 0.9 to account for the spherical shape of the grains;
- λ is the X-ray wavelength (1.54 Å);
- β (or $\Delta 2\theta$) is the line broadening at half the maximum intensity (Full Width at Half Maximum, FWHM), expressed in radians;
- θ is the Bragg angle of the selected peak.

To ensure an accurate estimation, the Full Width at Half Maximum (β) was determined through mathematical fitting using GraphPad Prism software. The analysis focused on the most prominent diffraction peak. Specifically, a non-linear regression analysis was performed using a Gaussian function that included a baseline parameter.

This approach was necessary to properly model the peak shape and prevent convergence artifacts caused by the non-zero experimental background. The resulting FWHM value was then substituted into the Scherrer equation to quantify the average grain dimension of the synthesized materials.

2.7.3 Determination of Zinc and Silica content via UV-Vis spectroscopy

To quantify the zinc content within the core-shell nanostructures and indirectly estimate the amount of silica deposited, UV-Vis spectroscopy was employed. This method relies on the optical transparency of the amorphous silica shell across the analyzed spectral range; therefore, the absorbance profile detected in the coated samples is attributed exclusively to the ZnO content of the core.

A comparative analysis was performed by preparing parallel sets of reference solutions (uncoated FeZnO) and sample dilutions (FeZnO@ SiO_2) to verify the concentration consistency at different points. Specifically, three reference standards of Fe-ZnO were prepared at known concentrations of 0.2 mg/mL, 0.1 mg/mL, and 0.05 mg/mL. Correspondingly, the silica-coated sample suspension was diluted in MilliQ water with dilution factors of 1:2, 1:4, and 1:8.

The ZnO concentration in the coated samples was determined using a comparison method based on the Lambert-Beer law. Each diluted sample was compared to its corresponding reference standard (i.e., 1:2 vs 0.2 mg/mL; 1:4 vs 0.1 mg/mL; 1:8 vs 0.05 mg/mL).

The concentration of the unknown diluted samples ($C_{diluited}$) was calculated using the ratio of their absorbance (A_{sample}) relative to the absorbance of the paired reference standard (A_{ref}):

$$C_{diluited} = C_{ref} \times \frac{A_{sample}}{A_{ref}}$$

This calculation was performed for each pair to ensure linearity and robustness of the quantification. The actual concentration of the undiluted silica-coated suspension (C_{SiO2}) was then derived by multiplying the calculated value by the respective dilution factor (d), confirming that:

$$C_{SiO2} = 2 \cdot C_{1:2} \approx 4 \cdot C_{1:4} \approx 8 \cdot C_{1:8}$$

Finally, the mass of the silica shell was estimated by difference. Knowing the total mass of the recovered core-shell powder (total reaction yield) and the quantified mass of the ZnO core derived from the spectroscopic analysis, the silica content was determined as:

$$Mass_{SiO2} = Mass_{Total\ Yeld} - Mass_{ZnO\ Quantified}$$

2.8 In vitro biological assessment

2.8.1 A549 human lung carcinoma cells and cell culture

The human lung adenocarcinoma cell line, A549, was selected as a representative in vitro tumor model to evaluate the biological interaction and potential toxicity of the synthesized nanoparticles. Established in 1972, this cell line is widely recognized as a standard in nanotoxicology and pharmacology research, because it retains key morphological and biochemical features of native Type II alveolar epithelial cells [61,62]. In the physiological context, Type II cells play a pivotal role and, although they cover a smaller surface area compared to Type I cells, they remain functionally distinct and metabolically active [63,64]. These cells are responsible for the synthesis of surfactant, which is stored in lamellar bodies, and possess cytochrome P450 isozymes, suggesting a significant capability for oxidative drug metabolism [65]. Furthermore, these cells exhibit well-characterized endocytic properties, making them an ideal substrate to study nanoparticle uptake and intracellular interaction mechanisms [64–66]. Consequently, the choice of A549 cells allows for a reliable assessment of the core-shell systems' biocompatibility, providing data on cytotoxicity and cell viability that are robust and comparable with the existing literature on inorganic nanomaterials.

For the in vitro biological assays, the cells were cultured in Dulbecco's Modified Eagle Medium (DMEM) supplemented with 1% L-glutamine, 1% penicillin-streptomycin, and 10% Fetal Bovine Serum (FBS). The cultures were maintained in 25 cm^2 flasks (T25) at 37 °C in a humidified atmosphere containing 5% CO_2.
Routine subculturing was performed when the cell monolayer reached near-confluence (approximately 80-90%). To detach the adherent cells, the spent culture medium was first removed, and the monolayer was washed with approximately 2 mL of Phosphate-Buffered Saline (PBS) to eliminate residual serum proteins, which can inhibit the enzymatic activity of trypsin.
Subsequently, 1 mL of trypsin solution was added to the flask, which was then incubated at 37 °C for 5 minutes to facilitate cell detachment. The enzymatic reaction was neutralized by

adding 2 to 3 mL of complete growth medium (containing FBS). The resulting cell suspension was collected in a sterile conical tube.

For cell quantification, a 10 µL aliquot of the suspension was mixed with an equal volume (10 µL) of Trypan Blue dye to exclude non-viable cells. The viable cell concentration (live count) was determined using an automated cell counter (BioRad). Based on the calculated density (cells/mL), an appropriate volume of the suspension containing approximately 150,000 cells was transferred into a new T25 flask containing 5 mL of fresh medium for maintenance.

2.8.2 Cytotoxicity assay (WST-1)

Cell viability was assessed using the WST-1 cell proliferation assay (Roche). A549 cells were seeded into 96-well plates at a density of 1,250 cells/well in a final volume of 100 µL of complete medium. To prevent experimental bias caused by medium evaporation or uneven thermal distribution, the peripheral wells were filled with sterile PBS and excluded from the analysis. The plates were then incubated for 24 hours at 37 °C to ensure proper cell attachment and recovery.

Following the 24-hour stabilization period, treatment suspensions were prepared. Specifically, 250 µg of FeZnO and Silica-coated FeZnO (FeZnO@SiO2) nanoparticles were centrifuged and resuspended in sterile MilliQ water to obtain a stock concentration of 1 mg/mL. To ensure a precise toxicological comparison, the weight of the core-shell particles was adjusted based on the ZnO content, ensuring that the concentration of the active metal oxide remained comparable across all samples regardless of the presence of the silica shell.

These stock solutions were then serially diluted in the culture medium to reach the final testing concentrations of 100, 50, 25, and 12.5 µg/mL. The spent medium was removed from the wells and replaced with 100 µL of the nanoparticle-containing medium. The experimental layout was designed to include 4 technical replicates for each condition, along with a specific background well (medium with nanoparticles but without cells) for each concentration to correct for any optical interference caused by the nanomaterials. An untreated control group (cells with medium only) was included as a reference.

Cytotoxicity was evaluated at two distinct time points: 24 hours and 48 hours post-treatment. At each time step, 10 µL of WST-1 reagent was added to each well, incubating the plate for 1 hour at 37 °C to allow the metabolic conversion of the tetrazolium salt into the formazan dye. Finally, the absorbance was measured at 450 nm with 620 nm as reference wavelength using a Multiskan GO microplate spectrophotometer (Thermo Fisher). The assay was performed in three independent biological replicates, with four technical replicates for each experimental condition. The absorbance values from the technical replicates were averaged, and the specific background was subtracted from each sample. The viability of untreated control cells was set to 100% and the percentage of cell viability for cells treated with different amounts of NPs was calculated relative to the untreated control using the following equation:

$$\% \, Cell \, Viability = \left(\frac{OD_{sample} - OD_{background}}{OD_{control} - OD_{background}} \right) \times 100$$

Where:

- $\mathrm{OD}_{\mathrm{sample}}$ is the absorbance of the nanoparticle-treated cells;
- $\mathrm{OD}_{\mathrm{background}}$ is the absorbance of the corresponding background well;
- $\mathrm{OD}_{\mathrm{control}}$ is the mean absorbance of the untreated control cells;

All data were expressed as the mean ± standard deviation of three independent biological replicates. Statistical analysis was performed with GraphPad Prism software (version 9.5.0), using a two-way analysis of variance (ANOVA) followed by a Sidak post-hoc test to compare the effect of different NP types at the same concentration. A p-value of less than 0.05 was considered statistically significant.

3 Results and Discussion

3.1 Synthesis of ZnO nanostructures

The synthesis of Zinc Oxide nanostructures, encompassing both nanoparticles and quantum dots, was carried out following a wet chemical hydrolysis protocol. This synthetic approach was selected for its proven efficacy in producing high-purity nanostructured materials with precise stoichiometric control [67]. Compared to other techniques, wet chemistry offers significant advantages, including the use of mild processing temperatures [68], and the use of environmentally sustainable solvents, such as ethanol and water [69].

The formation of the metal oxide nanostructures is driven by hydrolysis and condensation mechanisms. The zinc precursor (normally zinc acetate or nitrate) reacts with the mineralizing agent (like alkaline hydroxides or TMAH), which provides the hydroxyl ions (OH-) necessary to trigger nucleation. The chemical pathway leading to the formation of ZnO crystals can be described by the following reactions:

$$Zn^{2+} + \, 2OH^- \rightarrow Zn(OH)_2$$

$$Zn(OH)_2 + \, 2OH^- \rightarrow [Zn(OH)_4]^{2-}$$

$$[Zn(OH)_4]^{2-} \rightarrow ZnO \; + H_2O + \, 2OH^-$$

To achieve doping, the dopant precursor is normally introduced into the reaction mixture prior to the addition of the base. This step is critical to promote the homogeneous incorporation of ions into the zinc oxide host lattice during the initial nucleation phase, thereby minimizing the formation of separate phases.

The choice of experimental parameters, as the alkali base and organic solvent, the ratio between reagents and the reaction temperature and time, drastically influences growth kinetics and final morphological, physical and chemical properties of the nanomaterials [70,71].

3.2 Oleic Acid Fe-doped ZnO nanoparticles (OlFeZnO NPs)

Iron-doped (6 at%) ZnO NPs with oleic acid capping (OlFeZnO NPs) were synthetized by an optimized wet-chemical method [72]

The synthesized OlFeZnO NPs underwent a comprehensive physicochemical characterization to study the morphological, structural, and colloidal properties. The analysis focused on evaluating the hydrodynamic size, Polydispersity Index (PdI), and surface charge via DLS, as well as determining the primary particle morphology through FESEM and the crystalline composition via XRD. A summary of the quantitative data obtained is presented in Table 5, including DLS metrics, the primary size derived from FESEM, and the crystallite dimensions calculated from XRD.

To determine the particle size and morphology FESEM analysis was performed. The micrograph (Figure 11a) and the corresponding size distribution histogram (Figure 11b) reveal that the OlFeZnO NPs possess a uniform morphology. The analysis of the particle size distribution identified a predominant diameter of 9.5 nm.

The phase purity and crystallinity were investigated using XRD, where the diffraction pattern, shown in Figure 11c, is consistent with the hexagonal wurtzite phase of Zinc Oxide. The analysis reveals the characteristic peaks at (100), (002), and (101), which confirm the crystalline structure of the material. Crucially, the introduction of Oleic Acid did not induce any lattice distortion nor the formation of new crystalline features, confirming that the stabilizer does not incorporate into the ZnO crystal lattice. In contrast, the broad amorphous band present in the pattern could be attributed to the presence of oleic acid molecules on the nanoparticle surface. Moreover, no additional peaks corresponding to metallic Fe or iron oxide phases were observed. Quantitatively, the average crystallite size was calculated using the Debye-Scherrer equation as described in section 2.7.2, yielding a value of 10.97 nm. Interestingly, the calculated crystallite size (10.97 nm) is in excellent agreement with the physical diameter measured by FESEM analysis (9-10 nm), confirming the single-crystal nature of the nanoparticles.

To evaluate the behavior of the nanoparticles in suspension, the hydrodynamic size was analyzed via DLS. The measurements, shown in Figure 11d, revealed a main population with hydrodynamic diameter centered around 150 nm in both ethanol and water. The result differs from primary particle size measured by FESEM technique. Indeed, FESEM analysis validates the efficacy of the wet chemical protocol in controlling crystal growth at the nanoscale, while the DLS data provides information on the colloidal behavior of nanoparticles in solution, measuring the size of the particles moving in the liquid medium, inclusive of their hydrodynamic shell. However, the considerable discrepancy between DLS and FESEM dimensions suggested the presence of loose aggregates or clusters in the polar solvent. This could derive from the reorganization of ZnO nanocrystals after nucleation to minimize their overall surface energy, a phenomenon widely reported in literature and compatible with the low amount of oleic acid capping used [73].

Finally, the surface charge was investigated, resulting in a Zeta potential of 34.4 mV, which indicates a remarkable surface positive charge.

Table 4 *Physicochemical properties of Oleic Acid-capped Fe-doped ZnO nanoparticles (OlFeZnO NPs), reporting DLS data (Size and PdI in ethanol/water), Zeta Potential, crystallite size (XRD), and primary particle diameter (FESEM).*

Z-Aver_EtOH	PDI_EtOH	Z-Aver_H2O	PDI_H2O	ζ-Pot(mV)	Crystallite size (Scherrer)	FESEM diameter
157.6	0.13	143.5	0.18	34.3	10.97nm	10nm

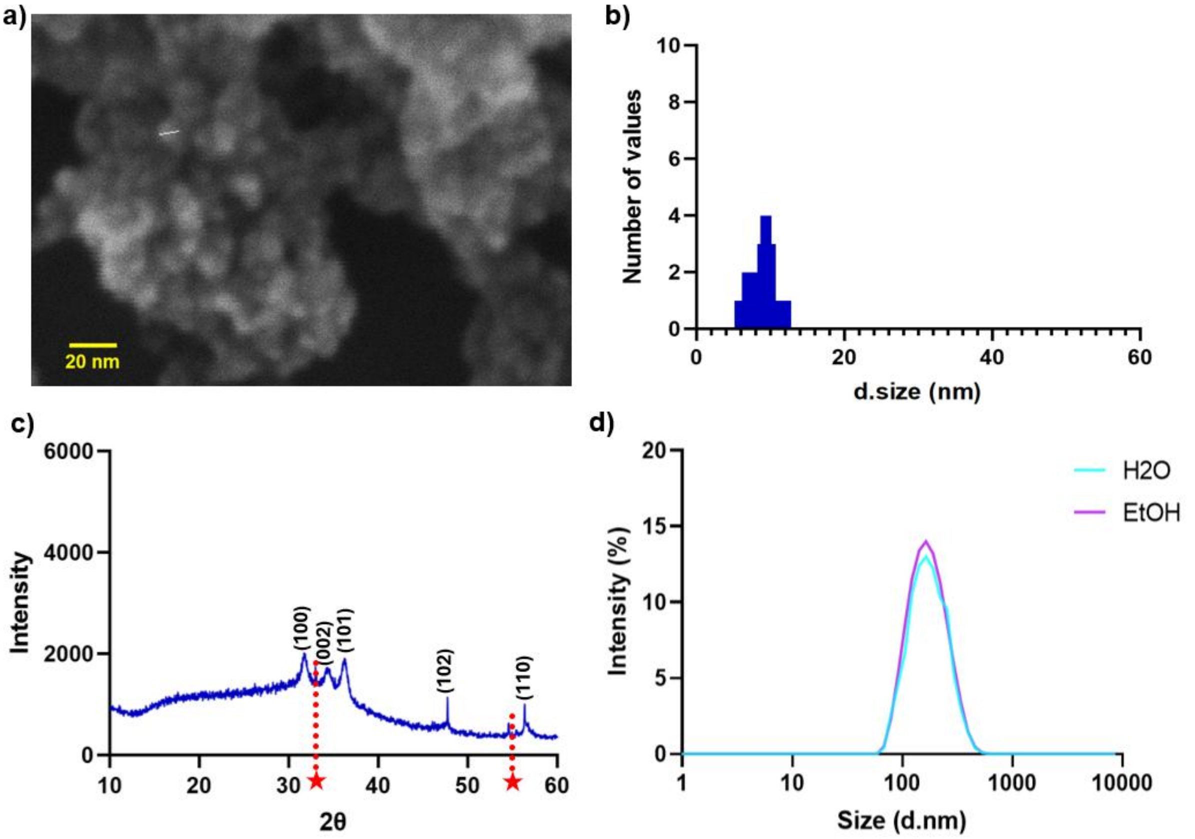

Figure 11 *Physicochemical characterization of Oleic Acid-capped Fe-doped ZnO nanoparticles (OlFeZnO NPs). (a) FESEM micrograph of the nanoparticles; the white segment illustrates the method used for diameter measurement. (b) Histogram representing particle size distribution based on FESEM measurement. (c) X-Ray Diffraction (XRD) pattern; the red stars indicate the diffraction peaks arising from the silicon substrate background. (d) Hydrodynamic size distribution profiles measured via DLS in water (H_2O) and ethanol (EtOH).*

3.3 Amino-functionalized Oleic Acid-capped Fe-doped ZnO nanoparticles (OlFeZnONH2 NPs)

To introduce specific reactive sites for further surface modification and provide reactive sites for dye conjugation, the nanoparticles were functionalized with amino-propyl groups using APTMS. Two different silane concentrations were investigated to optimize the surface density of amino groups: 10% molar ratio with respect to the total ZnO amount (denoted as 1x) and a ten times higher concentration (denoted as 10x).

The functionalized samples underwent a comprehensive characterization including FESEM, XRD and DLS, as the previous sample. The data obtained are summarized in Table 6. To facilitate a direct assessment of the functionalization effect, the table reports the data for the unfunctionalized nanoparticles (first row) alongside the results for the two functionalized samples (1x and 10x, second and third rows, respectively).

FESEM micrographs (Figure 12a regarding the 1x sample and b for the 10x sample) show that the particle integrity was preserved during the functionalization process. Both samples display a uniform, quasi-spherical morphology. The analysis identified a predominant diameter of 8 nm for both the 1x sample and 10x sample. These values are consistent with the dimensions of the core nanoparticles discussed in the previous section.

The crystalline structure of the functionalized samples was analyzed by XRD. As shown in Figure 12c for the 1x sample, d for the 10x sample, both the 1x and 10x samples retained the hexagonal wurtzite structure of ZnO, confirming that the silanization process did not induce phase change. Quantitatively, the average crystallite size calculated using the Debye-Scherrer equation was 10.94 nm for the 1x sample and 11.57 nm for the 10x sample, values which are in good agreement with the FESEM measurements.

The impact of the amino-silane shell on colloidal stability was evaluated by comparing the hydrodynamic size of the functionalized particles against the starting synthesis batch. The DLS profiles (Figure 12e and 12f) provide a characterization of the nanoparticles in ethanol and water, respectively in ethanol, the 1x sample exhibited a mean hydrodynamic diameter centered around 140 nm, while the 10x sample showed a value of approximately 125 nm. When comparing these results to the unfunctionalized oleic acid-capped NPs, which displayed a diameter of about 150 nm, the variations observed appear relatively limited, suggesting that the particles maintain a comparable dispersion state across the different batches. Similar results were obtained for the three types of NPs resuspended in water.

Regarding the surface charge, the Zeta potential was investigated for the three samples. The measurement indicates that the surface remains strongly positive in all cases (between 30 and 35 mV). However, the differences between the samples are too small to definitively confirm the presence of the amino groups, a parameter that is subsequently validated through the conjugation of amino reactive fluorescent molecules.

Table 5 *Physicochemical properties of Amino-functionalized Oleic Acid-capped Fe-doped ZnO nanoparticles (OlFeZnONH2 NPs), reporting DLS data (Size and PdI in ethanol/water), Zeta Potential, crystallite size (XRD), and primary particle diameter (FESEM). Unfunctionalized nanoparticles are shown in first row, 1x and 10x in second and third rows respectively.*

Sample	Z-Aver_EtOH	PDI_EtOH	Z-Aver_H2O	PDI_H2O	ζ-Pot(mV)	Crystallite size (Scherrer)	FESEM diameter
OlFeZnO	157.6	0.13	143.5	0.18	34.3	10.97nm	9.5nm
OlFeZnONH2 1x	128	0.13	153.9	0.12	32.8	10.94nm	7.9nm
OlFeZnONH2 10x	127.8	0.13	124.9	0.14	30.2	11.57nm	8.1nm

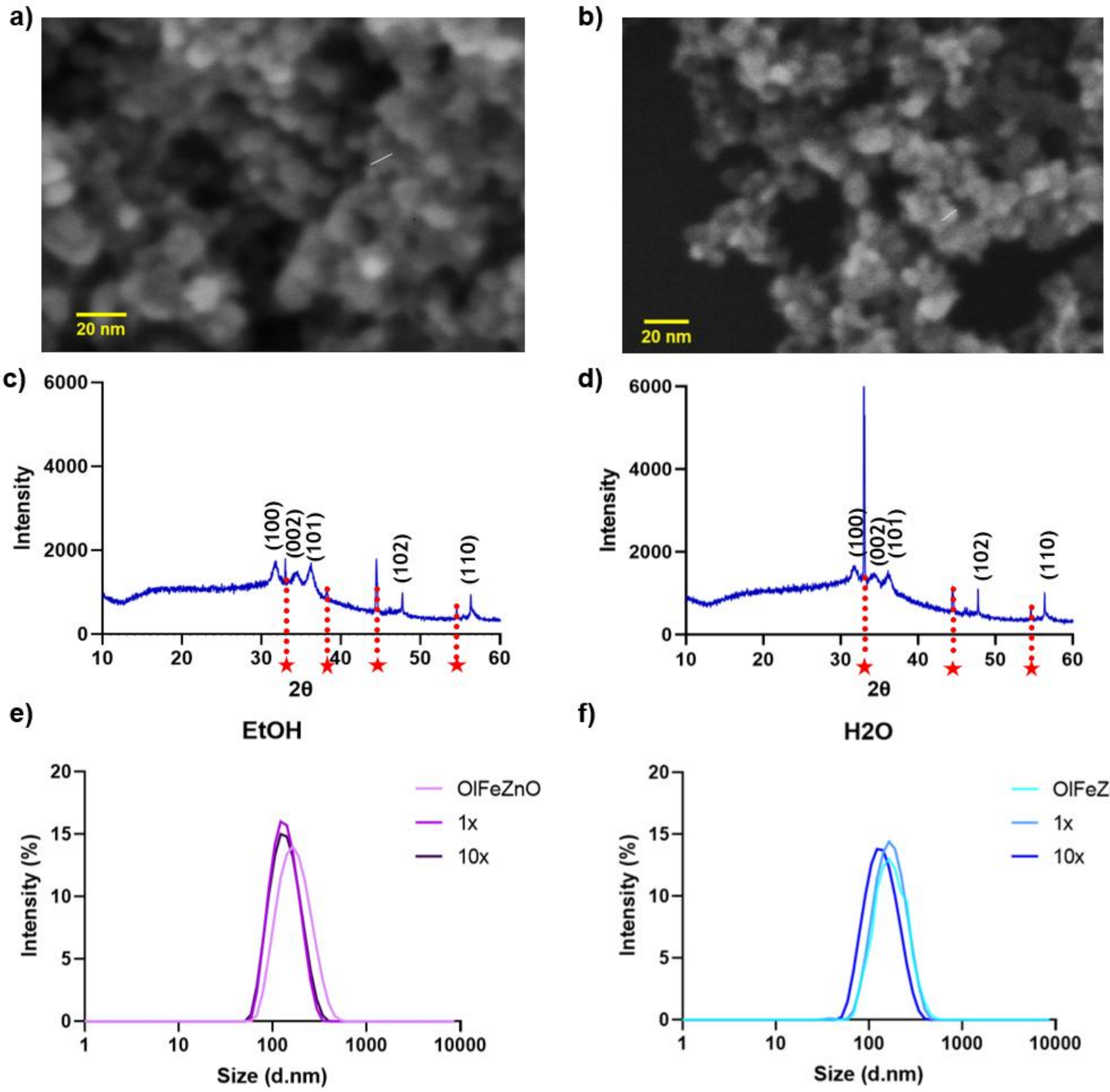

Figure 12 *Physicochemical characterization of Amino-functionalized Oleic Acid-capped Fe-doped ZnO nanoparticles (OlFeZnONH2 NPs). (a-b) FESEM micrograph of the nanoparticles of 1x sample and 10x sample respectively; the white segment illustrates the method used for diameter measurement. (c-d) X-Ray Diffraction (XRD) pattern nanoparticles of 1x sample and 10x sample, respectively; the red stars indicate the diffraction peaks arising from the silicon substrate background. Hydrodynamic size distribution profiles measured via DLS in water (H_2O) and ethanol (EtOH) of 1x sample and 10x sample respectively.*

3.3.1 Proof of functionalization: Dye conjugation assay

To overcome the limitations of the Zeta potential measurements and demonstrate that the amino groups introduced by silanization are indeed chemically accessible and reactive, a conjugation experiment was performed using ATTO 550 NHS-ester. This dye specifically reacts with primary amines to form a stable amide bond, providing an indirect method to confirm the successful surface functionalization.

The conjugation efficiency was monitored by analyzing the absorption spectra of both the supernatants of washing steps and the final nanoparticle suspensions, as shown in Figure

134a. The spectra of the supernatants, denoted as Sur_1x and Sur_10x, display a prominent absorption peak centered at 554 nm, which corresponds to the free unbound ATTO 550 dye removed during the purification steps. Notably, the 10x supernatant shows a lower residual dye concentration compared to the 1x sample, suggesting a different interaction or a more efficient conjugation during the labeling process, possibly indicating the presence of higher amount of amino groups on NPs surface.

To further investigate the outcome of the functionalization, fluorescence microscopy imaging was utilized. As illustrated in Figure 13b and 13c both the 1x and 10x samples exhibited red fluorescence emission, which appears localized on discrete nanoparticle aggregates. This qualitative observation confirms that a portion of the ATTO 550 molecules remains associated with the material after the washing cycles, suggesting that the APTMS effectively provided reactive sites for the dye conjugation. The fluorescence intensity appears comparable between the two batches, indicating that the use of a higher silane concentration did not lead to a macroscopically different degree of functionalization under the tested conditions.

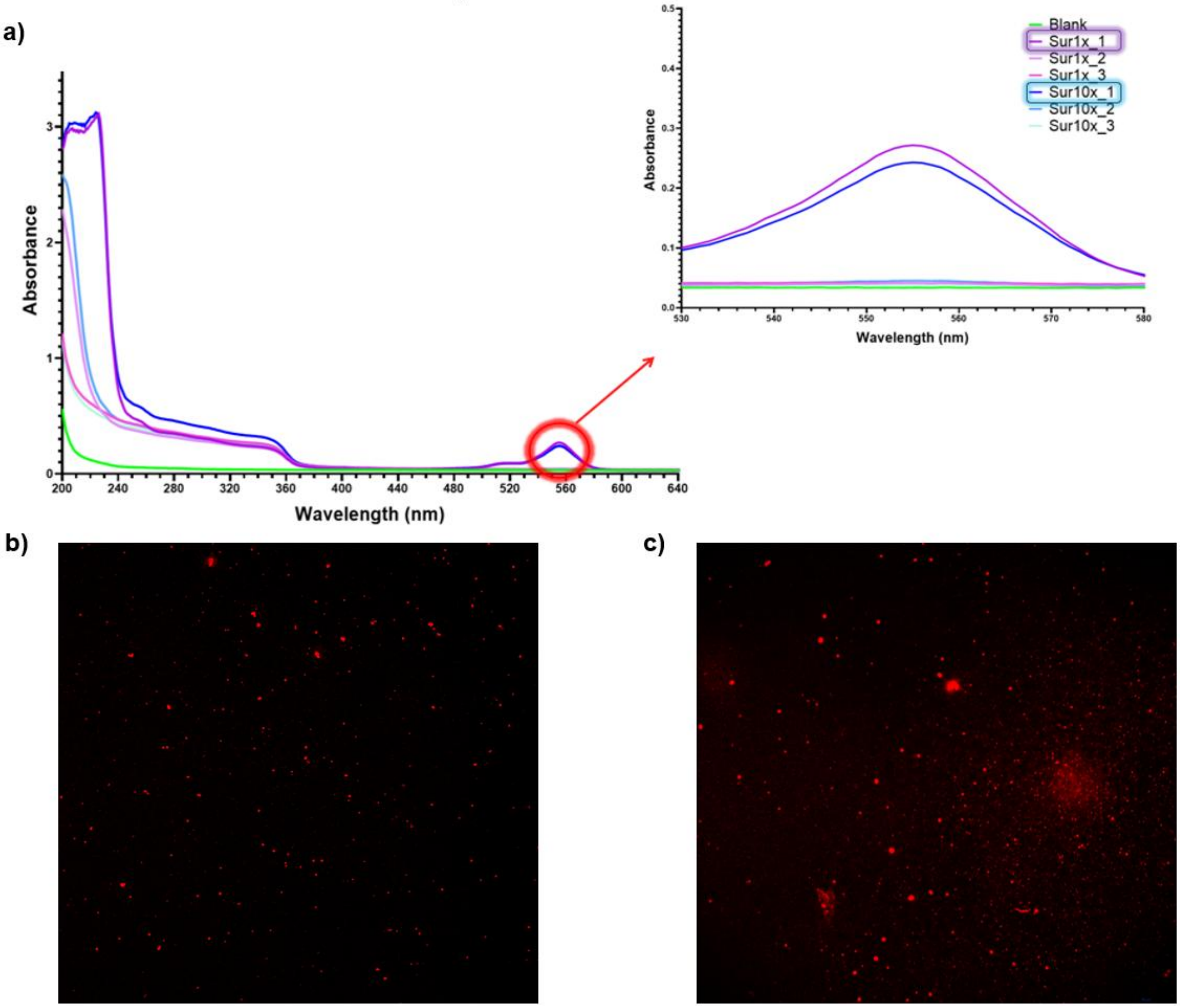

Figure 13 *a)UV-Vis absorption spectra of the washing supernatants containing unreacted dye. The red circle and the magnified inset highlight the specific absorbance peak of ATTO 550 at ~554 nm. (b-c) Fluorescence microscopy images of the 1x (b) and 10x (c) samples. The discrete spots showing red fluorescence emission confirm the successful localization of the dye on the nanoparticle.*

3.4 FeZnO NPs

Building upon the previously described particles, specifically the OlFeZnO NPs, a second batch of nanoparticles was subsequently produced without the use of oleic acid. The primary rationale for this modification was to obtain a pristine and accessible surface, thereby ensuring high reactivity for the subsequent deposition of the silica shell and avoiding any potential interference of capping agent molecules during the subsequent functionalization process.

The synthesized Fe-doped ZnO nanoparticles were analyzed using FESEM to determine the particle morphology, XRD to investigate their crystalline structure and DLS and zeta potential analysis to evaluate the hydrodynamic size and the surface charge. A summary of the data obtained is presented in Figure 14 and Table 6.

The FESEM analysis (Figure 14a) revealed that the synthesis produced nanoparticles with a uniform, quasi-spherical morphology. Analysis of the particle size distribution, as displayed in the histogram in Figure 14b, identified a mean diameter of 8.4 nm (within a broader range of 8–12 nm).

The phase purity and crystallinity were investigated using XRD. The diffraction patterns (Figure 14c) confirmed the crystalline nature of the material, exhibiting the characteristic peaks (100), (002), and (101), associated with the hexagonal wurtzite phase of Zinc Oxide. The broadening of these peaks was consistent with the formation of nanocrystalline domains. Quantitatively, the average crystallite size was calculated using the Debye-Scherrer equation yielding a value of 7.56 nm. It is worth noting that this crystallite size is in excellent agreement with the physical diameter measured by FESEM (8.4 nm). This similarity suggests that the synthesized nanoparticles are likely monocrystalline, meaning each particle consists of a single crystalline domain.

To evaluate the behavior of the nanoparticles in suspension, the hydrodynamic size was analyzed via DLS (Figure 14d). The measurements revealed a size around 140 nm. The size distribution profiles indicated a uniform dispersion in both water and ethanol.

Overall, the absence of oleic capping does not cause relevant changes in the morphology, crystallinity, and colloidal behavior of synthesized NPs.

Table 6 *Physicochemical properties of Fe-doped ZnO nanoparticles (FeZnO NPs), reporting DLS data (Size and PdI in ethanol/water), Zeta Potential, crystallite size (XRD), and primary particle diameter (FESEM).*

Z-Aver_EtOH	PDI_EtOH	Z-Aver_H2O	PDI_H2O	ζ-Pot(mV)	Crystallite size (Scherrer)	FESEM diameter
150.4	0.12	137.7	0.11	29.3	7.56nm	8.4nm

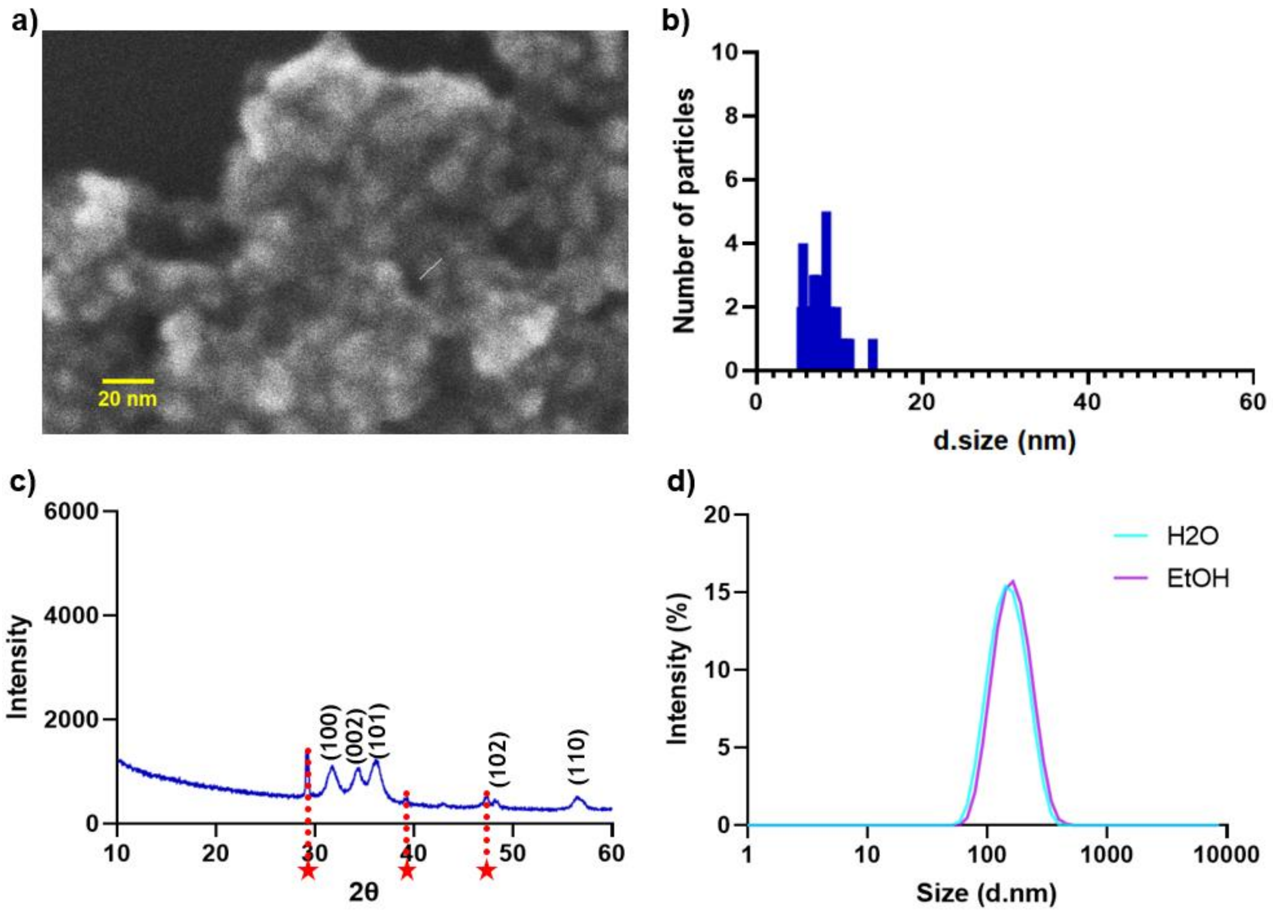

Figure 14 *Physicochemical characterization of Fe-doped ZnO nanoparticles (FeZnO NPs). (a) FESEM micrograph of the nanoparticles; the white segment illustrates the method used for diameter measurement. (b) Histogram representing particle size distribution based on FESEM measurement. (c) X-Ray Diffraction (XRD) pattern; the red stars indicate the diffraction peaks arising from the silicon substrate background. (d) Hydrodynamic size distribution profiles measured via DLS in water (H_2O) and ethanol (EtOH).*

3.5 ZnO quantum dots

Two distinct synthetic strategies were investigated to optimize the production of zinc oxide QDs.

The first approach, designated as Method 1, employs potassium hydroxide (KOH) as the hydrolyzing agent in ethanol, a combination that, while enabling the formation of stable colloids, is characterized by fast reaction kinetics due to the high dissociation constant of the base. This specific pathway has to be carefully controlled, optimizing reaction time and temperature, since the rapid kinetics can lead to secondary precipitation and a consequent increase in the average particle size [70,71].

Conversely, the second approach, identified as Method 2, utilizes sodium hydroxide (NaOH) in methanol. The use of methanol introduces a different solvation interaction for the zinc ions, where the specific solvated ion radius and the viscosity of the medium directly influence the kinetics of nucleation and growth of the crystals [70]. More importantly, in Method 2 the precursor concentrations were lowered, thereby reducing the rate of nucleation and growth processes, which could provide easier regulation of the reaction and better control of the nanocrystals size.

3.5.1 Method 1 (ZnO QDs1)

The synthesis identified as Method 1 was used to produce three distinct formulations, which are undoped QDs (ZnO QDs1), Iron-doped amino-functionalized QDs (FeZnONH2 QDs1), and Gadolinium-doped QDs (GdZnO QDs1). These nanoparticles underwent a comprehensive physicochemical characterization to assess their morphological, structural, and colloidal properties, with the resulting quantitative data summarized in Tables 7, and in figures 15, 16 and 17.

Regarding the morphological evaluation conducted via FESEM to determine the particle size, the image of undoped ZnO QDs1 reveals a uniform, spherical morphology, and a mean primary diameter of 9.5 nm, similar of those obtained for ZnO NPs. However, it is worth mentioning that NPs appeared as small entities aggregated in cluster, while ZnO QDs1 showed better separation and it was possible to identify singular structures, suggesting a higher dispersion of the sample. In contrast, the iron doping and in situ functionalization with amino groups of the FeZnONH2 QDs1 had a detectable impact on the growth kinetics, resulting in the smallest nanoparticles among all batches with a predominant diameter of 5.4 nm. Lastly, the GdZnO QDs1 showed a predominant diameter of 11.7 nm.

The structural properties investigated using XRD further support these observations, as the diffraction patterns confirm the formation of the hexagonal wurtzite phase for all samples. Quantitatively, the average crystallite size was calculated using the Debye-Scherrer equation, yielding values of 9.26 nm for the undoped QDs1, 5.28 nm for the Fe-doped formulation, and 8.98 nm for the Gd-doped system. It is important to highlight the remarkable agreement between these values and the physical diameters measured by FESEM, which unequivocally confirms the high crystallinity and single-domain nature of the quantum dots. In the case of Gd-doped ZnO QDs the presence of secondary impurities was observed and ascribed to secondary oxide phases involving Gd or non-reacted synthesis precursors.

Finally, the colloidal behavior was analyzed via DLS to evaluate the stability of the quantum dots in suspension. In MilliQ water, the ZnO QDs1 exhibit excellent dispersion with a peak centered at approximately 30-40 nm, while the FeZnONH2 QDs1 show an extremely small hydrodynamic diameter of 16.64 nm due to the effective capping provided by the in situ silanization. The GdZnO QDs1 exhibit a mean hydrodynamic diameter centered around 93 nm in the same aqueous medium. Conversely, in ethanol, all formulations display a significant shift to larger dimensions ranging from 200 nm to 410 nm, which indicates a strong tendency to form aggregates in alcoholic medium [74].

Table 7 *Physicochemical properties of ZnO quantum dots (ZnO QDs1), Amino-functionalized Fe-doped ZnO quantum dots (FeZnONH2 QDs1) and Gd-doped ZnO quantum dots (GdZnO QDs1) respectively, first, second and third row,, reporting DLS data (Size and PdI in ethanol/water), Zeta Potential, crystallite size (XRD), and primary particle diameter (FESEM).*

Sample	Z-Aver EtOH	PDI_EtOH	Z-Aver H2O	PDI_H2O	ζ-Pot(mV)	Crystallite size (Scherrer)	FESEM diameter
ZnO QDs1	225.7	0.23	29.2	0.24	43.4	9.26nm	9.5nm
FeZnONH2 QDs1	237.2	0.11	16.64	0.2	35.9	5.28nm	5.4nm

GdZnO QDs1	410.6	0.2	93.07	0.35	34.1	8.98nm	11.5nm

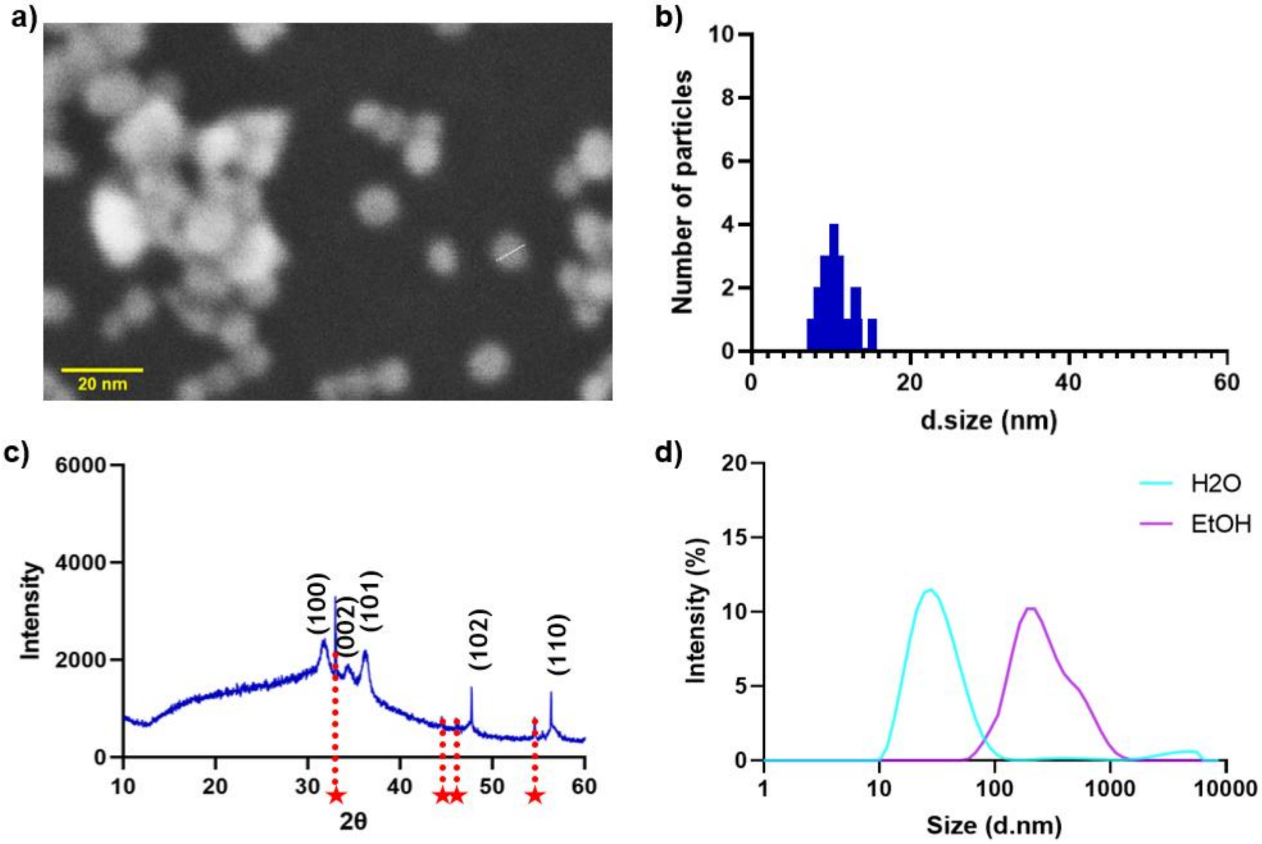

Figure 15 *Physicochemical characterization of ZnO quantum dots (ZnO QDs1). (a) FESEM micrograph of the nanoparticles; the white segment illustrates the method used for diameter measurement. (b) Histogram representing particle size distribution based on FESEM measurement (c) X-Ray Diffraction (XRD) pattern; the red stars indicate the diffraction peaks arising from the silicon substrate background. (d) Hydrodynamic size distribution profiles measured via DLS in water (H2O) and ethanol (EtOH).*

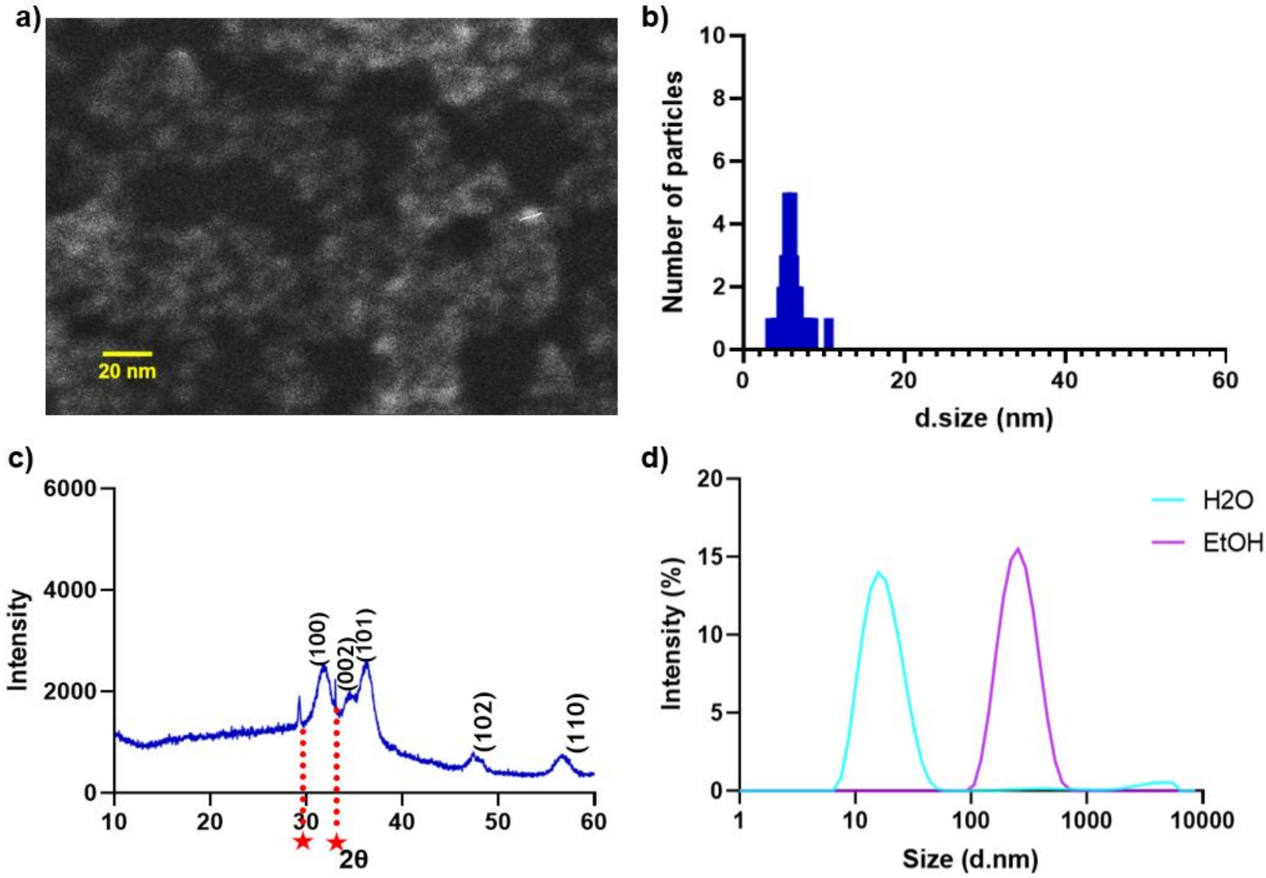

***Figure 16** Physicochemical characterization of Amino-functionalized Fe-doped ZnO quantum dots (FeZnONH2 QDs1). (a) FESEM micrograph of the nanoparticles; the white segment illustrates the method used for diameter measurement. (b) Histogram representing particle size distribution based on FESEM measurement (c) X-Ray Diffraction (XRD) pattern; the red stars indicate the diffraction peaks arising from the silicon substrate background. (d). Hydrodynamic size distribution profiles measured via DLS in water (H2O) and ethanol (EtOH).*

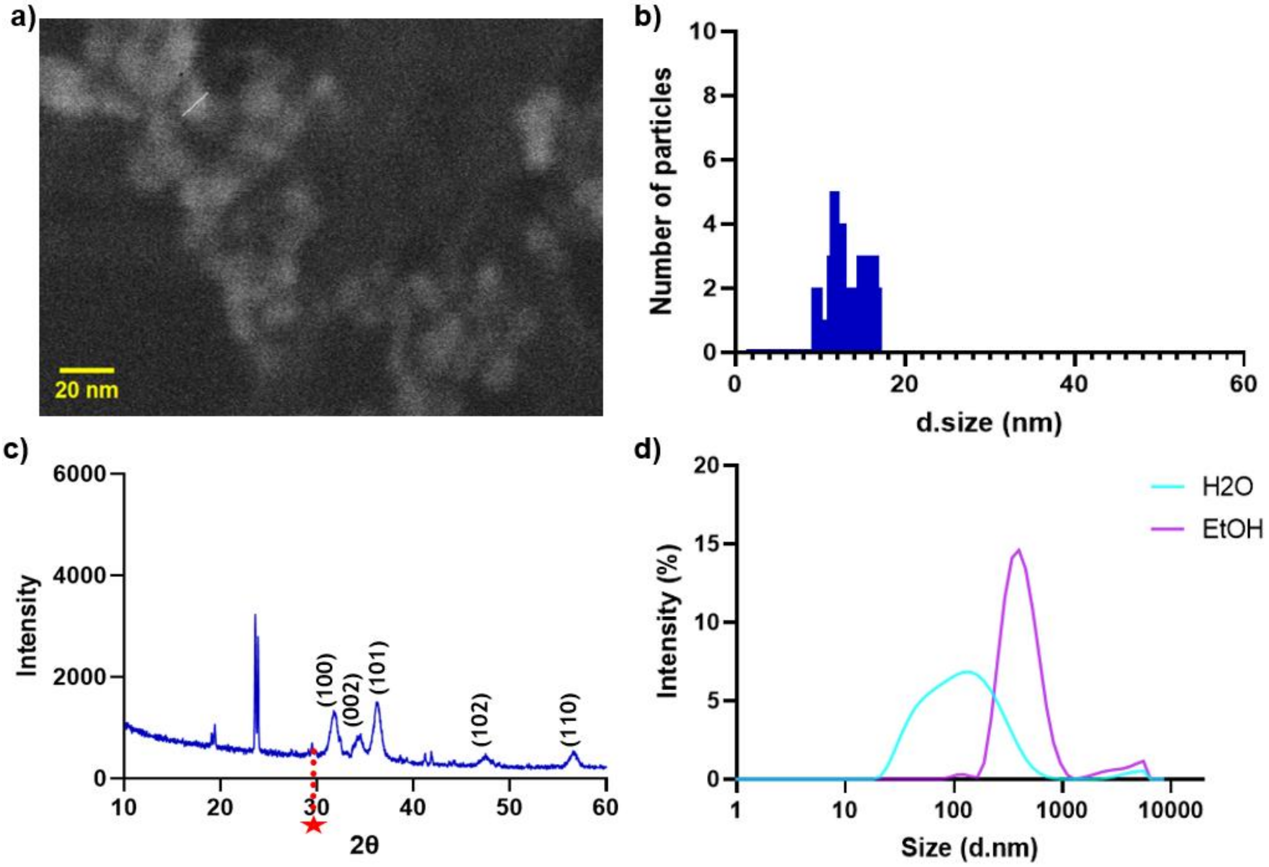

Figure 17 *Physicochemical characterization of Gd-doped ZnO quantum dots (GdZnO QDs1). (a) FESEM micrograph of the nanoparticles; the white segment illustrates the method used for diameter measurement. (b) Histogram representing particle size distribution based on FESEM measurement. (c) X-Ray Diffraction (XRD) pattern; the red stars indicate the diffraction peaks arising from the silicon substrate background. (d) Hydrodynamic size distribution profiles measured via DLS in water (H2O) and ethanol (EtOH).*

Moreover, the green-fluorescence emission under UV excitation was evaluated. As shown in Figure 18, FeZnO QDs exhibit fluorescence under UV illumination, whereas FeZnO NPs show no visible emission. This phenomenon is fundamentally rooted in the quantum confinement effect, which emerges when the semiconductor dimensions are reduced to a scale comparable to or smaller than the exciton Bohr radius [75]. In this regime, the electronic energy levels are no longer continuous as in bulk solids but become discrete and atom-like, directly influencing the optical response of the material. Such a transition allows for size-tunable light emission and enhanced photostability, characteristics that distinguish these quantum dots from ZnO NPs. Consequently, these unique features facilitate the integration of QDs into a variety of advanced fields beyond anti-tumour therapy, including high-resolution bioimaging and the development of sensitive nanosensors [75].

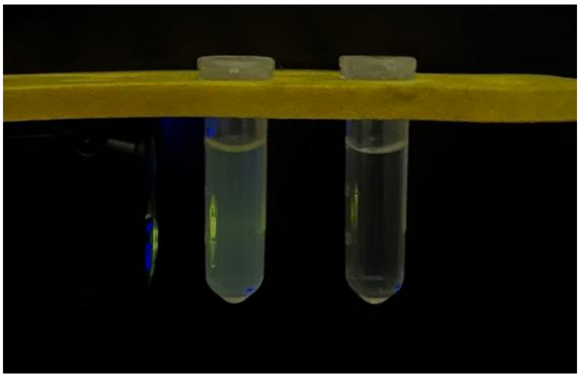

Figure 18 *Optical properties and fluorescence comparison. The image displays ZnO QDs sample in MilliQ water (left) and FeZnO nanoparticles sample in MilliQ water (right) under UV light illumination. The distinct luminescent response of the sample on the left highlights the successful synthesis of quantum dots, which exhibit fluorescence due to quantum confinement effects. Conversely, the FeZnO nanoparticles do not possess this intrinsic property, highlighting the unique optical advantage of the QD-based system for advanced bioimaging and diagnostic applications.*

3.5.2 Method 2 (ZnO QDs2)

The synthesis identified as Method 2 was employed to produce a batch designated as ZnO QDs2. The resulting particles underwent the same characterization used for the previous synthesis, as summarized in Table 8.

The particle morphology was first investigated by FESEM. The micrograph in Figure 19a reveals a poorly defined morphology, which could be attributed to the aggregation of small nanoparticles within a matrix of reaction residues during the drying process for preparing the sample. Due to this irregular geometry and the high degree of interconnection between the structures, a distinct diameter could not be defined, and a reliable statistical analysis of the particle size distribution could not be performed, so the size histogram is not reported for this batch.

To investigate the phase purity and crystalline structure, XRD analysis was subsequently performed. The diffraction pattern, shown in Figure 19b, confirms the formation of the hexagonal wurtzite phase of ZnO, where the main reflection peaks (100), (002), and (101) are clearly identifiable. The average crystallite size was calculated using the Debye-Scherrer equation, yielding a value of 4.57 nm. However, the pattern indicates a lower purity compared to the samples obtained via Method 1. Specifically, a distinct diffraction peak at low angles, highlighted by the red box, can be attributed to unreacted zinc acetate [76], which suggests that the precursor conversion was incomplete or that the washing protocol was insufficient to fully remove residues that crystallized alongside the ZnO nanocrystals. This outcome is hypothesized to stem from specific experimental conditions, particularly the application of a continuous nitrogen flow. While the inert gas was employed to maintain a controlled moisture environment, as the water content significantly influences the hydrolysis and condensation rates, it may have cause excess reduction of reaction kinetics, leading to inefficient precursor conversion.

To evaluate the behavior of the nanoparticles in suspension, the hydrodynamic size and Polydispersity Index (PDI) were analyzed via DLS. As illustrated in Figure 19c, the samples displayed unimodal size distributions in both MilliQ water and ethanol, with a mean hydrodynamic diameter of approximately 60 nm. While these narrow peaks and low PDI values suggest good dispersibility in polar solvents, it is important to specify that DLS data are strictly reliable only for spherical or near-spherical particles. Given the irregular geometry observed in the FESEM images, these hydrodynamic values should be considered as indicative rather than absolute measurements of the particle size. Overall, the results obtained with this approach appear less favorable than those of Method 1, which will therefore be selected for further development.

Table 8 *Physicochemical properties of ZnO quantum dots (ZnO QDs2), reporting DLS data (Size and PdI in ethanol/water), Zeta Potential, crystallite size (XRD).*

Z-Aver_EtOH	PDI_EtOH	Z-Aver_H2O	PDI_H2O	ζ-Pot(mV)	Crystallite size (Scherrer)
75.34	0.17	58.74	0.1	38.1	4.57

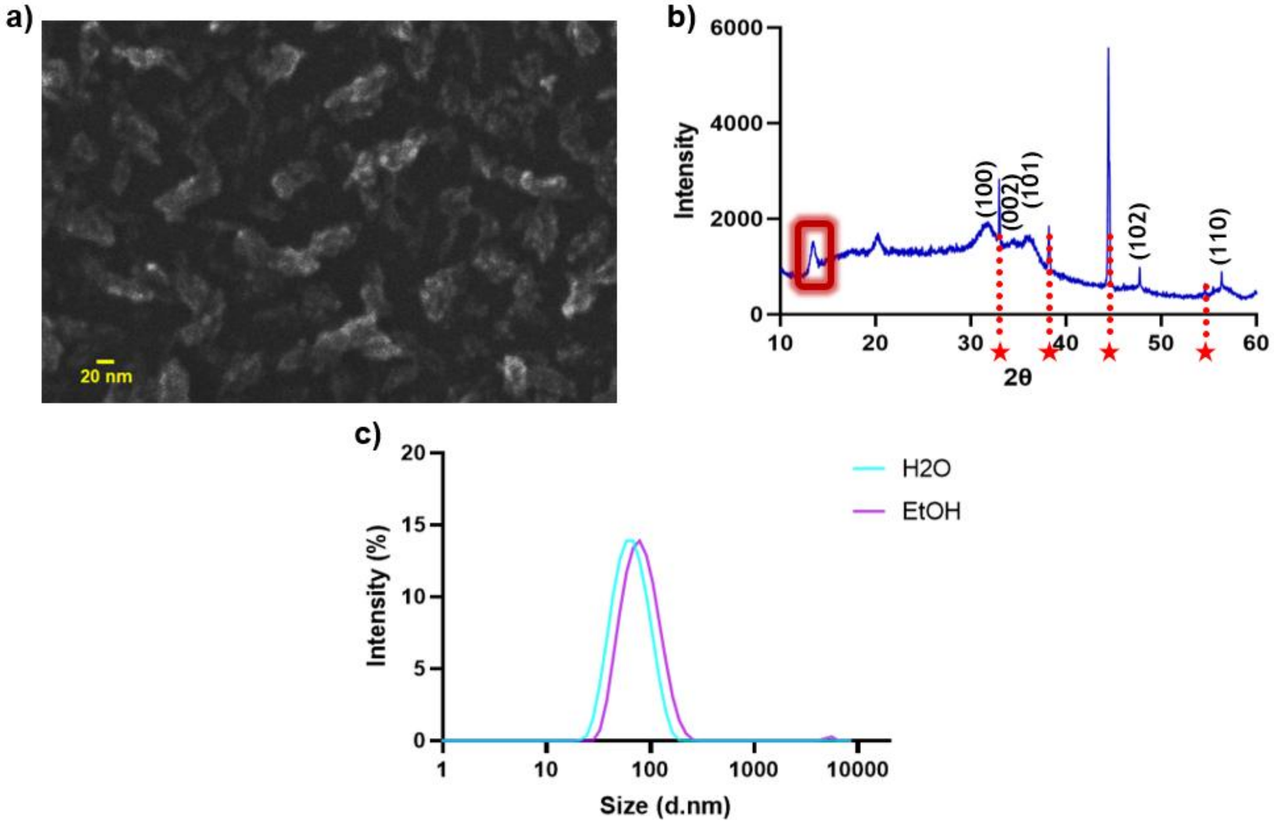

Figure 19 *Physicochemical characterization of ZnO quantum dots (ZnO QDs2). (a) FESEM micrograph of the nanoparticles. (b) X-Ray Diffraction (XRD) pattern; the red stars indicate the diffraction peaks arising from the silicon substrate background and the red rectangle highlight the diffraction peak of unreacted zinc acetate. (c) Hydrodynamic size distribution profiles measured via DLS in water (H2O) and ethanol (EtOH).*

3.6 Mesoporous silica nanoparticles (MSNPs)

Mesoporous silica nanoparticles (MSNPs) were synthesized using CTAB as a structure-directing agent and TEOS as the silica precursor, as described in detail in Section 2.4.1. The aim was to produce a carrier with high surface area and tunable porosity suitable for drug loading.

Following the synthesis, the surfactant template was removed via ionic exchange extraction to obtain an open mesoporous structure.

The resulting particles were characterized to evaluate their colloidal stability and morphology. Quantitative data obtained are presented in Table 9.

To determine the particle size and morphology, FESEM analysis was performed. The micrographs (Figure 20a) reveal that the particles possess a distinct geometry compared to the previously discussed zinc oxide nanostructures. They exhibit a defined, faceted morphology, which is characteristic of CTAB structure-directing agent, which promotes the formation of a hexagonally ordered mesoporous framework [77]. The particle size distribution analysis (Figure 20b) indicates a population ranging from 40 to 100 nm, with a mean diameter centered on 70nm.

To evaluate hydrodynamic behavior, particles were analyzed via DLS in both MilliQ water (H2O) and ethanol (EtOH). The DLS profiles (Figure 20c) show a unimodal distribution with comparable behavior in both solvents, suggesting that the particles are stable in both dispersant. The mean hydrodynamic diameter was recorded at approximately 200 nm.

Comparing these datasets, a significant discrepancy is observed between the hydrodynamic size (~200 nm) and the dry physical size (~70–80 nm). In the case of mesoporous silica, this difference is typically more pronounced than in dense particles due to two synergistic factors:

1. Solvation and Porosity**:** the porous nature of the particles allows solvent molecules to permeate the structure, forming a substantial hydration layer that moves with the particle and increases the frictional drag.[78]

2. Shape Factor**:** the non-spherical, faceted shape of the MSNPs affects the diffusion coefficient measured by DLS (which assumes a perfect sphere), contributing to a larger apparent diameter. [79]

Table 9 *Physicochemical properties of Mesoporous silica nanoparticles (MSNPs), reporting DLS data (Size and PdI in ethanol/water), Zeta Potential, and primary particle diameter (FESEM).*

Z-Aver_EtOH	PDI_EtOH	Z-Aver_H2O	PDI_H2O	ζ-Pot(mV)	FESEM diameter
210.7	0.1	223.6	0.1	-15.3	70nm

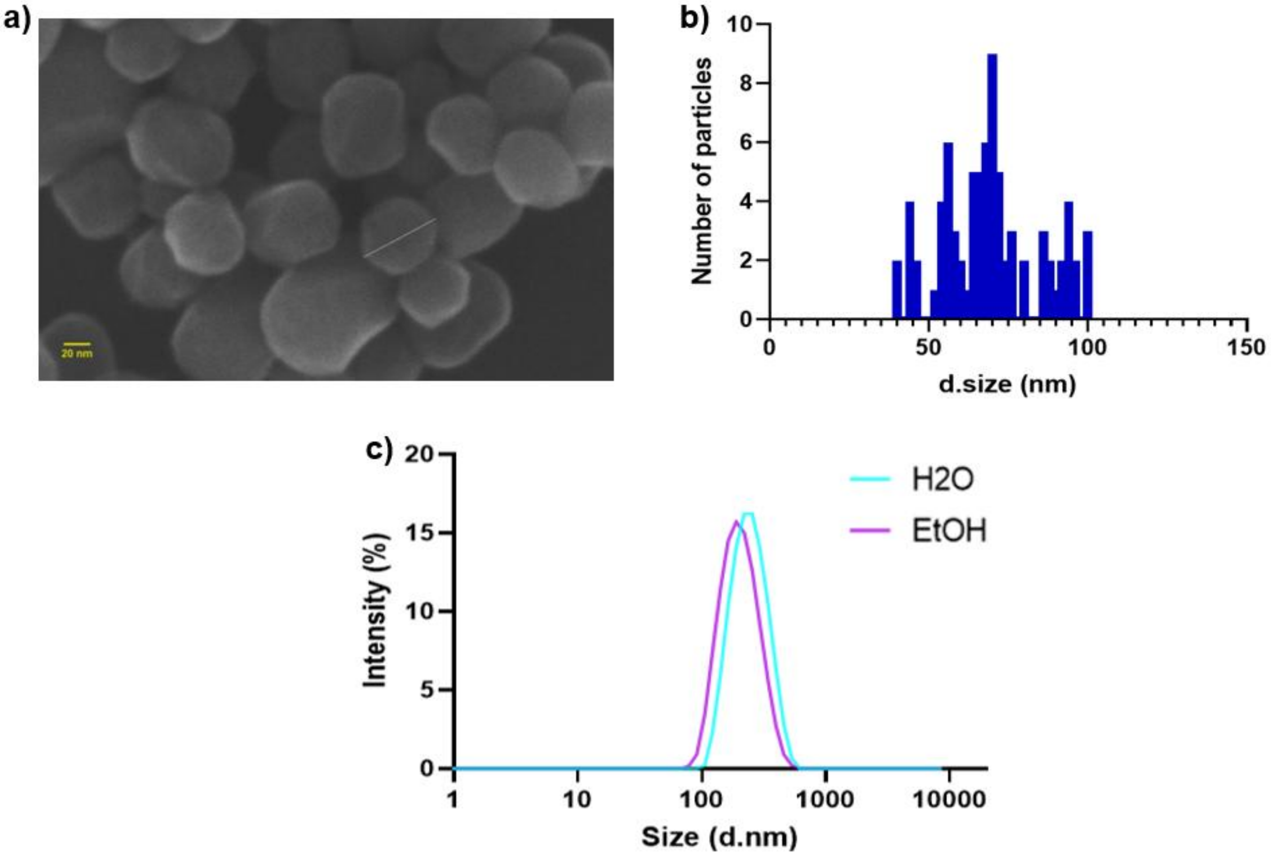

Figure 20 *Physicochemical characterization of Mesoporous silica nanoparticles (MSNPs). (a) FESEM micrograph of the nanoparticles; the white segment illustrates the method used for diameter measurement. (b) Histogram representing particle size distribution based on FESEM measurement. (c) Hydrodynamic size distribution profiles measured via DLS in water (H2O) and ethanol (EtOH).*

3.7 Silica coating of FeZnONPs via ultrasonication (Method US 1)

To obtain a thin silica shell around the FeZnO nanoparticles, a sonochemical approach was employed. As detailed in Table 1 of the Material and Methods, various amount of silica precursor (TEOS), and base (NH_4OH) relative to the ZnO core were tested to optimize the coating process. For batch A, B and C, the synthesis was carried out in a mixture of ethanol and MilliQ water (3:1 v/v ratio). A summary of the experimental outcome is shown in Table 10.

3.7.1 FeZnO@SiO2 US 1 characterization

DLS analysis was conducted in water and ethanol to assess how the solvent medium affects colloidal stability and hydrodynamic size. The results, shown in Figure 21 a and b, reveal substantial differences among the samples. While Batches A and B maintain a monomodal size distribution centered between 100 and 200 nm, Batch C exhibits a marked instability, characterized by the emergence of micron-sized populations exceeding 1000 nm. This behavior, when combined with the Zeta Potential data presented in Figure 21c, allows for a more accurate interpretation of the system's nature.

Although Batch C shows a distinct charge reversal reaching -38 mV, a value typical of deprotonated silica, the massive increase in hydrodynamic diameter suggests that the precursor did not correctly deposit onto the surface of the zinc oxide cores. It is more likely that the high concentration of reagents favored the formation of free silica aggregates or the nucleation of independent silica particles, which led to the creation of voluminous clusters rather than a dispersed core-shell system. Conversely, Batches A and B present strongly positive Zeta Potential values, +29 mV and +23 mV respectively, which are close to that of the naked ZnO core. This indicates that, with the molar ratios employed, the amount of TEOS was insufficient to modify the surface of the nanoparticles to form a uniform thin silica shell.

In conclusion, none of the three tested conditions allowed for the achievement of a stable and correctly coated system, as Batches A and B retained the properties of the uncoated ZnO core, while Batch C is dominated by the formation of silica by-products and aggregates.

Table 10 *Physicochemical properties of Silica coated FeZnO nanoparticles (FeZnO@SiO2 NPs US 1), reporting DLS data (Size and PdI in ethanol/water) and Zeta Potential.*

Sample	Z-Aver_EtOH	PDI_EtOH	Z-Aver_H2O	PDI_H2O	ζ-Pot(mV)
NAKED	152.8	0.13	140.3	0.12	32.9
Batch A	170.3	0.08	220.4	0.25	29.1
Batch B	158.3	0.12	224.6	0.26	23.2
Batch C	*3614*	*1*	*2390*	*0.63*	-39.3

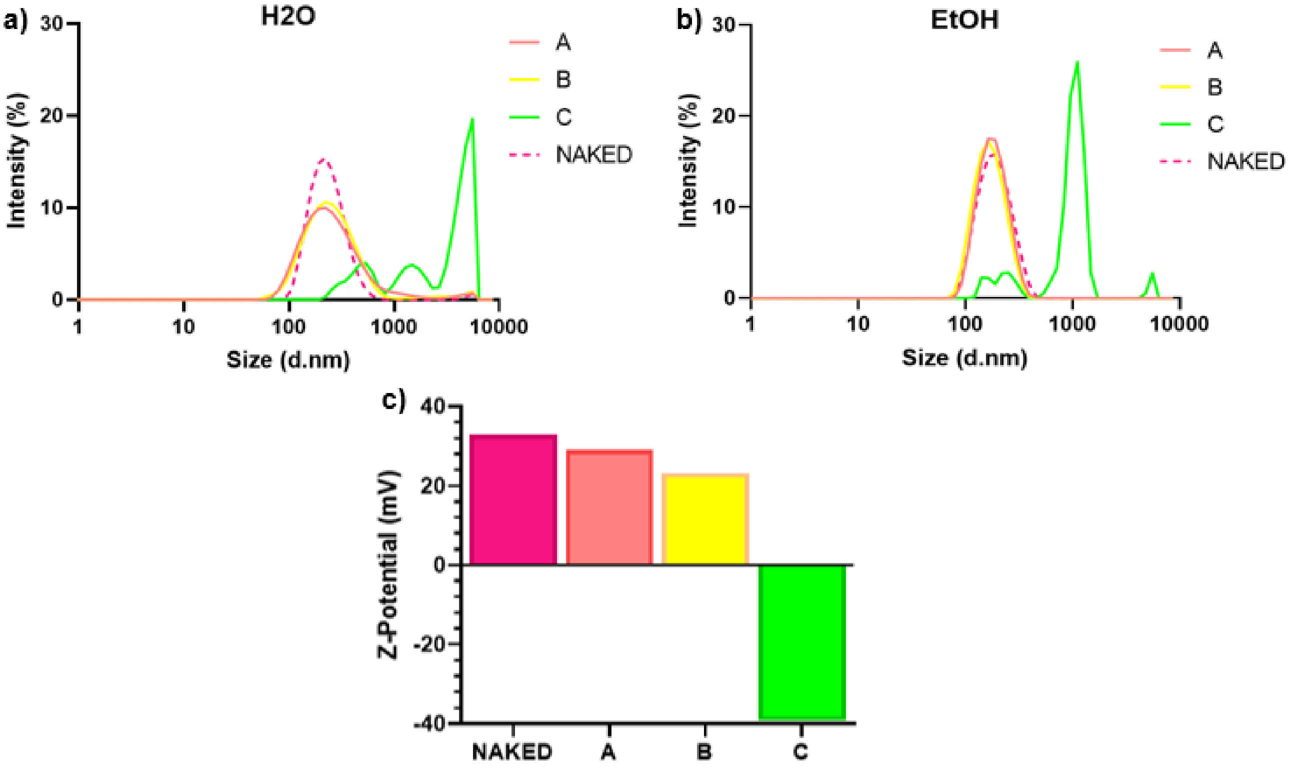

Figure 21 *DLS and Zeta Potential characterization of silica-coated batches (A, B, C) versus uncoated nanoparticles (Naked). (a, b) Hydrodynamic size distributions in H2O and EtOH. (c) Zeta Potential values for each batch compared to the uncoated one.*

3.8 Silica coating of FeZnONPs via ultrasonication (Method US 2)

Following the limitations observed in the water-ethanol mixtures used in Method US 1, a second sonochemical strategy was evaluated. As described in Section 2.5.1, this second set of experiments involved an ethanolic environment to better modulate the hydrolysis and condensation rates of the silica precursor.

These experimental batches are collectively designated as FeZnO@SiO2 US 2 and further identified as Batch D, Batch E, Batch F, and Batch G depending on the specific reaction conditions (different molar ratios among reagent, as reported in Table 1). The resulting nanoparticles were analyzed via DLS and Zeta Potential measurements to analyze changes in surface properties and identify the optimal coating condition. A summary of the experimental data is provided in Table 11.

3.8.1 FeZnO@SiO2 US 2 characterization

To assess colloidal stability, the hydrodynamic size was measured in both water and ethanol. The DLS profiles (Figure 22a, b) demonstrate that changing the reaction medium to absolute ethanol significantly improved the outcome compared to the previous aqueous and ethanol mixture. All four batches (D–G) exhibited unimodal size distributions with no evidence of the massive micron-sized aggregates observed previously. The hydrodynamic diameters remained in the range of 100–200 nm, comparable to the naked core, indicating that the dispersion of ZnO nanoparticles was not adversely affected during the coating process and that the eventually formed silica shell was thin.

To discriminate the degree of silica coverage among the stable batches, Zeta Potential analysis was performed (Figure 22c). This measurement proved critical in identifying the optimal TEOS concentration:

- Batch G and Batch F exhibited Zeta Potential values of +10 mV and -5 mV, respectively. These values - being close to neutrality or still positive - indicate an incomplete or patchy silica shell, insufficient to fully mask the positive surface charge of the FeZnO core.
- Batch E and Batch D displayed a distinct charge reversal, reaching negative values of -20 mV and -35 mV, respectively. This shift suggests the formation of a continuous silica shell, with zeta potential dominated by deprotonated silanol groups.

While both Batch D and Batch E achieved a promising coating, Batch E was selected as the optimal candidate for further characterization and biological testing.

The rationale lies in the efficiency of the synthesis: Batch E represents the formulation that yields a stable, fully coated core-shell system (confirmed by the negative zeta potential and stability in water) using the lowest effective amount of TEOS. While Batch D showed a highly negative potential (-35 mV), suggesting a potentially thicker shell, Batch E provides the best balance between surface coverage and precursor economy, minimizing the risk of forming excessively thick shells or free silica by-products.

Table 11 *Physicochemical properties of Silica coated FeZnO nanoparticles (FeZnO@SiO2 NPs US 2), reporting DLS data (Size and PdI in ethanol/water) and Zeta Potential.*

Sample	Z-Aver_EtOH	PDI_EtOH	Z-Aver_H2O	PDI_H2O	ζ-Pot(mV)
NAKED	152.8	0.13	140.3	0.12	32.9
Batch D	204.6	0.09	189.1	0.11	-35.4
Batch E	170.8	0.06	165.6	0.07	-20.0
Batch F	119.8	0.09	251.2	0.27	-4.73
Batch G	150.4	0.12	153.4	0.15	10.9

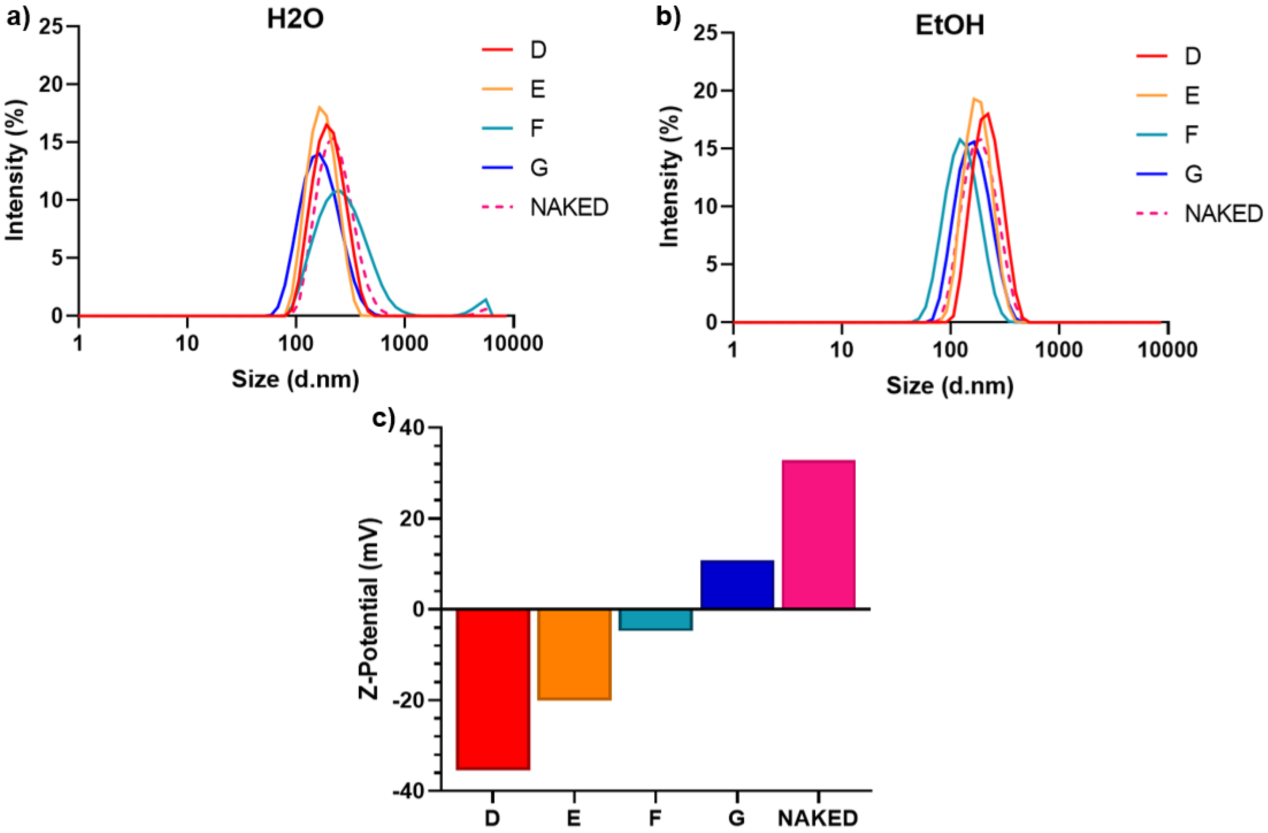

Figure 22 *DLS and Zeta Potential characterization of silica-coated batches (A, B, C) versus uncoated nanoparticles (Naked). (a, b) Hydrodynamic size distributions in H2O and EtOH. (c) Zeta Potential values for each batch compared to the uncoated one.*

The optimized formulation (Batch E) was analyzed by FESEM to assess any changes to size and morphology due to the presence of silica shell. The micrograph in Figure 23 reveals nanoparticles with a uniform, quasi-spherical morphology and a distinct contrast compared to the bare ZnO cores (Figure 23a for the coated particles and b for the uncoated one), suggesting the presence of an amorphous silica envelope. This difference in contrast could arises from the different electron-matter interactions of zinc oxide and silica, as the atomic number of the elements directly influences the secondary electron emission [80]. Analysis of the FESEM size distribution, Figure 23c showing coated sample size distribution and d showing the uncoated one, and Table 12, identified a mean diameter of 13.6 nm.

Moreover, to quantify the zinc content within the obtained core-shell particle and indirectly estimate the amount of silica deposited, UV-Vis spectroscopy was employed (resulting data are reported in Figure 24). This method relies on the optical transparency of the amorphous silica shell across the analyzed spectral range, which implies that the absorbance profile detected in the coated samples is attributed exclusively to the ZnO content of the core. The Beer-Lambert law was used to compare the absorbance of the coated samples against the absorbance of naked FeZnO reference standards, measured by point for each tested concentration. From this comparison, the percentage of the ZnO core with respect to the total weight of the nanoparticle was quantified. As described in details in section 2.7.3 the total yield after coating process was 0.6 mg/mL. Given that the spectroscopic analysis quantified a final ZnO concentration of 0.24 mg/mL, the equivalent silica content was estimate by difference to be 0.36 mg/mL.

These values demonstrate that the silica fraction accounts for 60% of the total mass of the composite system, which confirms the successful coating process and allows for the precise determination of the stoichiometry of the final product. This further characterization validates the formation of a uniform silica shell around ZnO NPs, which could effectively stabilize the nanoparticles for the intended biological applications.

Table 12 *Physicochemical properties of Silica coated FeZnO nanoparticles Batch E (FeZnO@SiO2 NPs US 2 Batch E), reporting DLS data (Size and PdI in ethanol/water), Zeta Potential, and primary particle diameter (FESEM).*

Z-Aver_EtOH	PDI_EtOH	Z-Aver_H2O	PDI_H2O	ζ-Pot(mV)	FESEM diameter
170.8	0.06	165.6	0.07	-20.0	13.6nm

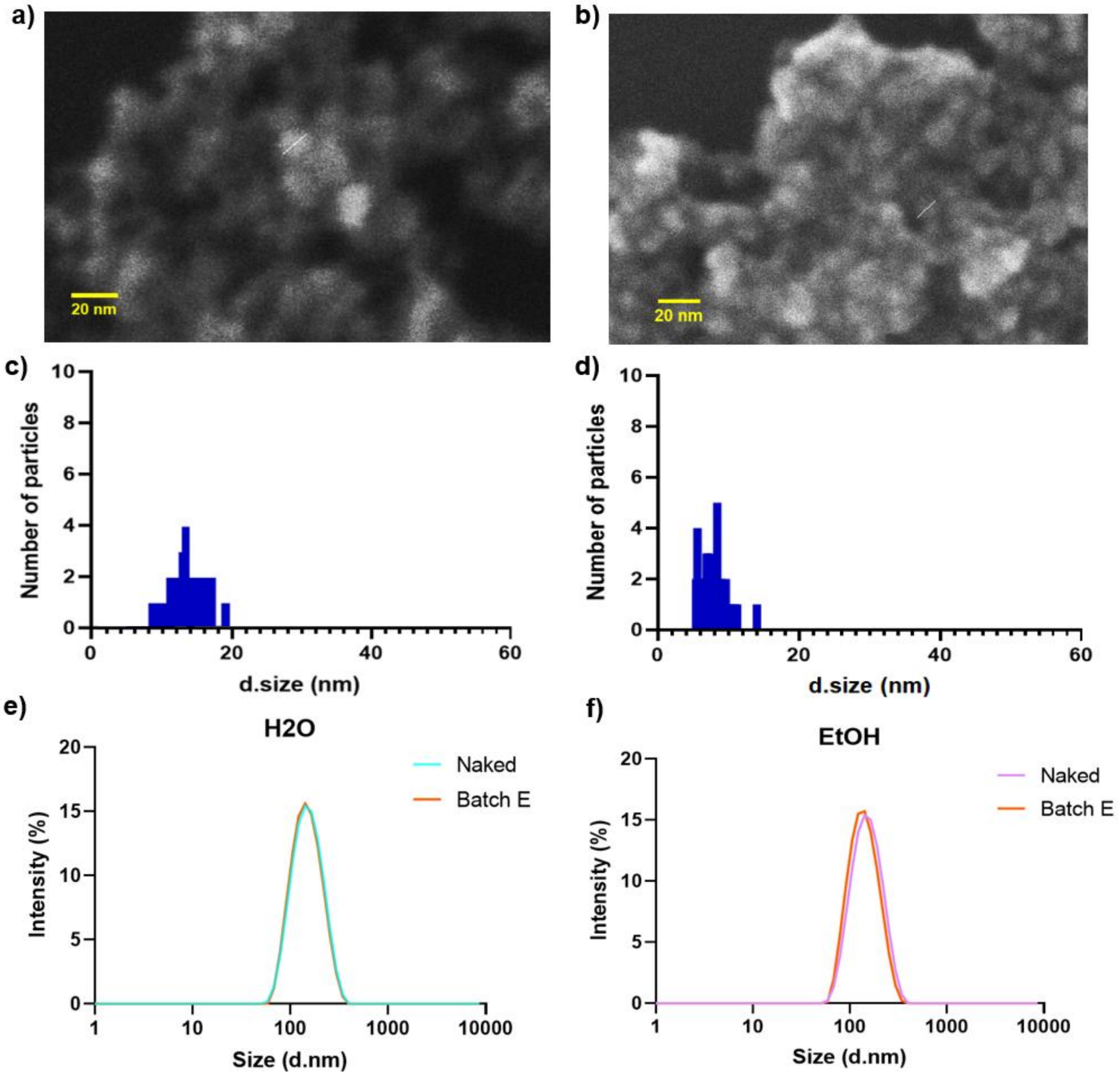

Figure 23 *Physicochemical characterization of the optimized silica-coated nanoparticles (Batch E) compared to the bare ZnO cores. (a, b) FESEM micrograph of the nanoparticles; the white segment illustrates the method used for diameter measurement, silica coated and bare ZnO particles, respectively. (c-d) Histogram representing particles size distribution based on FESEM measurement.. (e-f) Hydrodynamic size distribution profiles measured via DLS in water (H2O) and ethanol (EtOH) compared to the uncoated precursor.*

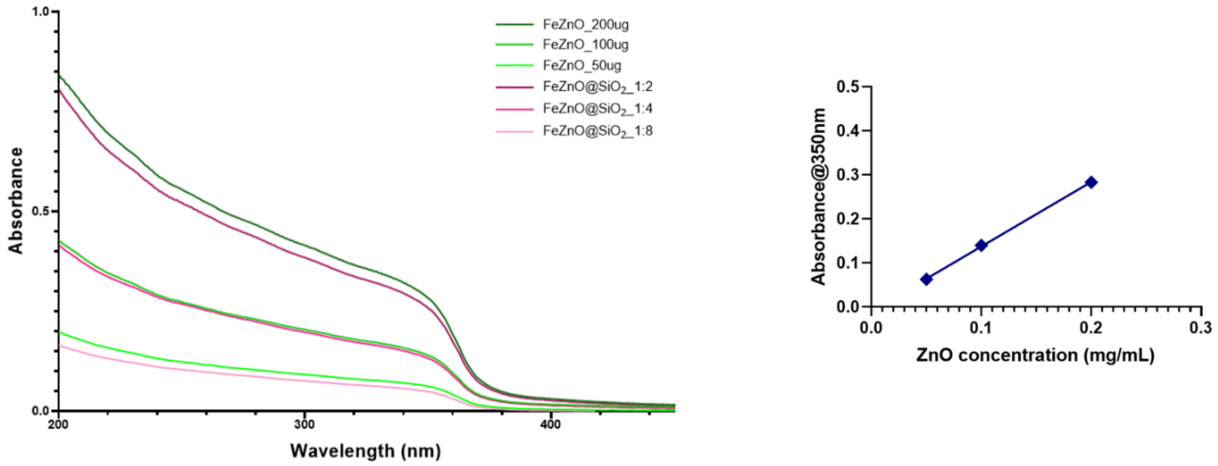

Figure 24 *UV Vis absorbance spectra of FeZnO reference standards and FeZnO@SiO2 samples across the analyzed spectral range, including the linear calibration curve derived at 350 nm. The full spectra illustrate the optical transparency of the*

amorphous silica shell, which preserves the characteristic absorption profile of the ZnO core without interference, and the regression analysis enables the precise interpolation of the zinc oxide concentration in the coated nanoparticles

3.9 Biological assessment: cytotoxicity on A549 cells

To evaluate the biocompatibility of the optimized core-shell nanocarriers (labelled above as FeZnO@SiO2 NPs US 2 Batch E) and verify the protective efficacy of the silica shell, in vitro cytotoxicity assays were performed on human lung adenocarcinoma cells (A549) (Section 2.8.2).

This cell line was selected as a representative model for solid tumors, aligning with the potential antitumor application of the system. The metabolic activity of the cells was quantified using the WST-1 proliferation assay after exposure to varying concentrations (12.5, 25, 50, and 100 μg/mL) of uncoated FeZnO nanoparticles and the optimized silica-coated FeZnO nanoparticles (FeZnO@SiO2, Batch E). To accurately evaluate the screening effect of the silica shell, the dosage of FeZnO@SiO2 was normalized to the ZnO content. Consequently, while the total weight of the FeZnO@SiO2 particles administered was higher due to the additional mass of the silica coating, the net amount of ZnO remained identical to that of the uncoated samples. This approach ensures that any observed reduction in toxicity is a direct result of the coating's protective effect rather than a lower concentration of the active metal oxide.

The cytotoxicity profiles obtained after 24 hours and 48 hours of incubation are presented in Figure 25. The results reveal a clear dose-dependent reduction in cell viability for both samples; however, the silica coating has a beneficial effect at intermediate concentrations. At low concentrations, specifically 12.5 and 25 μg/mL, both formulations showed good biocompatibility. At 24 hours, as shown in Figure 25a, cell viability remained above 75% for both the naked and coated nanoparticles, with no statistically significant difference observed. At these dosages, ZnO nanoparticles do not induce immediate cell death. However, literature suggests that it can trigger a basal oxidative stress, which represents a state of physiological strain. This condition can exhaust the internal defenses of the tumor cell, making it significantly more sensitive to a second external stimulus. By exploiting this sensitized state, the subsequent application of external energy, such as ultrasound in sonodynamic therapy or light in photdynamic therapy, or even the administration of a drug can effectively overcome cellular resilience and achieve the desired therapeutic effect [81]. The rationale for this approach is to maximize the dose of active nanoparticles up to the threshold of cellular toxicity, thereby priming the system to amplify the cytotoxic impact of an eventual secondary treatment.

At the intermediate concentration of 50 μg/mL, this dosage represents the critical tipping point where the protective role of the shell becomes manifest. The uncoated FeZnO induced severe cytotoxicity, causing a dramatic drop in viability to approximately 12% at 24h and less than 5% at 48h. In sharp contrast, the FeZnO@SiO2 nanoparticles preserved cell viability, with values remaining around 75% at 24h and 60% at 48h. This result confirms that the dense silica shell effectively shields the core, probably preventing the rapid dissolution of Zn^{2+} ions.

At the high concentration of 100 µg/mL, a significant decrease in viability below 10% was observed for both formulations. At this dosage, the protective effect of the silica shell is overcome. This may be due to an excessive amount of internalized nanoparticles, indeed, the massive cellular uptake and physical accumulation of nanoparticles may induce mechanical stress or interfere with cytoskeleton dynamics regardless of surface chemistry, leading to irreversible metabolic failure [82,83]. While further mechanistic studies are required to confirm this hypothesis, these results demonstrate that the silica coating effectively attenuates the inherent cytotoxicity of ZnO at lower concentrations.

Extending the exposure time to 48 hours, as illustrated in Figure 25b, exacerbated the toxicity of the uncoated particles, which essentially eradicated the cell population at a dose of 50 µg/mL. Conversely, the silica-coated particles maintained their protective trend, suggesting that the coating stability persists over prolonged incubation periods in the biological medium. Collectively, the metabolic assay demonstrated that coating the FeZnO nanoparticles with a silica shell mitigates their inherent cytotoxicity. Specifically, at 50 µg/mL, the silica shell acts as an effective barrier, transforming a highly toxic agent into a more biocompatible nanoconstruct. Consequently, the silica shell allows for an increase of the administered dose, which is essential for ensuring that a sufficient concentration of FeZnO is present to achieve maximal efficacy once triggered by external stimuli. This improvement is crucial for further experiments, as it validates the success of the optimized wet-chemical protocol in producing safe vectors for potential cancer applications.

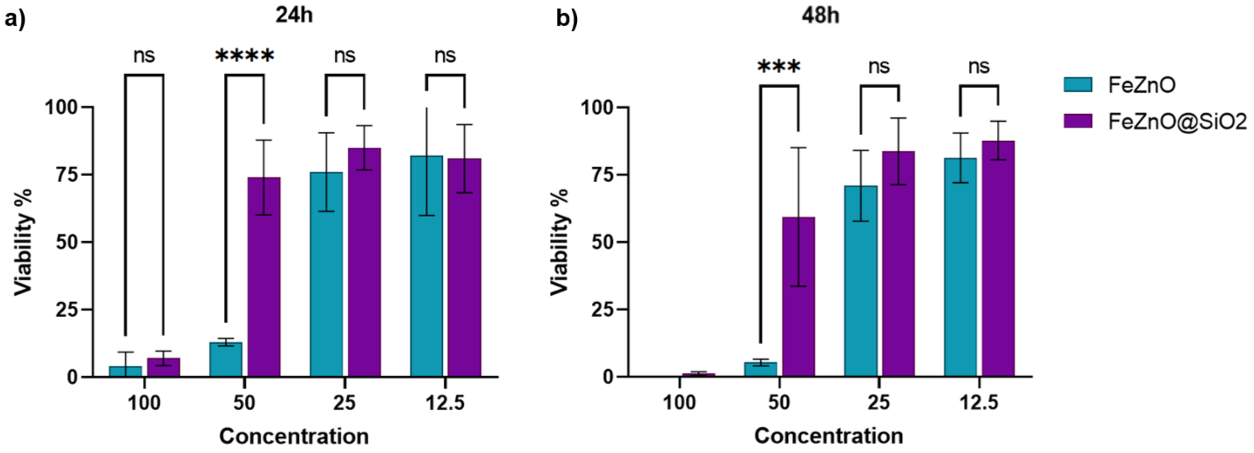

Figure 25 *In vitro cytotoxicity assessment of uncoated FeZnO and silica-coated FeZnO@SiO2 (Batch E) nanoparticles on A549 lung cancer cells using the WST-1 assay. (a) 24-hour incubation: at 50 µg/mL, the silica coating significantly preserves cell viability (~75%) compared to the uncoated counterpart (~12%). (b) 48-hour incubation: the trend is confirmed, with the uncoated nanoparticles causing near-total cell death at 50 µg/mL, while the coated system maintains moderate viability (~60%). Data are presented as mean viability % ± Standard Deviation (n=3 biological replicates).*

3.10 Silica coating of ZnO quantum dots via ultrasonication (Method US 2)

The reaction parameters of the ultrasonic coating method, US2, were applied to the ZnO QDs2 sample with molar ratios shown in Table 1 (batch H and I). After the synthesis, the samples were analyzed via DLS and ELS to investigate their size and the zeta potential. The results are reported in Table 13, while the size distribution curves in water and ethanol are shown in Figure 26. The hydrodynamic diameter size of the nanoparticles of batch H resulted in 234.3 nm in

Milli-Q water and 253.5 nm in ethanol, while for Batch I, it was 71.65 nm in Milli-Q water and 102.4 nm in ethanol. Regarding the surface charge, the Z-potential values for Batch H and I were -42.2 mV and -18.3 mV, respectively. Based on these data and the comparison between each batch and the naked particles, batch I was selected for FESEM morphological characterization, which however revealed an irregular morphology that, as observed for the bare ZnO QDs2 particles, prevented an accurate particle size analysis. Therefore, in contrast to the FeZnO@SiO2 nanoparticles, the QDs could not be maintained as monodispersed entities during the coating process, likely resulting in the formation of aggregates.

Table 13 *Physicochemical properties of Silica coated ZnO quantum dots (ZnO@SiO2 QDs US 2), reporting DLS data (Size and PdI in ethanol/water) and Zeta Potential.*

Sample	Z-Aver_EtOH	PDI_EtOH	Z-Aver_H2O	PDI_H2O	ζ-Pot(mV)
NAKED	75.34	0.17	58.74	0.1	38.1
Batch H	253.5	0.09	234.3	0.07	-42.2
Batch I	102.4	0.11	71.65	0.13	-18.3

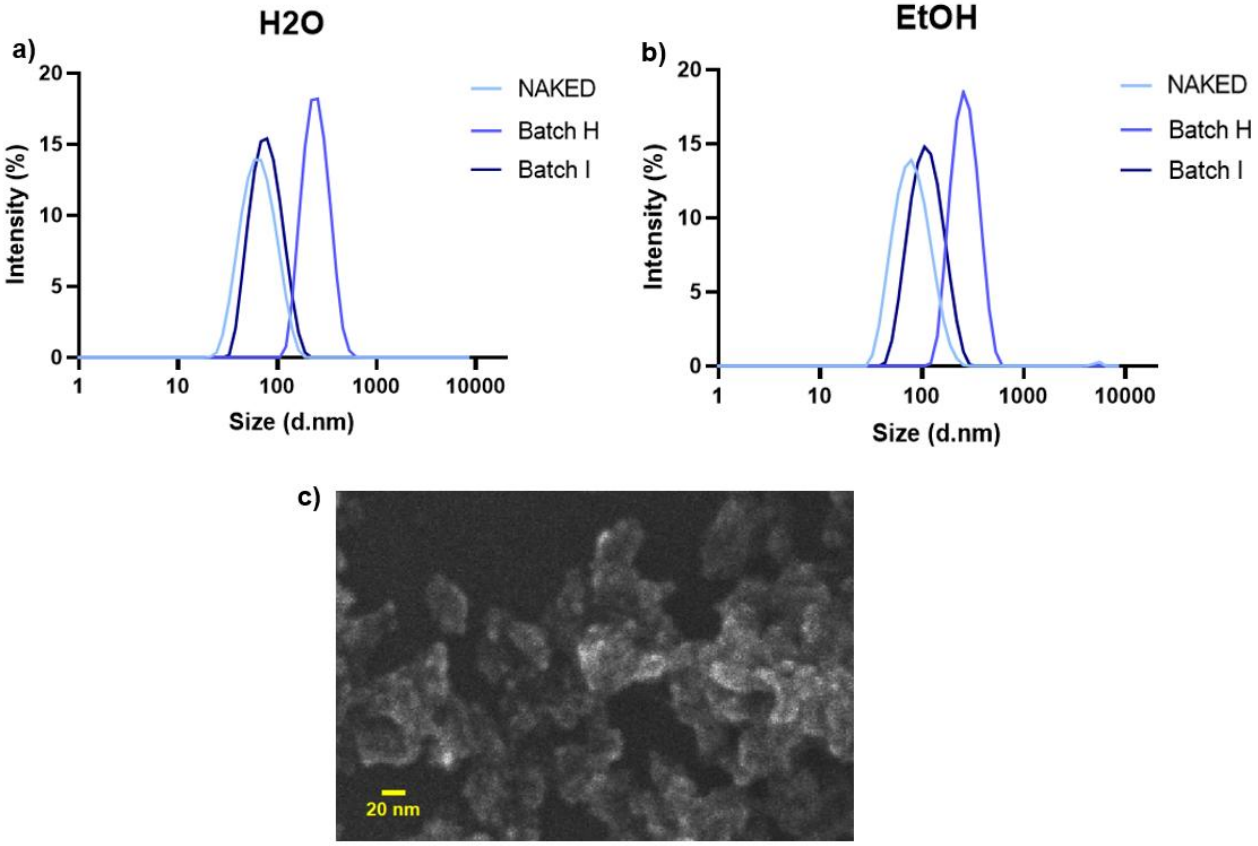

Figure 26 *Physicochemical characterization of silica-coated batches (H, I) versus uncoated nanoparticles (Naked). (a, b) Hydrodynamic size distribution profiles measured via DLS in water (H2O) and ethanol (EtOH) compared to the uncoated precursor. (c) FESEM micrograph of the particles.*

3.11 Post-synthesis silica coating of ZnO quantum dots (Method 1)

Due to the suboptimal results obtained with the ultrasound-assisted coating process for the QDs, alternative methodologies were investigated. As previously demonstrated, ZnO QDs exhibit a high degree of aggregation in ethanol but remain well-dispersed in water. Consequently, a post-synthesis coating procedure performed in water at 100 °C was evaluated to encapsulate the ZnO QDs. The process was repeated by using two different TEOS concentrations, corresponding to molar ratios of 20% and 5% relative to ZnO, to modulate the silica growth and prevent excessive polymerization. These experimental batches are named as ZnO@SiO2 QDs1 20% and 5%.

The resulting nanoparticles were analyzed via DLS to evaluate the effect of the coating process on colloidal stability. A summary of the experimental data is provided in Table 15.

3.11.1 ZnO@SiO2 QDs 5% and 20% characterization

The comparative results between the coated samples and the uncoated reference are displayed in Figure 26. The analysis reveals that this post-synthesis route also induced severe destabilization of the colloidal system, regardless of the precursor concentration.

- 20% formulation: as shown in Figure 27a, the particle size distribution in water shifted entirely from the nanometric range of the naked QDs (~20–30 nm) to the micron range, indicating the formation of massive macro-aggregates. This instability was even more critical in ethanol (Figure 27b): the aggregates formed were so large that they sedimented rapidly during the measurement, making it impossible to record the size distribution. Furthermore, the surface charge analysis for this formulation showed a significant decrease in Zeta potential, reaching values close to neutrality.

- 5% formulation: reducing the precursor amount to 5% did not mitigate the issue. The DLS profiles in both water (Figure 27c) and ethanol (Figure 27d) continue to display multimodal distributions with dominant populations centered in the micron range (1000–5000 nm). In this case, the measured surface charge was 17.8 mV.

These results indicate that the high-temperature aqueous protocol is unsuitable for coating these specific ZnO QDs. The failure is likely attributed to the reaction conditions that promoted aggregation of the QDs. The result is the formation of large silica nanoparticles, which highly likely trapped multiple quantum dots covalently bonded clusters rather than providing a uniform coating on each single QD.

Table 14 *Physicochemical properties of Silica coated ZnO Quantum Dots (ZnO QDs1), reporting DLS data (Size and PdI in ethanol/water) and Zeta Potential.*

Sample	**Z-Aver_EtOH**	**PDI_EtOH**	**Z-Aver_H2O**	**PDI_H2O**	**ζ-Pot(mV)**
NAKED	225.7	0.23	29.2	0.24	43.4
ZnO_TEOS20%	>10000	0.7	2692	0.5	0.81
ZnO_TEOS5%	2746	0.6	602	0.4	17.8

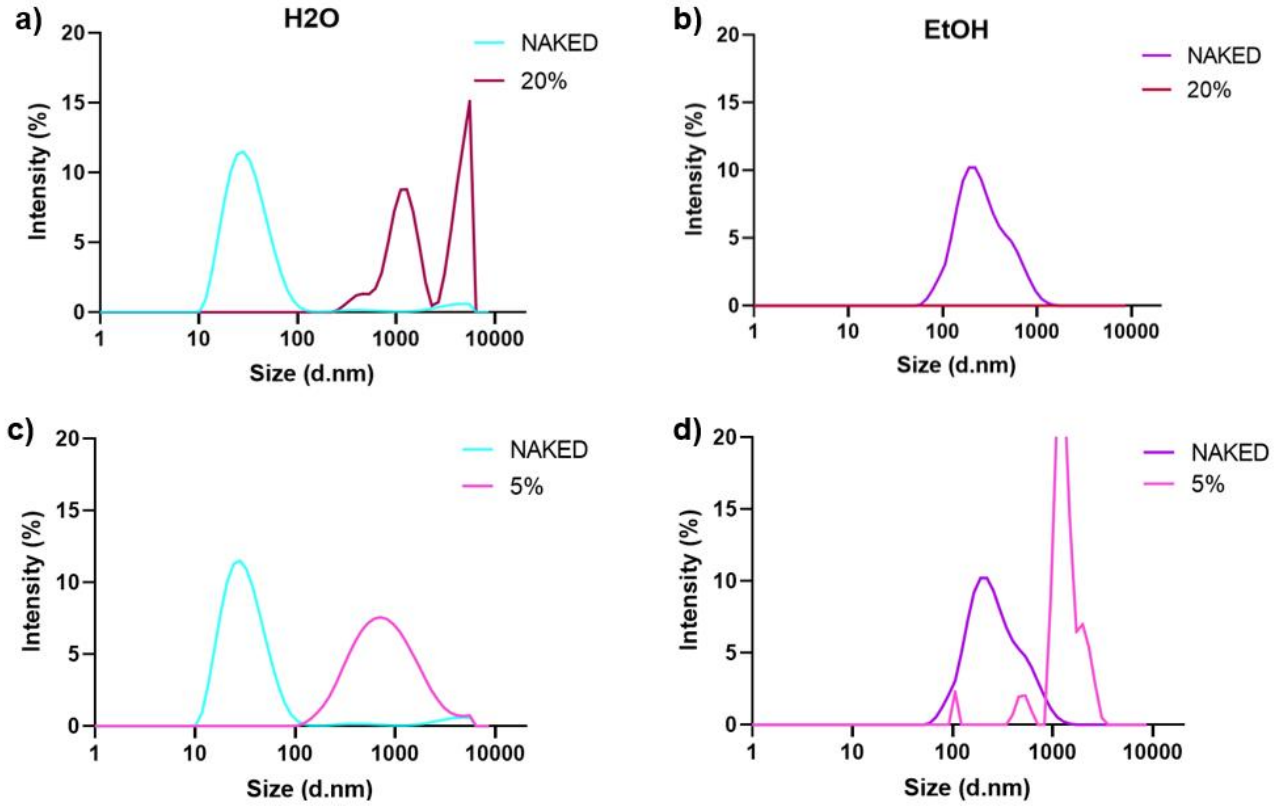

Figure 27 *Physicochemical characterization of silica-coated ZnO Quantum Dots (QDs1) prepared via aqueous route. (a, b) Hydrodynamic size distribution profiles measured via DLS in MilliQ water (H_2O) and ethanol (EtOH) for the sample treated with 20% TEOS compared to the uncoated precursor (Naked). In ethanol (b), the curve for the 20% sample is not visible because the massive aggregates exceeded the instrument's detection range. (c, d) Hydrodynamic size distribution profiles measured via DLS in MilliQ water (H_2O) and ethanol (EtOH) for the sample treated with 5% TEOS compared to the uncoated precursor.*

3.12 Silica coating of ZnO quantum dots (Method 2) during synthesis

Following the failure of the aqueous post-synthesis treatment described in the previous section, the strategy was shifted towards an in-synthesis coating approach.

The presence of water also accelerates the silica growth rate in basic conditions. Specifically, high water concentrations promote the rapid hydrolysis and self-condensation of TEOS in the hydroalcoholic solution, leading to the formation of silica networks that include the QDs aggregates rather than the growth of a uniform silica coating on the independent QD surface [84]. Consequently, the in-synthesis coating procedure, for which the TEOS is introduced directly during the growth phase of ZnO particle, was performed modifying the ZnO QDs2 protocol, which offers a drier reaction environment compared to the one of QDs1.

Specifically, while the synthesis of QDs1 involves the use of 952 µL of water, the QDs2 protocol requires only 318 µL, which is approximately one-third of the volume. It was hypothesized that this reduction in water content would limit the hydrolysis rate of the precursor [84], providing a more controlled environment for the simultaneous nucleation of the core and condensation of the silica shell. This batch is designated as ZnO@SiO2 QDs2. A summary of the experimental data is provided in Table 15, where the datasets for the uncoated sample, referred to as Naked, and the coated sample at 30% are reported.

3.12.1 ZnO@SiO2 QDs2 characterization

To implement this strategy, TEOS was added dropwise to the QDs2 reaction mixture at a molar ratio of 30% relative to the zinc acetate dihydrate precursor, aiming to perform the silane hydrolysis during the zinc oxide nanoparticle growth.

The samples were analyzed via DLS in both ethanol (EtOH) and MilliQ water (H_2O). The comparative results between the coated sample and the uncoated reference are displayed in Figure 28.

The analysis reveals that this route still induced severe destabilization of the colloidal system. In ethanol, the particle size distribution of coated samples shifted significantly compared to the unimodal profile of the naked QDs, which is approximately 50 nm. The sample treated with 30% TEOS exhibits a broad distribution centered around 500 nm with a secondary peak extending into the micron range. This behavior was further exacerbated in aqueous media, where the 30% sample displayed a multimodal distribution with dominant populations shifted entirely to the micron range, precisely between 1000 and 6000 nm, while the naked QDs maintained a stable population around 50–60 nm. The consistency of these results across different solvents confirms the formation of massive aggregates regardless of the medium. Concerning the Zeta potential of the 30% sample, it was measured at 24.2 mV, indicating a slight decrease in surface charge compared to the reference naked sample.

These results indicate that simply using a one-pot approach does not provide advantages in the controlled silica shell growth on these ZnO QDs. Based on the final particle size measured with the DLS, it can be hypothesized that the failure is likely attributed to the hydrolysis of TEOS in the reaction medium that may have occurred simultaneously with the final stages of zinc oxide growth [84]. However, instead of condensing uniformly onto fully formed nuclei, the silicate species might have bond together the ZnO QDs leading to the formation of large covalently bonded aggregates. The slight decrement observed in the ζ-potential, reaching 24.2 mV, further supports the hypothesis that silica was formed. However, this silica growth could not achieve the desired colloidal dispersion of the nanoconstructs.

Table 15 *Physicochemical properties of Silica coated ZnO Quantum Dots (ZnO QDs2), reporting DLS data (Size and PdI in ethanol/water) and Zeta Potential.*

Sample	Z-Aver_EtOH	PDI_EtOH	Z-Aver_H2O	PDI_H2O	ζ-Pot(mV)
NAKED	75.34	0.17	58.74	0.1	38.1
30%	268.4	0.15	1325	0.6	24.2

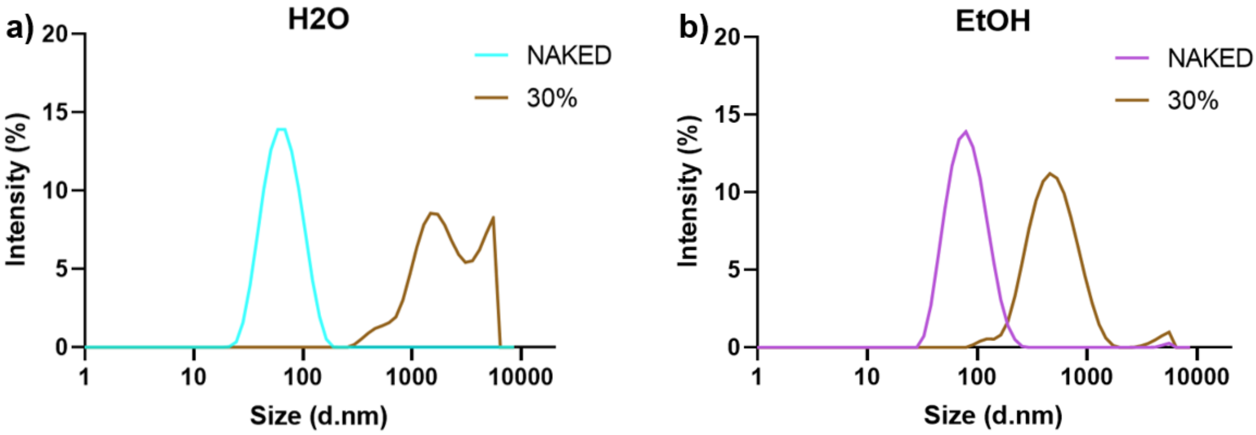

Figure 28 *Physicochemical characterization of silica-coated ZnO Quantum Dots (QDs2). (a, b) Hydrodynamic size distribution profiles measured via DLS in MilliQ water (H_2O) and ethanol (EtOH) for the sample treated with 30% TEOS compared to the uncoated particles (Naked).*

3.13 Evaluation of microfluidic lipid coating of Fe-doped ZnO quantum dots

In parallel with the investigation of inorganic coatings, such as the silica shell, an alternative supramolecular approach was explored: the encapsulation of quantum dots within a lipid bilayer. While silica provides a robust inorganic framework, the lipidic coating offers a biomimetic and versatile interface, relying on physical self-assembly rather than covalent modification. This method aims to provide a biocompatible barrier while avoiding the specific conditions required for wet chemical silica synthesis, which can sometimes interfere with the integrity of ZnO surface [85].

The advantages of utilizing a lipidic coating are manifold, but, most importantly, as organic molecules naturally present in biological systems, lipids offer superior biocompatibility. However, the encapsulation process remains challenging, as it requires high initial dispersion of the bare nanoparticles and solvent conditions that favor the selective self-assembly of the lipidic bilayer onto the nanoparticle surface. Nevertheless, the nanometric dimensions of the QDs, coupled with their extreme sensitivity to the dispersion medium, necessitate highly controlled reaction parameters that are often unattainable through manual synthesis. The formation of a lipidic bilayer typically relies on the solvent exchange method, where a rapid increase in the aqueous fraction within an organic lipid solution (usually ethanol) triggers the self-assembly of amphiphilic molecules into micelles or bilayers. The ZnO surface can serve as a template for this process, facilitating the formation of a supported lipid bilayer.

To ensure maximum reproducibility, a microfluidic-assisted approach was employed in this case. The microfluidic regime, unlike conventional turbulent mixing, is typically laminar and diffusion-limited [86], not providing the correct mixing conditions for the aqueous and the organic phase. To overcome such limitations, the employed chip features a specific herringbone design that induces chaotic advection, a process characterized by the generation of transverse flows that stretch and fold the fluid streams [86]. This mechanism reduces the diffusion distance exponentially, enabling rapid mixing of the organic and aqueous phases on a millisecond timescale [85,86]. Such rapid solvent exchange triggers a controlled nanoprecipitation process, frequently referred to as limit size synthesis, where the lipid assembly is driven by thermodynamics rather than mixing kinetics [86]. This technology are supposed to form uniform and densely packed lipid shells around the QDs before aggregation can occur, providing a highly reproducible method for the synthesis of hybrid nanostructures [85].

The process was performed on amino-functionalized Fe-doped QDs, referred to as FeZnONH2 QDs1. The presence of surface amino groups provides a positive charge density, as confirmed by a Zeta potential of +35.9 mV, (Figure 29) and offers hydrogen-bonding sites that interact effectively with the polar headgroups of the lipids, acting as a molecular anchor to stabilize the forming bilayer [39]. In MilliQ water, these uncoated particles exhibited a hydrodynamic diameter of approximately 19.8 nm with a PDI of 0.3, indicating a substantially monodisperse suspension. However, as shown in first columns of the heat maps in Figure 30, the introduction of saline media and biological buffers, including PBS and RPMI, leads to massive aggregation, with sizes exceeding 2400 nm and 3300 nm, respectively. The aim of the lipidic coating is to stabilize the QDs in biologically relevant media, to allow an actual administration to biological entities. To address this QDs limitation, three distinct lipid formulations were designed with different charge properties. While structural and PEGylated lipid ratios remained unvaried, the head groups of the most abundant lipid components were adjusted to include anionic (3C-), zwitterionic (2CN), or cationic (3C+) functionalities, with the goal of creating a more robust interface between the QDs surface and the lipids exploiting the coulombic interactions.

The results of the coating processes performed with the three formulations are summarized in the heatmaps in Figure 30. As can be seen, all the formulations presented high Z-average values that reveal critical nanoconstructs instability. Regarding the charged formulations, specifically 3C+ and 3C-, the high ionic strength of the biological buffers induced immediate destabilization. These samples formed aggregates in the micron-size range when exposed to saline media, reaching sizes greater than 3000 nm in PBS, which confirms that purely electrostatic stabilization is ineffective in physiological environments. In contrast, the zwitterionic formulation (2CN) consistently showed values that were identified as measurement artifacts. The instrument recorded a Derived Count Rate below 100 kcps, a value significantly lower than the thousands of kcps observed for stable samples. This drastic drop in scattering intensity, compared to the naked particles, suggests that the QDs underwent rapid aggregation and subsequent sedimentation, leaving insufficient material in the detection volume to generate a valid correlation function [87]. The underlying causes for this behavior were clarified by the Zeta potential measurements.

The naked FeZnONH2 QDs1 exhibited a strong positive Zeta-potential of +35.9 mV, attributed to the surface amino groups. Upon coating, the 3C+ formulation maintained a high positive charge of +35.25 mV, while the zwitterionic 2CN reached an intermediate value of +9.71 mV. Most notably, the 3C- formulation led to a complete neutralization of the surface, shifting the value to neutral -0.06 mV, indicating that the anionic lipids compensated the positive charge of the amino groups rather than providing a stable negative shell.

This experimental evidence confirms that a stable lipid coating was not achieved under the tested conditions, as the system was unable to prevent the sedimentation of the ZnO QDs in physiological media. It is highly probable that the inherent instability of the QDs in media other than double-distilled water triggers rapid aggregation. This phenomenon likely occurs prior to the initiation of any chemical or physical modification, effectively precluding the formation of stable nanoconstructs.

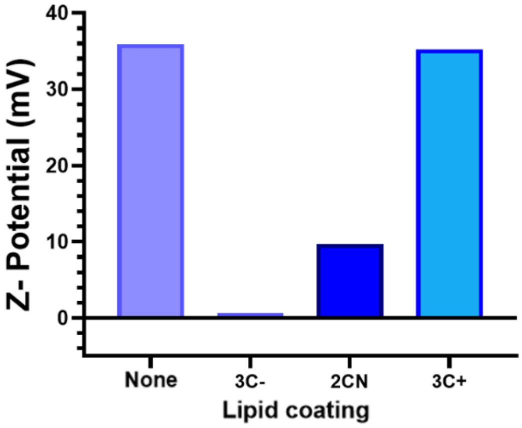

Figure 29 *Zeta potential measurements of uncoated (None) and lipid-coated quantum dots (3C-, 2CN, 3C+). The graph illustrates the surface charge transitions from the naked nanoparticles, characterized by a strong positive charge due to surface amino groups, to the different lipidic formulations.*

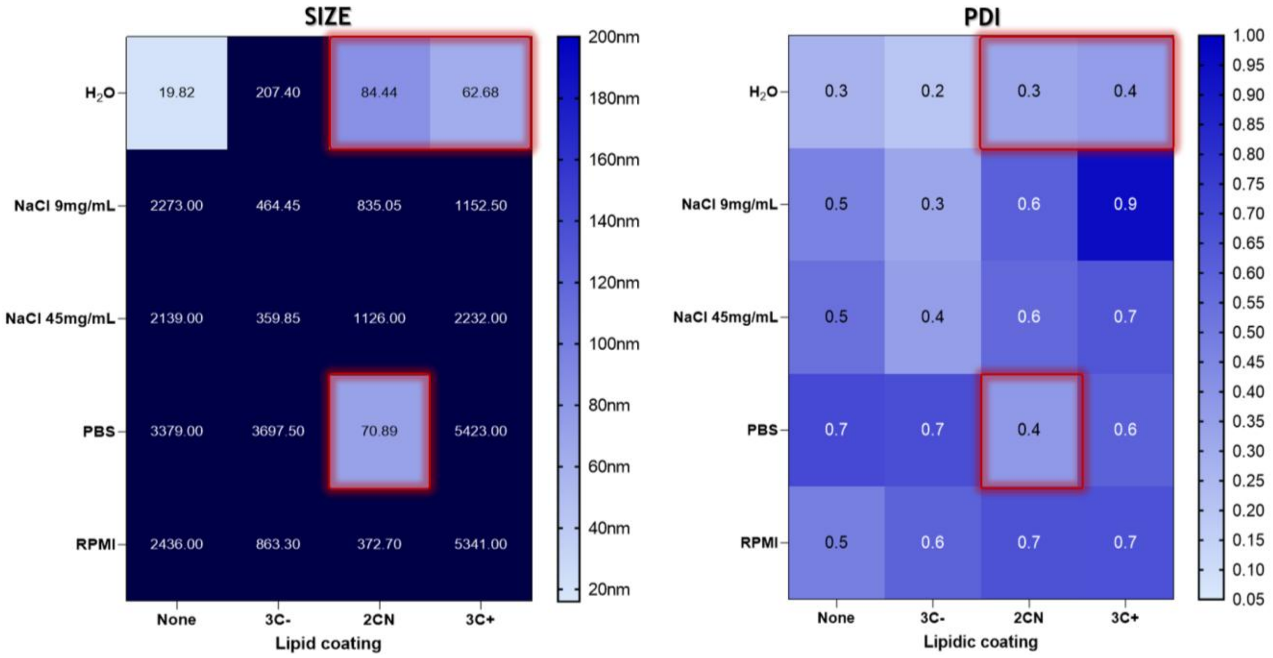

SIZE	None	3C-	2CN	3C+
H_2O	19.82	207.40	84.44	62.68
NaCl 9mg/mL	2273.00	464.45	835.05	1152.50
NaCl 45mg/mL	2139.00	359.85	1126.00	2232.00
PBS	3379.00	3697.50	70.89	5423.00
RPMI	2436.00	863.30	372.70	5341.00

PDI	None	3C-	2CN	3C+
H_2O	0.3	0.2	0.3	0.4
NaCl 9mg/mL	0.5	0.3	0.6	0.9
NaCl 45mg/mL	0.5	0.4	0.6	0.7
PBS	0.7	0.7	0.4	0.6
RPMI	0.5	0.6	0.7	0.7

Figure 30 *Heatmap summary of the colloidal stability for uncoated (None) and lipid-coated quantum dots (3C-, 2CN, 3C+) across different dispersal media. The left panel represents the Hydrodynamic Size (Z-Average), while the right panel displays the Polydispersity Index (PDI). The color gradient indicates the magnitude of the values, with darker blue corresponding to larger aggregates or higher polydispersity. The specific data points highlighted by the red boxes (particularly for the 2CN formulation in PBS and H2O) should be interpreted as measurement artifacts. In these instances, the instrument recorded a Derived count rate <100 kcps. This low scattering intensity indicates that the samples underwent rapid aggregation and sedimentation, leaving insufficient particles in the detection volume.*

4 Conclusion

This Master Thesis explored the design, synthesis, and characterization of iron-doped zinc oxide nanosystems in two distinct size regimes, i.e. nanoparticles and quantum dots, and different strategies for the development of protective shell to optimize their performance for potential antitumor applications. The research addressed the critical challenge of stabilizing ZnO-based materials in biological environments, where their inherent tendency to dissolve and release zinc ions often leads to poor control over the nanosystem, potentially causing unwanted toxicity in healthy tissues.

The experimental work successfully achieved the synthesis of Fe-ZnO nanoparticles and quantum dots through wet chemical routes. The structural and morphological properties were validated via FESEM imaging and XRD analysis, which confirmed the production of crystalline nanoparticles with controlled dimensions. Furthermore, DLS and zeta potential measurements were performed to assess the colloidal stability and surface charge of the synthesized particles. A massive portion of the study was dedicated to investigating silica-based structures as coating strategy, focusing on both dense silica shells and the development of mesoporous silica nanoparticles. In particular, the use of an ultrasound-assisted protocol with optimized reagent ratio and reaction medium (Method US 2, batch E) allowed for the achievement of a stable and uniform dense silica coating on Fe-ZnO NPs which demonstrated marked protective effect in biological assays. The results of in vitro cytotoxicity tests on A549 cells confirmed that the silica shell attenuates the intrinsic toxicity of the Fe-ZnO core at the critical concentration of 50 µg/mL, preserving cell viability compared to the uncoated counterparts.

The successful synthesis of mesoporous nanoparticles represents a promising result, as they could be employed in future studies to encapsulate the ZnO core, aiming to limit the uncontrolled release of zinc ions while providing a versatile platform for drug delivery in different nanomedical application.

Regarding ZnO quantum dots, stabilization attempts with silica coating, performed both in situ and post-synthesis, faced significant challenges related to the tendency of the ultra-small particles to aggregate in the basic environments required for the silica condensation. As an alternative to inorganic silica shell, the study explored the development of lipid shells of positive, negative and neutral lipid formulations using microfluidic technology. However, the experimental results revealed that the lipid coating was not sufficient to ensure the stability of the quantum dots, which exhibited rapid aggregation and sedimentation in biological buffers regardless of the formulation used. These findings, supported by DLS and zeta potential measurements, highlight the complexity of protecting such small-scale structures in high ionic strength solvents and suggest that the current lipid coating procedure requires further optimization to provide the colloidal stability of the system.

The comparative analysis of the different strategies provided valuable insights into the limitations and potential of core-shell ZnO architectures. The data indicated that while dense silica coatings offer a viable route for the efficient shielding of nanoparticles, the challenges encountered with quantum dots emphasize the need for stabilization methods with milder reaction conditions. Additionally, the iron-doped core opens interesting perspectives for further investigations into its piezoelectric, photo, and sono-catalytic properties, which could allow for the study of how external stimuli might activate the nanosystem in a controlled manner for combined therapy applications.

In conclusion, this thesis has investigated the engineering of Fe-ZnO systems, identifying the key parameters that govern their synthesis and stability. Although the stabilization of quantum dots remains a challenge to be overcome, the successful development of silica-coated Fe-ZnO nanoparticles represent significant steps toward creating more stable nanoplatforms, paving the way for future investigations into their interaction within complex biological systems.

5 Bibliography

1. Bulbake, U.; Doppalapudi, S.; Kommineni, N.; Khan, W. Liposomal Formulations in Clinical Use: An Updated Review. *Pharmaceutics* **2017**, *9*, 12.
2. Wang, R.; Billone, P.S.; Mullett, W.M. Nanomedicine in Action: An Overview of Cancer Nanomedicine on the Market and in Clinical Trials. *Journal of Nanomaterials* **2013**, *2013*, 629681.
3. Begines, B.; Ortiz, T.; Pérez-Aranda, M.; Martínez, G.; Merinero, M.; Argüelles-Arias, F.; Alcudia, A. Polymeric Nanoparticles for Drug Delivery: Recent Developments and Future Prospects. *Nanomaterials* **2020**, *10*, 1403.
4. Zhang, C. Progress, challenges, and future of nanomedicine. *Elsevier B.V* **2020**.
5. Popat, K.; McQueen, K.; Feeley, T.W. The Global Burden of Cancer. *Best Practice & Research Clinical Anaesthesiology* **2013**, *27*, 399–408, doi:10.1016/j.bpa.2013.10.010.
6. Klisic, A.; Ahmad, R.; Haddad, D.; Bonomini, F.; Sindhu, S. Editorial: The Role of Oxidative Stress in Metabolic and Inflammatory Diseases. *Front. Endocrinol.* **2024**, *15*, 1374584, doi:10.3389/fendo.2024.1374584.
7. Mohammed, A.M.; Mohammed, M.; Oleiwi, J.K.; Ihmedee, F.H.; Adam, T.; Betar, B.O.; Gopinath, S.C.B. The Anticancer, Antioxidant, and Antimicrobial Properties of Zinc Oxide Nanoparticles: A Comprehensive Review. *Nano TransMed* **2025**, *4*, 100097.
8. Hassanein, T.F.; Mohammed, A.S.; Mohamed, W.; Sobh, R.A.; Zahran, M.K. Optimized Synthesis of Biopolymer-Based Zinc Oxide Nanoparticles and Evaluation of Their Antibacterial Activity. *Egypt. J. Chem* **2021**, *64*, 3767–3790.
9. Sun, T.; Zhang, Y.S.; Pang, B.; Hyun, D.C.; Yang, M.; Xia, Y. Engineered Nanoparticles for Drug Delivery in Cancer Therapy. *Nanomater. Neoplasms* **2021**, 31–142.
10. Gavas, S.; Quazi, S.; Karpiński, T.M. *Nanoparticles for Cancer Therapy: Current Progress and Challenges*; Springer, 2021;
11. Vert, M. Terminology for Biorelated Polymers and Applications (IUPAC Recommendations 2012. *Pure and Applied Chemistry* **2012**, *84*, 377-410,.
12. Khurshid, Z.; Zafar, M.; Qasim, S.; Shahab, S.; Naseem, M.; AbuReqaiba, A. Advances in Nanotechnology for Restorative Dentistry. *Materials* **2015**, *8*, 717–731.
13. Goldberg, M.; Langer, R.; Jia, X. Nanostructured Materials for Applications in Drug Delivery and Tissue Engineering. *Journal of Biomaterials Science, Polymer Edition* **2007**, *18*, 241–268, doi:10.1163/156856207779996931.
14. Bisht, G.; Rayamajhi, S. ZnO Nanoparticles: A Promising Anticancer Agent. *Apr* **2016**, *20*.
15. Mitchell, M.J.; Billingsley, M.M.; Haley, R.M.; Wechsler, M.E.; Peppas, N.A.; Langer, R. Engineering Precision Nanoparticles for Drug Delivery. *Feb* **2021**, *01*.
16. Sarnelli, S.; Cardamone, M.; Reverchon, E.; Baldino, L. Lipid-Based Nanoparticles for Nucleic Acids Delivery. *Physical Sciences Reviews* **2025**, *10*, 317–338, doi:10.1515/psr-2025-0001.
17. Anselmo, A.C.; Mitragotri, S. A Review of Clinical Translation of Inorganic Nanoparticles. *AAPS J* **2015**, *17*, 1041–1054, doi:10.1208/s12248-015-9780-2.
18. Carofiglio, M.; Barui, S.; Cauda, V.; Laurenti, M. Doped Zinc Oxide Nanoparticles: Synthesis, Characterization and Potential Use in Nanomedicine. *Applied Sciences* **2020**, *10*, 5194.
19. Racca, L.; Canta, M.; Dumontel, B.; Ancona, A.; Limongi, T.; Garino, N.; Laurenti, M.; Canavese, G.; Cauda, V. Zinc Oxide Nanostructures in Biomedicine. In *Smart*

Nanoparticles for Biomedicine; Ciofani, G., Ed.; Elsevier: Amsterdam, The Netherlands, 2018; pp. 171–187.

20. Espitia, P.J.P.; Otoni, C.G.; Soares, N.F.F. Chapter 34—Zinc Oxide Nanoparticles for Food Packaging Applications. In *Antimicrobial Food Packaging*; Barros-Velázquez, J., Ed.; San Diego, CA, USA, 2016; pp. 425–431.
21. Lee, K.M.; Lai, C.W.; Ngai, K.S.; Juan, J.C. Recent Developments of Zinc Oxide Based Photocatalyst in Water Treatment Technology: A Review. *Water Research* **2016**, *88*, 428–448.
22. Laurenti, M.; Garino, N.; Canavese, G.; Hernandéz, S.; Cauda, V. Piezo- and Photocatalytic Activity of Ferroelectric ZnO:Sb Thin Films for the E_cient Degradation of Rhodamine-_ Dye Pollutant. *ACS Appl. Mater. Interfaces* **2020**, *12*, 25798–25808.
23. Lops, C.; Ancona, A.; Cesare, K.; Dumontel, B.; Garino, N.; Canavese, G.; Hérnandez, S.; Cauda, V. Sonophotocatalytic Degradation Mechanisms of Rhodamine B Dye via Radicals Generation by Micro- and Nano-Particles of ZnO. *Appl. Catal. B Environ* **2019**, *243*, 629–640.
24. Laurenti, M.; Stassi, S.; Lorenzoni, M.; Fontana, M.; Canavese, G.; Cauda, V.; Pirri, C.F. Evaluation of the Piezoelectric Properties and Voltage Generation of Flexible Zinc Oxide Thin Films. *Nanotechnology* **2015**, *26*, 215704.
25. Laurenti, M.; Canavese, G.; Stassi, S.; Fontana, M.; Castellino, M.; Pirri, C.F.; Cauda V.Aporous Nanobranched Structure: An E_ective Way to Improve Piezoelectricity in Sputtered ZnO Thin Films. *RSC Adv* **2016**, *6*, 76996–77004.
26. Liu, J.; Fernández-Serra, M.V.; Allen, P.B. First-Principles Study of Pyroelectricity in GaN and ZnO. *Phys. Rev. B* **2016**, *93*, 081205.
27. Ahamed, M.; Akhtar, M.J.; Khan, M.A.M.; Alhadlaq, H.A. Enhanced Anticancer Performance of Eco-Friendly-Prepared Mo-ZnO/RGO Nanocomposites: Role of Oxidative Stress and Apoptosis. *ACS Omega* **2022**, *7*, 7103–7115.
28. Laurenti, M.; Cauda, V. Porous Zinc Oxide Thin Films: Synthesis Approaches and Applications. *Coatings* **2018**, *8*, 67.
29. Znaidi, L. Sol–Gel-Deposited ZnO Thin Films: A Review. *Mater. Sci. Eng. B* **2010**, *174*, 18–30.
30. Bagga, S.; Akhtar, J.; Mishra, S. Synthesis and Applications of ZnO Nanowire: A Review. In Proceedings of the AIP Conf. Proc. 2018; 1989; p. 020004.
31. Yi, G.-C.; Wang, C.; Park, W.I. ZnO Nanorods: Synthesis, Characterization and Applications. *Semicond. Sci. Technol* **2005**, *20*, 22–34.
32. Li, Y.B.; Bando, Y.; Sato, T.; Kurashima, K. ZnO nanobelts grown on Si substrate. *Appl. Phys. Lett* **2002**, *81*, 144–146.
33. Garino, N.; Limongi, T.; Dumontel, B.; Canta, M.; Racca, L.; Laurenti, M.; Castellino, M.; Casu, A.; Falqui, A.; Cauda, V. A Microwave-Assisted Synthesis of Zinc Oxide Nanocrystals Finely Tuned for Biological Applications. *Nanomaterials* **2019**, *9*, 212.
34. Cauda, V.; Pugliese, D.; Garino, N.; Sacco, A.; Bianco, S.; Bella, F.; Lamberti, A.; Gerbaldi, C. Multi-Functional Energy Conversion and Storage Electrodes Using Flower-like Zinc Oxide Nanostructures. *Energy* **2014**, *65*, 639–646.
35. Sirelkhatim, A. Review on Zinc Oxide Nanoparticles: Antibacterial Activity and Toxicity Mechanism. *Nanomicro Lett* **2015**, *7*, 219-242,.
36. Wolfbeis, O.S. An Overview of Nanoparticles Commonly Used in Fluorescent Bioimaging. *Chem. Soc. Rev* **2015**, *44*, 4743–4768.

37. Boschi, F.; Sanctis, F. Overview of the Optical Properties of Fluorescent Nanoparticles for Optical Imaging. *Eur. J. Histochem. EJH* **2017**, *61*, 2830.
38. Dumontel, B. Enhanced Biostability and Cellular Uptake of Zinc Oxide Nanocrystals Shielded with a Phospholipid Bilayer. *J Mater Chem B* **2017**, *5*, 8799-8813,.
39. Cao, D.; Shu, X.; Zhu, D.; Liang, S.; Hasan, M.; Gong, S. Lipid-Coated ZnO Nanoparticles Synthesis, Characterization and Cytotoxicity Studies in Cancer Cell. *Nano Convergence* **2020**, *7*, 14, doi:10.1186/s40580-020-00224-9.
40. Vighetto, V.; Ancona, A.; Racca, L.; Limongi, T.; Troia, A.; Canavese, G.; Cauda, V. The Synergistic Effect of Nanocrystals CombinedWith Ultrasound in the Generation of Reactive Oxygen Species for Biomedical Applications. *Front. Bioeng. Biotechnol* **2019**, *7*, 374.
41. Dumontel, B.; Susa, F.; Limongi, T.; Canta, M.; Racca, L.; Chiodoni, A.; Garino, N.; Chiabotto, G.; Centomo, M.L.; Pignochino, Y.; et al. ZnO Nanocrystals Shuttled By Extracellular Vesicles As Effective Trojan Nano-Horses Against Cancer Cells. *Nanomedicine (Lond.)* **2019**, *14*, 2815–2833.
42. Moon, S.-H.; Choi, W.J.; Choi, S.-W.; Kim, E.H.; Kim, J.; Lee, J.-O.; Kim, S.H. Anti-Cancer Activity of ZnO Chips by Sustained Zinc Ion Release. *Toxicol. Rep* **2016**, *3*, 430–438.
43. Jiang, J.; Pi, J.; Cai, J. The Advancing of Zinc Oxide Nanoparticles for Biomedical Applications, Bioinorg. *Chem. Appl* **2018**, 1–18.
44. Anjum, S.; Hashim, M.; Malik, S.; Khan, M.; Lorenzo, J.; Abbasi, B.; Hano, C. Recent Advances in Zinc Oxide Nanoparticles (Zno Nps) for Cancer Diagnosis, Target Drug Delivery, and Treatment. *Cancers* **2021**, *13*, 4570.
45. Bai, D.; Zhang, X.; Zhang, G.; Huang, Y.; Gurunathan, S. Zinc Oxide Nanoparticles Induce Apoptosis and Autophagy in Human Ovarian Cancer Cells. *Int. J. Nanomed* **2017**, *12*, 6521–6535.
46. Loganathan, S.; Manimaran, K.; Mutamimurugan, K.; Prakash, D.; Subashini, R. Green Synthesis of Zinc Oxide Nanoparticles (Zno-Nps) by Pterolobium Hexapetalum (Roth) Santapau & Wagh Aqueous Leaf Extract and Its Assessment of Biocompatible, Antibacterial, Dpph Radical Scavenging, Anticancer and Larvicidal Activities: An Effective Eco-Friendly Approach 2022.
47. Laurenti, M.; Cauda, V. ZnO Nanostructures for Tissue Engineering Applications. *Nanomaterials* **2017**, *7*, 374.
48. Malik, R.; Tomer, V.K.; Mishra, Y.K.; Lin, L. Functional gas sensing nanomaterials: A panoramic view. *Appl. Phys. Rev* **2020**, *7*, 021301.
49. Rivera, V.F.; Auras, F.; Motto, P.; Stassi, S.; Canavese, G.; Celasco, E.; Bein, T.; Onida, B.; Cauda, V. Length-Dependent Charge Generation from Vertical Arrays of High-Aspect-Ratio ZnO Nanowires. *Chem. A Eur. J* **2013**, *19*, 14665–14674.
50. Carofiglio, M.; Laurenti, M.; Vighetto, V.; Racca, L.; Barui, S.; Garino, N.; Gerbaldo, R.; Laviano, F.; Cauda, V. Iron-Doped ZnO Nanoparticles as Multifunctional Nanoplatforms for Theranostics. *Nanomaterials* **2021**, *11*, 2628.
51. Xia, T.; Zhao, Y.; Sager, T.; George, S.; Pokhrel, S.; Li, N.; Schoenfeld, D.; Meng, H.; Lin, S.; Wang, X. Decreased Dissolution of ZnO by Iron Doping Yields Nanoparticles with Reduced Toxicity in the Rodent Lung and Zebrafish Embryos. *ACS Nano* **2011**, *5*, 1223–1235.
52. Chia, S.L.; Leong, D.T. Reducing ZnO Nanoparticles Toxicity through Silica Coating. *Heliyon* **2016**, *2*, e00177.

53. Chen, M.; Hu, J.; Bian, C.; Zhu, C.; Chen, C.; Guo, Z.; Zhang, Z.; Agyekum, G.A.; Zhang, Z.; Cao, X. pH-Responsive and Biodegradable ZnO-Capped Mesoporous Silica Composite Nanoparticles for Drug Delivery. *Materials* **2020**, *13*, 3950.
54. Vandebriel, R.J.; Jong, W.H. A Review of Mammalian Toxicity of ZnO Nanoparticles. *Nanotechnol. Sci. Appl* **2012**, *5*, 61–71.
55. Li, Y.; Li, F.; Zhang, L.; Zhang, C.; Peng, H.; Lan, F.; Guo, J. Zinc Oxide Nanoparticles Induce Mitochondrial Biogenesis Impairment and Cardiac Dysfunction in Human Ipsc-Derived Cardiomyocytes. *Int. J. Nanomed* **2020**, *15*, 2669–2683.
56. Pandurangan, M.; Kim, D.H. In Vitro Toxicity of Zinc Oxide Nanoparticles: A Review. *J. Nanoparticle Res* **2015**, *17*, 158.
57. Chen, X.; Wang, Q.; Wang, X.-J.; Li, J.; Xu, G.-B. Synthesis and Performance of ZnO Quantum Dots Water-Based Fluorescent Ink for Anti-Counterfeiting Applications. *Sci Rep* **2021**, *11*, 5841, doi:10.1038/s41598-021-85468-z.
58. Durfee, P.N.; Lin, Y.-S.; Dunphy, D.R.; Muñiz, A.J.; Butler, K.S.; Humphrey, K.R.; Lokke, A.J.; Agola, J.O.; Chou, S.S.; Chen, I.-M.; et al. Mesoporous Silica Nanoparticle-Supported Lipid Bilayers (Protocells) for Active Targeting and Delivery to Individual Leukemia Cells. *ACS Nano* **2016**, *10*, 8325–8345.
59. Zöller, K.; Haddadzadegan, S.; Lindner, S.; Veider, F.; Bernkop-Schnürch, A. Design of Charge Converting Lipid Nanoparticles via a Microfluidic Coating Technique. *Drug Deliv. and Transl. Res.* **2024**, *14*, 3173–3185, doi:10.1007/s13346-024-01538-5.
60. Malvern Panalytical, 2025, Zetasizer Nano ZS Technical Specifications and Manuals, Malvern Panalytical Official Website, Https://Www.Malvernpanalytical.Com/En/Support/Product-Support/Zetasizer-Range/Zetasizer-Nano-Range/Zetasizer-Nano-Zs#manuals, Accessed December 17, 2025.
61. Foster, C.G.O.; Mayer, M.M.; Avery, M.L.; Audus1, K.L. Characterization of the A549 Cell Line as a Type II Pulmonary Epithelial Cell Model for Drug Metabolism Kimberly A.
62. Lieber, M.; Smith, B.; Szakal, A.; Nelson-Rees, W.; Todaro, G. A Continuous Tumor-Cell Line from a Human Lung Carcinoma with Properties of Type II Alveolar Epithelial Cells. *Int J Cancer* **1976**, *17*, 62–70.
63. Hastings, R.H.; Wright, J.R.; Albertine, K.H.; Ciriales, R.; Matthay, M.A. Effect of endocytosis inhibitors on alveolar clearance of albumin, immunoglobulin G, and SP-A in rabbits. *Am. J. Physiol* **1994**, *266*, 544–552.
64. Ryan, R.M.; Mineo-Kuhn, M.M.; Kramer, C.M.; Finkelstein, J.N. Growth factors alter neonatal type II alveolar epithelial cell proliferation. *Am. J. Physiol* **1994**, *266*, 17–22.
65. Gotze, J.P.; Lindeskog, P.; Tornquist, C.S.I. Characterization of the A549 Cell Line as a Type II Pulmonary Epithelial Cell Model for Drug Metabolism. *Health Perspect* **1994**, *102*, 147–156.
66. Ito, T.; Kitamura, H.; Inayama, Y.; Nozawa, A.; Kanisawa, M. Uptake and Intracellular Transport of Cationic Ferritin in the Bronchiolar and Alveolar Epithelia of the Rat. *Cell Tissue Res* **1992**, *268*, 335-340 10 1186 12989-021-00424-.
67. Norberg, N.S.; Kittilstved, K.R.; Amonette, J.E.; Kukkadapu, R.K.; Schwartz, D.A.; Gamelin, D.R. Synthesis of Colloidal Mn^{2+}:ZnO Quantum Dots and High- T_C Ferromagnetic Nanocrystalline Thin Films. *J. Am. Chem. Soc.* **2004**, *126*, 9387–9398, doi:10.1021/ja048427j.

68. Baruah, S.; Dutta, J. Hydrothermal Growth of ZnO Nanostructures. *Science and Technology of Advanced Materials* **2009**, *10*, 013001, doi:10.1088/1468-6996/10/1/013001.
69. Khoza, P.B.; Moloto, M.J.; Sikhwivhilu, L.M. The Effect of Solvents, Acetone, Water, and Ethanol, on the Morphological and Optical Properties of ZnO Nanoparticles Prepared by Microwave. *Journal of Nanotechnology* **2012**, *2012*, 1–6, doi:10.1155/2012/195106.
70. Hu, Z.; Oskam, G.; Searson, P.C. Influence of Solvent on the Growth of ZnO Nanoparticles. *Journal of Colloid and Interface Science* **2003**, *263*, 454–460, doi:10.1016/S0021-9797(03)00205-4.
71. Zhang, X.; Luo, S.; Wu, X.; Feng, M.; Li, Y.; Han, H.; Li, W. Effect of Alkali Bases on the Synthesis of ZnO Quantum Dots. *Open Chemistry* **2021**, *19*, 377–384, doi:10.1515/chem-2021-0027.
72. Carofiglio, M.; Laurenti, M.; Vighetto, V.; Racca, L.; Barui, S.; Garino, N.; Gerbaldo, R.; Laviano, F.; Cauda, V. Iron-Doped ZnO Nanoparticles as Multifunctional Nanoplatforms for Theranostics. *Nanomaterials* **2021**, *11*, 2628, doi:10.3390/nano11102628.
73. Qamar, A.; Arshad, A.; Anwar, Z.; Shaukat, R.; Amjad, M.; Imran, S.; Razzaq, L.; Ali, M.; Korakianitis, T. Dispersion Stability and Rheological Characteristics of Water and Ethylene Glycol Based ZnO Nanofluids. *Therm sci* **2021**, *25*, 1989–2001, doi:10.2298/TSCI200110187Q.
74. Kawska, A.; Duchstein, P.; Hochrein, O.; Zahn, D. Atomistic Mechanisms of ZnO Aggregation from Ethanolic Solution: Ion Association, Proton Transfer, and Self-Organization. *Nano Lett.* **2008**, *8*, 2336–2340, doi:10.1021/nl801169x.
75. Matea, C.; Mocan, T.; Tabaran, F.; Pop, T.; Mosteanu, O.; Puia, C.; Iancu, C.; Mocan, L. Quantum Dots in Imaging, Drug Delivery and Sensor Applications. *IJN* **2017**, *Volume 12*, 5421–5431, doi:10.2147/IJN.S138624.
76. Boonphan, S.; Prachakiew, S.; Keereeta, Y.; Klinbumrung, A. Precursor-Dependent Crystallinity and Surface Charge Modulation of ZnO Nanostructures via Microwave-Assisted Synthesis. *Ionics* **2025**, *31*, 12355–12377, doi:10.1007/s11581-025-06660-z.
77. Hao, N.; Chen, X.; Jayawardana, K.W.; Wu, B.; Sundhoro, M.; Yan, M. Shape Control of Mesoporous Silica Nanomaterials Templated with Dual Cationic Surfactants and Their Antibacterial Activities. *Biomater. Sci.* **2016**, *4*, 87–91, doi:10.1039/C5BM00197H.
78. Cui, Y.; Dong, H.; Cai, X.; Wang, D.; Li, Y. Mesoporous Silica Nanoparticles Capped with Disulfide-Linked PEG Gatekeepers for Glutathione-Mediated Controlled Release. *ACS Appl. Mater. Interfaces* **2012**, *4*, 3177–3183, doi:10.1021/am3005225.
79. Malvern Panalytical, 2025, Zetasizer Nano ZS Technical Specifications and Manuals, Malvern Panalytical Official Website. Measuring Non-Spherical Objects with Dynamic Light Scattering.
80. Moncrieff, D.A.; Barker, P.R. Secondary Electron Emission in the Scanning Electron Microscope. *Scanning* **1978**, *1*, 195–197, doi:10.1002/sca.4950010307.
81. Meyer, T.J.; Scherzad, A.; Moratin, H.; Gehrke, T.E.; Killisperger, J.; Hagen, R.; Wohlleben, G.; Polat, B.; Dembski, S.; Kleinsasser, N.; et al. The Radiosensitizing Effect of Zinc Oxide Nanoparticles in Sub-Cytotoxic Dosing Is Associated with Oxidative Stress In Vitro. *Materials* **2019**, *12*, 4062, doi:10.3390/ma12244062.
82. Ketebo, A.A.; Din, S.U.; Lee, G.; Park, S. Mechanobiological Analysis of Nanoparticle Toxicity. *Nanomaterials* **2023**, *13*, 1682, doi:10.3390/nano13101682.

83. Kersting, M.; Olejnik, M.; Rosenkranz, N.; Loza, K.; Breisch, M.; Rostek, A.; Westphal, G.; Bünger, J.; Ziegler, N.; Ludwig, A.; et al. Subtoxic Cell Responses to Silica Particles with Different Size and Shape. *Sci Rep* **2020**, *10*, 21591, doi:10.1038/s41598-020-78550-5.
84. Moriones, P.; Arzamendi, G.; Cornejo, A.; Garrido, J.J.; Echeverria, J.C. Comprehensive Kinetics of Hydrolysis of Organotriethoxysilanes by^{29} Si NMR. *J. Phys. Chem. A* **2019**, *123*, 10364–10371, doi:10.1021/acs.jpca.9b08910.
85. Hao, N.; Zhang, M.; Zhang, J.X.J. Microfluidics for ZnO Micro-/Nanomaterials Development: Rational Design, Controllable Synthesis, and on-Chip Bioapplications. *Biomater. Sci.* **2020**, *8*, 1783–1801, doi:10.1039/C9BM01787A.
86. Popa, M.L.; Preda, M.D.; Neacșu, I.A.; Grumezescu, A.M.; Ginghină, O. Traditional vs. Microfluidic Synthesis of ZnO Nanoparticles. *IJMS* **2023**, *24*, 1875, doi:10.3390/ijms24031875.
87. George, A.; Alva, E.; Brancaleon, L.; Marucho, M. Dynamic and Electrophoretic Light Scattering Measurements on Microtubules at Low Concentrations. *PLoS ONE* **2024**, *19*, e0312430, doi:10.1371/journal.pone.0312430.